# ELECTRONIC SPECTRA OF FULLERENES IN CRYOGENIC RADIO FREQUENCY ION TRAPS

**Inauguraldissertation**
zur
Erlangung der Würde eines Doktors der Philosophie
vorgelegt der
Philosophisch-Naturwissenschaftlichen Fakultät
der Universität Basel

von

Mathias Holz
aus Finsterwalde, Deutschland

Basel, 2017



Genehmigt von der Philosophisch-Naturwissenschaftlichen Fakultät
auf Antrag von

**Prof. Dr. John P. Maier**

**Prof. Dr. Stefan Willitsch**

Basel, den 20.09.2016

**Prof. Dr. Jörg Schibler**

Dekan

# Acknowledgement

This little scientific contribution would not have been possible without guidance and support of several individuals.

First of all I would like to thank Prof. John P. Maier who gave me the opportunity to work in his group, as well as for his assistance, financial support and lots of patience throughout my doctoral studies.

I thank Prof. Stefan Willitsch agreeing to be the co-referee of my thesis and Prof. Cornelia G. Palivan for taking responsibility of chairing my defense.

During the whole time I had the privilege to work with Prof. Dieter Gerlich. His deep knowledge about ion-trapping and enthusiasm for science is without equal. It was a fortunate for me and this project to have him participating.

Similar words I could find for Dr. Corey Rice. He became not only a valuable colleague, but even more a very good friend. Although we didn't work on the same projects he always offered a helping hand to find solutions for any problem. Special thanks also to Dr. Satrajit Chakrabarty not only for explaining me the aspects of the machine when I made my first steps with ion-trapping. I greatly enjoyed the company of Dr. Varun Gupta, Dr. Rainer Dietsche and Dr. Ranjini Dietsche, Kaveh Najafian, Panagiotis Fountas, Karol Filipkowski and Dr. Lindsay Zack. Apart from science we shared plenty of time outside the labs having BBQs by the Rhine, or discussing semi-scientific problems at "Bester Pizza". It was really a great pleasure to have met you guys, I hope I will see all of you from time to time.

I'd like to thank Dr. Ewen Campbell working with me in the lab and pushing the machine to its limits to obtain these nice results.

Much of the presented work in this thesis would have never been possible without the excellent support of Georg Holderied (electronics), Dr. Anatoly Johnson (lasers), Jacques Lecoultre (chemicals, synthesizing), the mechanical workshop with Grisha Martin, Philipp Knöpfel and Dieter Wild. Danni Tischhauser and Maya Greuter are kindly acknowledged for off-scientific matters.

And of course I thank my family and friends in Basel and Berlin for providing support not only in the last five years, but my whole life through. Finally I would like to thank Rebecca for her encouragement, strength and loving care she has been giving.

# Abstract

Over several decades interest has been devoted to the astronomical enigma of the diffuse interstellar bands (DIBs). These are hundreds of absorption features of interstellar origin seen in the spectra of stars with different strengths and widths spread over the visible and near infrared (NIR). They are typically broader than atomic lines and concluded to be of molecular nature. Polycyclic aromatic hydrocarbons, long carbon-chain molecules, and fullerenes have been suspected as their carriers.

Two of the DIBs showed coincident spectral features recorded in a neon matrix experiment for the fullerene $C_{60}^+$. Embedding molecules in a solid matrix are known to induce perturbations of the measured spectrum and consequently, the assignment was classified as tentative. An unambiguous identification of a specific molecule as a carrier can only be made upon measurements of its laboratory gas-phase spectrum under similar conditions as they are present in the interstellar medium. Nevertheless, the recent identification of the infrared signature of $C_{60}$, $C_{60}^+$ and $C_{70}$ in the spectra of a protoplanetary and reflection nebula fueled their relevance as possible candidates.

Optical and NIR spectroscopy of large molecules has strong demands on the employed method. Therefore, an existing apparatus was improved and a special spectroscopic technique was thought. The heart of the experiment was a radio-frequency ion trap in which a cryogenic bath of a neutral gas was created to confine and prepare the ionic species for further investigations. Electronic gas-phase spectra have been finally obtained by photofragmentation of weakly bound cation-helium complexes, which enabled a confident confrontation with astronomical observations. In the case of $C_{60}^+$, an unequivocal assignment of five DIBs has been achieved, and thus, the first identification of a carrier almost 100 years after their first detection.

# Contents

**Acknowledgement** **v**

**Abstract** **vii**

**1 Introduction** **1**
1.1 The Diffuse Interstellar Bands . . . 2
1.2 Fullerenes as Carriers of the DIBs . . . 3
1.3 Motivation and Thesis Structure . . . 5
Bibliography . . . 7

**2 Methodology** **11**
2.1 Ion Motion in Multipole RF-Fields . . . 11
2.1.1 Mass Filtering in a Quadrupole . . . 12
2.1.2 Ion Trapping . . . 14
2.2 Buffer Gas Cooling of Ions . . . 16
2.3 Electronic Spectroscopy . . . 17
2.3.1 The Franck-Condon Principle . . . 20
2.3.2 Selection Rules . . . 21
2.4 Spectroscopic Methods . . . 22
2.4.1 Absorption Spectroscopy . . . 22
2.4.2 Photodissociation Spectroscopy of Weakly Bound Complexes . . . 23
2.4.3 Line-Shape Functions . . . 25
Bibliography . . . 28

**3 Experimental** **31**
3.1 Electron Impact Source . . . 33
3.2 Quadrupole Mass Filter . . . 35
3.3 Multipole Radio Frequency Ion Traps . . . 37
3.3.1 22-Pole Trap . . . 37
3.3.2 4-Pole Trap . . . 38
3.3.3 Piezo Valve . . . 39
3.4 Ion Detection . . . 41
3.5 Laser Systems . . . 43
3.6 Operating procedures . . . 44
3.6.1 Estimation of Number Densities . . . 44

3.6.2 Ion Trapping and Complex Formation . . . 45
3.6.3 Absorption Cross-Sections . . . 48
Bibliography . . . 51

**4 Laser Induced Inhibition of Complex Growth 53**
4.1 Proof of Principle on $N_2^+$ . . . 55
4.1.1 Experimental Conditions . . . 55
4.1.2 Spectroscopy . . . 55
4.1.3 Laser Induced Charge Transfer Reaction to Ar . . . 57
4.1.4 Dynamical Processes . . . 58
4.1.5 Conclusion . . . 59
4.2 $NCCN^+$–He . . . 61
4.3 $C_{14}H_{10}^+$–He . . . 63
4.4 Conclusion . . . 64
Bibliography . . . 66

**5 Electronic Spectra of Fullerenes 69**
5.1 $C_{60}^+$ . . . 70
5.1.1 $C_{60}^+$–He . . . 70
5.1.2 $C_{60}^+$–$n$He . . . 75
5.1.3 Comparison to the DIBs . . . 79
5.1.4 $C_{60}^+$–$L$ ($L$ =Ne, Ar, Kr, $H_2$, $D_2$, $N_2$) . . . 82
5.2 $C_{70}^+$ . . . 91
5.2.1 $C_{70}^+$–He . . . 91
5.2.2 Comparison to the DIBs . . . 93
5.3 $C_{60}^{2+}$–He and $C_{70}^{2+}$–He . . . 95
5.4 $C_{84}^+$–He . . . 97
5.5 Conclusion . . . 97
Bibliography . . . 100

**6 Conclusion and Outlook 105**
Bibliography . . . 107

**Appendix 109**
A Relaxation Kinetics: Microscopic Reversibilty . . . 109
B Table Parameters of 9577/9632 DIBs . . . 111
Bibliography . . . 112

# 1

*Space is big. You just won't believe how vastly, hugely, mind-bogglingly big it is. I mean, you may think it's a long way down the road to the chemist's, but that's just peanuts to space.*

■ Douglas Adams

# Introduction

The space between stars or galaxies is not completely empty. The interstellar medium (ISM) contains mainly gas but also dust, which coexist under different physical conditions. Hydrogen and helium have been identified as the most abundant elements, heavier atoms represent less than 2 % as illustrated in a periodic table of elements for astronomers shown in Figure 1.1. Interstellar gas and dust aggregate to form interstellar clouds which absorb and scatter blue light more than red, making the stars in the line-of-sight appear redder than they are. To reflect the different local conditions mainly based on temperature and atomic hydrogen densities, a classification in diffuse atomic, diffuse molecular, translucent, and dense molecular has been made [1]. The formation of stars occurs in dense clouds, where molecular hydrogen becomes more abundant. Heavier elements such as carbon, nitrogen or oxygen are produced in their hot cores and are ejected into the surroundings from the collapsing star at the end of its main life cycle. Depending on the local environment, this allows a rich chemistry and the production of organic materials in the ISM.

Since the first identification of molecules in the ISM, approximately $\sim 200$ have been detected to be present in the ISM or circumstellar shells [2]. The detection mechanism utilizes spectroscopic methods as direct sampling is only possible by probing meteoroids. An exception was the recent investigation of a comet's (67P/Churyumov–Gerasimenko) composition, when a special equipped module of a space probe was dropped on the object [3]. However, most of the species in the ISM are detected by radio, mirco- and millimeter-waves as they exhibit a permanent dipole moment allowing a detection via their rotational spectrum.

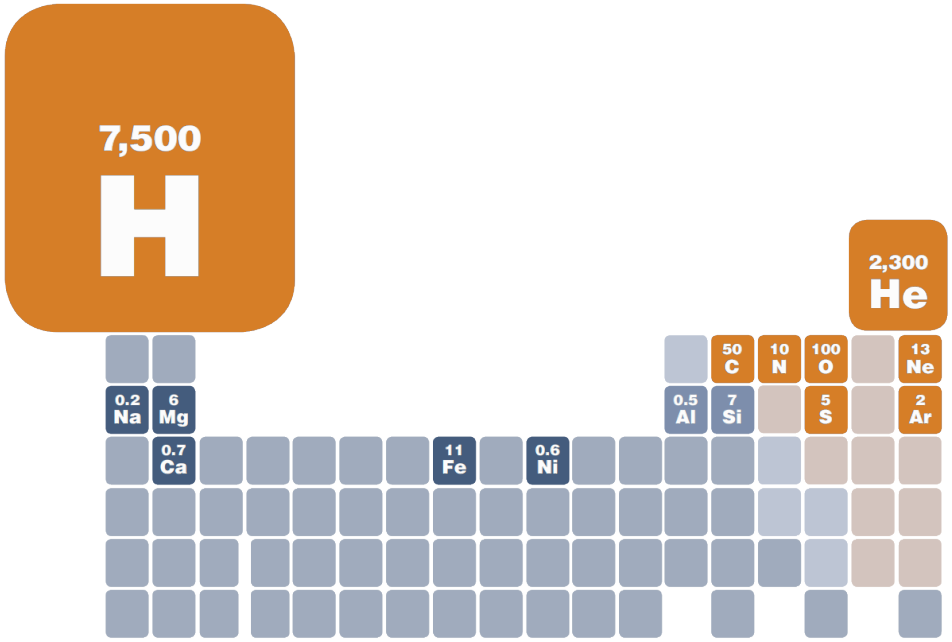


Figure 1.1: Astronomers view on the periodic table of elements [4]. Shown is the relative abundance in parts per 10 000. These values give e.g. indications for requirements of interstellar chemical reactions.

## 1.1 The Diffuse Interstellar Bands

One of the biggest mysteries in astronomical spectroscopy are the diffuse interstellar bands (DIBs). These are absorption features in the optical (VIS) and infrared (IR) spectra of stars seen through interstellar clouds. They were first observed in 1921 by Mary Lea Heger [5], when she was studying the spectra of different stars and later confirmed by Paul Merrill [6]. It was found that DIBs have to be of interstellar origin, because their frequencies are not affected by Doppler broadening when the two stars in a binary system went through their orbits. Meanwhile several hundred lines have been reported with a large spread in spectral characteristics. Their full-widths-at-half-maximum (FWHM) range from less than 1 Å to 30 Å with different strengths. Some narrow DIBs show asymmetric profiles and/or unresolved rotational contours, while others indicate natural linewidths [7].

Survey studies of the complete DIB spectrum in different regions of the ISM have been examined in order to find correlations between the DIBs but led to little success [8]. Significant differences in density and UV flux determine the existence, abundance and ionization stage of the corresponding carrier molecules and provide several starting points for identification strategies [9–11]. Early hypotheses considered dust grains as carriers, but they have been discarded [12]. Much attention

was also raised to the group of polycyclic aromatic hydrocarbons (PAHs) when some of them were detected in diffuse and dark clouds in the IR [13, 14]. These are assumed to be the most abundant organic molecules in the ISM holding more than 15 % of all cosmic carbon. In ionic form their electronic transitions are expected in the visible spectrum with narrow lines [15–18]. A low ionization potential of typically less than $< 10\,\mathrm{eV}$ and their photo-stability would even more favor them as possible candidates. Protonated species of larger PAHs have been also added to the list as they have similar properties [19, 20]. The most promising candidates of carbon bearing molecules have been the cationic naphthalene, diacetylene, and neutral $H_2CCC$. An extensive discussion concluded that an unequivocal assignment of these molecules is not feasible [21–27].

## 1.2 Fullerenes as Carriers of the DIBs

Fullerenes were suggested to be widely distributed in the ISM as outflows of carbon rich stars with low $H_2$ abundance. They are a class of spherical, elliptical or cylindrical molecules typically composed of linked six and five membered carbon rings. Terrestrial abundances are limited to low concentrations and occurrences are correlated with localized energetic events [28]. The name has been a homage to Richard Buckminster Fuller because of the similarity to his geodesic domes as shown in Figure 1.2. The most prominent one $C_{60}$, also known as buckminsterfullerene or buckyball, was discovered by Harold Kroto and coworkers in 1985 and very shortly after he already proposed [29, 30]:

> *"The present observations indicate that $C_{60}$ might survive in the general interstellar medium (probably as the ion $C_{60}^+$) protected by its unique ability to survive processes so drastic that, most if not all, other known molecules are destroyed.",*

First laboratory spectra of $C_{60}$ became possible with the synthesis in macroscopic quantities [32]. Comparisons of UV/VIS transitions to known DIBs have led to negative results [33, 34]. Recently, the vibrational IR signature of $C_{60}$ has been detected in protoplanetary and reflection nebula confirming its abundance in the ISM [35–37].

In 1994, Bernhard Foing and Pascale Ehrenfreund assigned a pair of DIBs to $C_{60}^+$ based on their proximity to laboratory absorptions bands measured in a neon matrix isolation experiment [38, 39]. In the following years, these two bands have

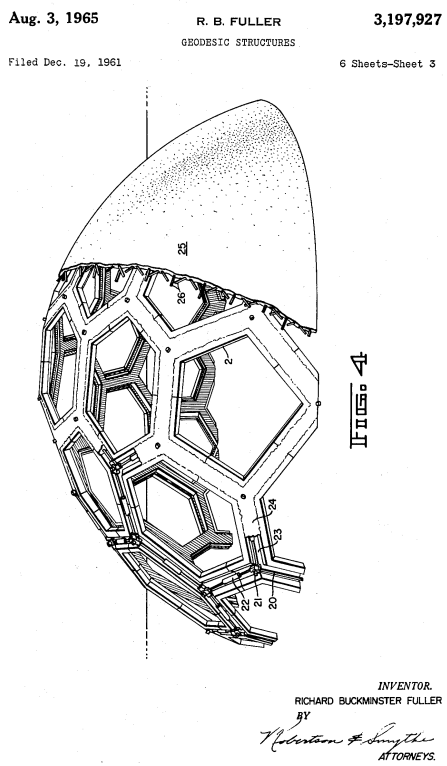


(a)

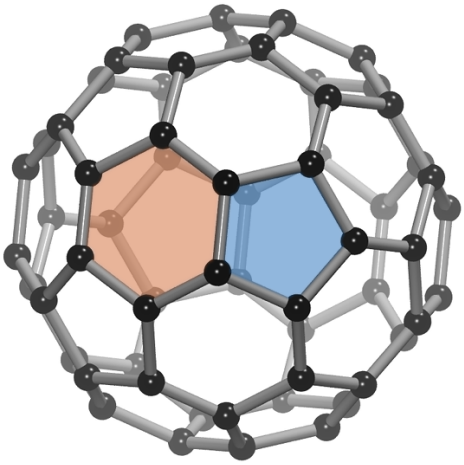

(b)

Figure 1.2: (a) One of the geodesic domes proposed and patented by R. Buckminster Fuller [31]. In comparison (b) the (truncated) icosahedral molecular structure of $C_{60}$ with indicated (●) penta- and (●) hexagon ring.

been under permanent discussion because of several discrepancies in their spectrum, which is shown in Figure 1.3. The ground-based astronomical observations have several constraints. For example, due to the earth's atmosphere, strong and variable absorption features in the near infrared (NIR) mainly caused by water vapor require extensive corrections. On the laboratory side, embedding a molecule in a solid environment leads to unpredictable significant perturbations to the spectrum of the probed species [40]. Broadened lineshapes, shifted frequencies, and the intensity ratios allowed only tentative conclusions. While the two DIBs have been confirmed toward several lines-of-sight, a laboratory gas-phase spectrum of $C_{60}^{+}$ is still not available. Measurements of electronic transitions of possible carriers have to be done under conditions comparable to the local environment in the ISM. This desires cryogenic temperatures and a spectroscopic method allowing an investigation of the candidate without influencing its absorption spectrum.

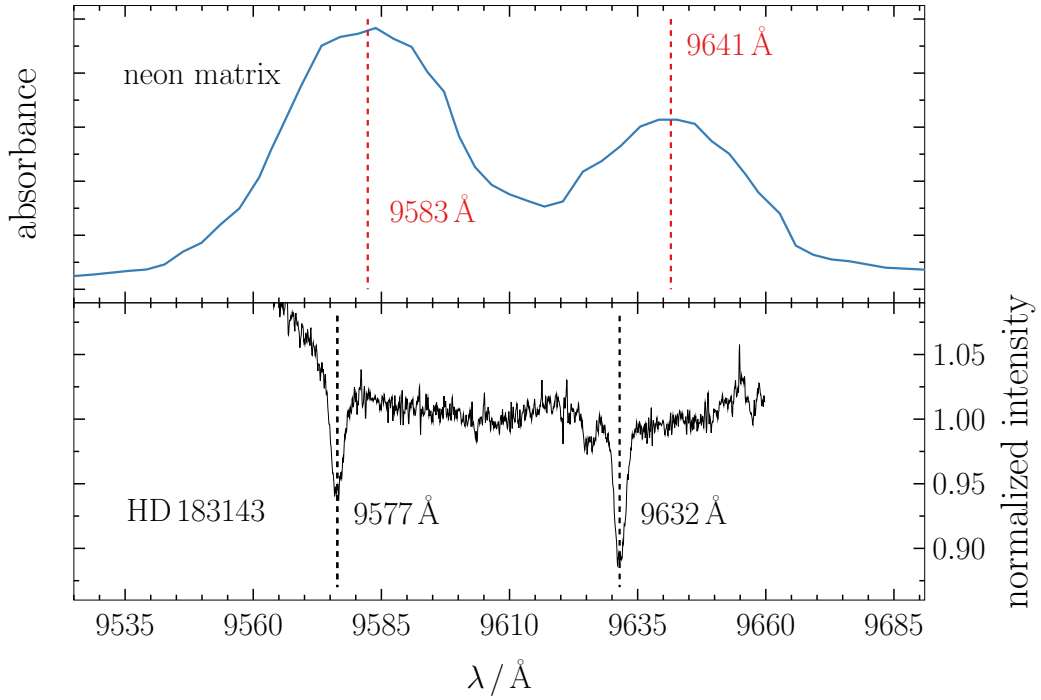


Figure 1.3: Comparison of the electronic spectra $C_{60}^{+}$ measured in neon matrix (upper trace) and the 9577/9632 DIBs recorded toward HD 183143 (lower trace). The data was reproduced from Ref. [39, 42]

## 1.3 Motivation and Thesis Structure

A low temperature ion trap combined with mass spectrometry has been used for preparing and spectroscopic probing fullerenes. Trapping methods have become an important tool in the field of spectroscopy of cold molecular ions [41]. Long interaction times with photons provided by lasers can circumvent insufficient densities of the investigated molecule. The cryogenic environment allows the attachment of a weakly bound helium atom to the species of interest and was used to record photofragmentation spectra of fullerene-helium complexes. Furthermore, the messenger technique enabled the development of a novel method called laser induced inhibition complex growth.

This thesis is structured in the following way: Chapter 2 provides insights in the used techniques of ion motion in radio-frequency fields and a brief history about spectroscopy together with relevant methods to probe ions. In Chapter 3 the apparatus employed is described in detail with several aspects of operating conditions. Two spectroscopic methods including a novel approach to measure electronics spectra are studied in Chapter 4. The photofragmentation spectra of weakly bound

fullerene complexes are presented in Chapter 5 and discussed in the context of astronomical observations of the DIBs, which is followed by an outlook.

# Bibliography


[1] T. P. Snow and B. J. McCall, "Diffuse atomic and molecular clouds", *Annual Review of Astronomy and Astrophysics*, vol. 44, pp. 367–414, 2006. DOI: 10.1146/annurev.astro.43.072103.150624.

[2] (2016). The cologne database for molecular spectroscopy: Molecules in space, [Online]. Available: https://www.astro.uni-koeln.de/cdms/molecules (visited on 08/17/2016).

[3] European Space Agency. (2014). Comet rendezvous, [Online]. Available: http://m.esa.int/Our_Activities/Space_Science/Rosetta/Comet_rendezvous (visited on 08/17/2016).

[4] NASA. (2011). Chemistry and the universe, [Online]. Available: http://www.chandra.harvard.edu/graphics/resources/handouts/lithos/chemistry_universe_litho.pdf (visited on 04/08/2016).

[5] M. L. Heger, "Further study of the sodium lines in class B stars", *Lick Observatory bulletin*, vol. 10, no. 337, pp. 141–145, 1922. DOI: 10.5479/ADS/bib/1922LicOB.10.141H.

[6] P. W. Merrill, "Unidentified interstellar lines", *Publications of the Astronomical Society of the Pacific*, vol. 46, no. 272, pp. 206–207, 1934. DOI: 10.1086/124460.

[7] P. Ehrenfreund and B. H. Foing, "Resolved profiles of diffuse interstellar bands: Evidence for rotational contours of gas-phase molecules.", *Astronomy and Astrophysics*, vol. 307, pp. L25–L28, 1996.

[8] P. Sonnentrucker, "Modern DIB surveys and DIB environmental behavior", in *Symposium S297 (The Diffuse Interstellar Bands)*, *Proceedings IAU Symposium*, Z. Knezević and A. Lemaitre, Eds., vol. 9, 2013, pp. 1–10. DOI: 10.1017/S1743921313015524.

[9] P. Jenniskens and F. Désert, "A survey of diffuse interstellar bands (3800-8680 Å)*", *Astronomy and Astrophysics Supplement Series*, vol. 106, pp. 39–78, 1994.

[10] P. Ehrenfreund, J. Cami, E. Dartois, and B. Foing, "Diffuse interstellar bands towards BD+63° 1964⋆", *Astronomy and Astrophysics*, vol. 317, pp. L28–L31, 1997.

[11] J. Cami, P. Sonnentrucker, P. Ehrenfreund, and B. Foing, "Diffuse interstellar bands in single clouds: EW families and constraints on the carriers", *Astronomy and Astrophysics*, vol. 326, pp. 822–830, 1997.

[12] B. T. Draine, "Interstellar dust grains", *Annual Review of Astronomy and Astrophysics*, vol. 41, pp. 241–289, 2003. DOI: 10.1146/annurev.astro.41.011802.094840.

[13] B. T. Draine and A. Li, "Infrared emission from interstellar dust. IV. The silicate-graphite-PAH model in the Post-Spitzer era", *The Astrophysical Journal*, vol. 657, no. 2, pp. 810–837, 2007. DOI: 10.1086/511055.

[14] K. Sellgren, "The near-infrared continuum emission of visual reflection nebulae", *The Astrophysical Journal*, vol. 277, pp. 623–633, 1984. DOI: 10.1086/161733.

[15] F. Salama, G. A. Galazutdinov, J. Krełowski, L. J. Allamandola, and F. A. Musaev, "Polycyclic aromatic hydrocarbons and the diffuse interstellar bands: A survey", *The Astrophysical Journal*, vol. 526, 1 1999. DOI: 10.1086/307978/.

[16] A. Léger and L. D'Hendecourt, "Are polycyclic aromatic hydrocarbons the carriers of the diffuse interstellar bands in the visible?", *Astronomy and Astrophysics*, vol. 146, pp. 81–85, 1 1985.

[17] G. P. van der Zwet and L. J. Allamandola, "Polycyclic aromatic hydrocarbons and the diffuse interstellar bands", *Astronomy and Astrophysics*, vol. 146, no. 1, pp. 76–80, 1985.

[18] M. K. Crawford, A. G. G. M. Tielens, and L. J. Allamandola, "Ionized polycyclic aromatic hydrocarbons and the diffuse interstellar bands", *The Astrophysical Journal*, vol. 293, pp. L45–L48, 1985. DOI: 10.1086/184488.

[19] A. Pathak and P. J. Sarre, "Protonated pahs as carriers of diffuse interstellar bands", *Monthly Notices of the Royal Astronomical Society*, vol. 391, 1 2008. DOI: 10.1111/j.1745-3933.2008.00544.x.

[20] V. L. Page, T. P. Snow, and V. M. Bierbaum, "Hydrogenation and charge states of polycyclic aromatic hydrocarbons in diffuse clouds. II. Results", *The Astrophysical Journal*, vol. 584, no. 1, 2003. DOI: 10.1086/345595/.

[21] S. Iglesias-Groth, A. Manchado, D. A. García-Hernández1, J. I. G. Hernández, and D. L. Lambert, "Evidence for the naphthalene cation in a region of the interstellar medium with anomalous microwave emission", *The Astrophysical Journal Letters*, vol. 685, no. 1, pp. L55–L58, 2008. DOI: 10.1086/592349.

[22] J. M. Searles, J. D. Destreeand, T. P. Snow, F. Salama, D. G. York, and J. Dahlstrom, "Searching for naphthalene cation absorption in the interstellar medium", *The Astrophysical Journal*, vol. 732, no. 1, pp. 1–6, 2011. DOI: 10.1088/0004-637X/732/1/50.

[23] J. Krełowski, Y. Beletsky, G. A. Galazutdinov, R. Kołos, M. Gronowski, and G. LoCurto, "Evidence for diacetylene cation as the carrier of a diffuse interstellar band", *The Astrophysical Journal Letters*, vol. 714, no. 1, pp. L64–L67, 2010. DOI: 10.1088/2041-8205/714/1/L64.

[24] J. Maier, S. Chakrabarty, F. Mazzotti, C. Rice, R. Dietsche, G. Walker, and D. Bohlender, "Assignment of 5069 Å diffuse interstellar band to $HC_4H^+$: Disagreement with laboratory absorption band", *The Astrophysical Journal Letters*, vol. 729, no. 2, pp. 1–4, 2011. DOI: 10.1088/2041-8205/729/2/L20.

[25] J. Maier, G. Walker, D. Bohlender, F. Mazzotti, R. Raghunandan, J. Fulara, I. Garkusha, and A. Nagy, "Identification of $H_2CCC$ as a diffuse interstellar band carrier", *The Astrophysical Journal*, vol. 726, no. 1, pp. 1–9, 2011. DOI: 10.1088/0004-637X/726/1/41.

[26] J. Krełowski, G. Galazutdinov, and R. Kołos, "Can $H_2CCC$ be the carrier of broad diffuse bands?", *The Astrophysical Journal*, vol. 735, no. 2, pp. 1–6, 2011. DOI: 10.1088/0004-637X/735/2/124.

[27] T. P. Snow, "Diffuse interstellar bands: Past and present", in *Symposium S297 (The Diffuse Interstellar Bands)*, Z. Knezević and A. Lemaitre, Eds., vol. 9, 2013, pp. 1–12. DOI: 10.1017/S1743921313015512.

[28] P. R. Buseck, "Geological fullerenes: Review and analysis", *Earth and Planetary Science Letters*, vol. 203, no. 3–4, pp. 781–792, 2002. DOI: 10.1016/S0012-821X(02)00819-1.

[29] H. W. Kroto, J. R. Heath, S. C. O'Brien, R. F. Curl, and R. E. Smalley, "C60: Buckminsterfullerene", *Nature*, vol. 318, pp. 162–163, 1985. DOI: 10.1038/318162a0.

[30] H. W. Kroto, "Chains and grains in interstellar space", in *Polycyclic Aromatic Hydrocarbons and Astrophysics*, A. Léger, L. d'Hendecourt, and N. Boccara, Eds., 191 vols. 1987, vol. 191, pp. 197–206. DOI: 10.1007/978-94-009-4776-4_17.

[31] R. B. Fuller, "Geodesic structures", US Patent 3,197,927, 1965.

[32] W. Krätschmer, L. D. Lamb, K. Fostiropoulos, and D. R. Huffman, "Solid $C_{60}$: A new form of carbon", *Nature*, vol. 347, pp. 354–358, 1990. DOI: 10.1038/347354a0.

[33] G. H. Herbig, "The search for interstellar $C_{60}$", *The Astrophysical Journal*, vol. 542, pp. 334–343, 2000. DOI: 10.1086/309523.

[34] S. Leach, "Spectroscopy and photophysics of possible large molecule carriers of the diffuse interstellar bands", in *The Diffuse Interstellar Bands*, A. G. G. M. Tielens and T. P. Snow, Eds. Springer Netherlands, 1995, pp. 281–305. DOI: 10.1007/978-94-011-0373-2_29.

[35] Y. Zhang and S. Kwok, "Detection of $C_{60}$ in the protoplanetary nebula IRAS 01005+7910", *The Astrophysical Journal*, vol. 730, no. 2, pp. 1–11, 2011. DOI: 10.1088/0004-637X/730/2/126.

[36] J. Cami, J. Bernard-Salas, E. Peeters, and S. E. Malek, "Detection of $C_{60}$ and $C_{70}$ in a young planetary nebula", *Science*, vol. 329, no. 5996, pp. 1180–1182, 2010. DOI: 10.1126/science.1192035.

[37] K. Sellgren, M. W. Werner, J. G. Ingalls, J. D. T. Smith, T. M. Carleton, and C. Joblin, "$C_{60}$ in reflection nebulae", *The Astrophysical Journal Letters*, vol. 722, no. 1, pp. L54–L57, 2010. DOI: 10.1088/2041-8205/722/1/L54.

[38] B. H. Foing and P. Ehrenfreund, "Detection of two interstellar absorption bands coincident with spectral features of $C_{60}^+$", *Nature*, vol. 369, pp. 296–298, 1994. DOI: 10.1038/369296a0.

[39] J. Fulara, M. Jakobi, and J. P. Maier, "Electronic and infrared spectra of $C_{60}^+$ and $C_{60}^-$ in neon and argon matrices", *Chemical Physics Letters*, vol. 211, no. 2–3, pp. 227–234, 1993. DOI: 10.1016/0009-2614(93)85190-Y.

[40] M. E. Jacox, "The spectroscopy of molecular reaction intermediates trapped in the solid rare gases", *Chemical Society Reviews*, vol. 31, no. 2, pp. 108–115, 2002. DOI: 10.1039/B102907J.

[41] R. Wester, "Radiofrequency multipole traps: Tools for spectroscopy and dynamics of cold molecular ions", *Journal of Physics B: Atomic, Molecular and Optical Physics*, vol. 42, no. 15, pp. 1–12, 2009. DOI: 10.1088/0953-4075/42/15/154001.

[42] B. H. Foing and P. Ehrenfreund, "New evidences for interstellar $C_{60}^+$", *Astronomy and Astrophysics*, vol. 317, pp. L59–L62, 1997.

# 2

*The aim of science is to make difficult things understandable in a simpler way; the aim of poetry is to state simple things in an incomprehensible way.*

Paul M. A. Dirac

# Methodology

Spectroscopic studies of ions are intrinsically problematic. Apart from the sufficient production of the species, a sensitive detection technique to record their spectra is necessary. Ion trapping methods have evolved as a standard tool to prepare molecular ions in a well-defined state [1, 2]. Parameters like storage time, buffer gas density and trap temperature can be adjusted to the needs of the experiment. Probing of even large molecules like proteins at low concentrations revealed the capabilities of ion confinement combined with spectroscopy [3].

## 2.1 Ion Motion in Multipole RF-Fields

The force acting on a particle with charge $q$ in the presence of an electromagnetic field and in the absence of any further perturbations (gravitation, collisions etc.) is described by the Lorentz force

$$\vec{F} = q\vec{E}(\vec{r},t) + \frac{\dot{\vec{r}}}{c} \times \vec{B}(\vec{r},t). \tag{2.1}$$

The fields depend on the spatial and temporal coordinates of the particle. A contribution of the magnetic term can be neglected as the velocities of atomic or molecular ions are expected to be much slower than the speed of light. The electric field $\vec{E}$ is described by Maxwell's equations

$$\nabla \cdot \vec{E} = \frac{\rho}{\epsilon_0} \tag{2.2}$$

and

$$\nabla \times \vec{E} = 0. \tag{2.3}$$

The density $\rho$ of charged particles is usually low and therefore, equation (2.2) can be simplified. The second equation states that $\vec{E}$ is the gradient of a scalar function

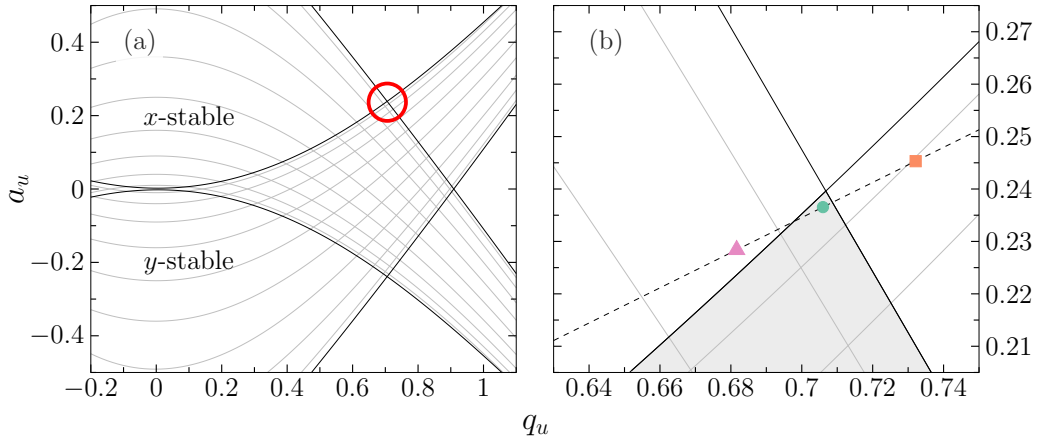


Figure 2.1: (a) Part of the Mathieu stability diagram in $(a_u, q_u)$ space for the linear quadrupole ($\alpha = -\beta, \gamma = 0$). The region of simultaneous overlap allow $x$- and $y$-stable conditions. The region at the cusp (◯) of the mass selective mode is enlarged in (b). Three different particles with $m/z = 27$ (▲), 28 (●), and 29 (■) are indicated with their positions in the diagram, all other parameters that define $(a_u, q_u)$ are kept the same. Only $m/z = 28$ exhibits $x, y$-confinement, while the other two particles possess unstable trajectories.

$\Phi$,

$$\vec{E} = -\nabla\Phi, \tag{2.4}$$

and is derived from the generalized Coulomb law (see e.g. Ref.[4]). Equations (2.4) and (2.2) can be combined into one partial differential equation, Laplace's equation

$$\nabla^2\Phi = 0. \tag{2.5}$$

Once the potential $\Phi$ is known, the motion of a charged particle is expressed by Newton's equation of motion

$$\vec{F} = m\ddot{\vec{r}} = q\nabla\Phi. \tag{2.6}$$

### 2.1.1 Mass Filtering in a Quadrupole

A quadrupole mass filter uses an oscillating radio-frequency field to selectively transport ions of a specific mass-to-charge ratio. It is ideally constructed from four electrically parallel hyperbolic cylindrical surfaces. An electric potential for this case is given by

$$\Phi(x, y, z) = \frac{\Phi_0}{r_0}(\alpha x^2 + \beta y^2 + \gamma z^2). \tag{2.7}$$

Parameters $\alpha, \beta$, and $\gamma$ are weighting constants for the three coordinates and $r_0$ defines the distance from the center of the trap to an electrode. The applied electric potential $\Phi_0$ is a combination of a static and a time varying potential

$$\Phi_0 = U_0 + V_0 \cos(\Omega t). \tag{2.8}$$

The potential $\Phi$ has to fulfill the Laplace's equation (2.5) at every instant in time. An important consequence is that no local three dimensional minimum in free space can be generated. Furthermore, it is found that

$$\alpha + \beta + \gamma = 0, \tag{2.9}$$

from which various situations can be constructed. For a mass filter the choice will be $\alpha = -\beta = 1$ and $\gamma = 0$. These values lead to confinement in the $x$-$y$ plane and free motion in $z$ direction. The equations of motion (2.6) are then decoupled

$$\ddot{x} + \frac{e}{mr_0^2}\left[U_0 - V_0 \cos(\Omega t)\right] x = 0 \tag{2.10}$$

$$\ddot{y} - \frac{e}{mr_0^2}\left[U_0 - V_0 \cos(\Omega t)\right] x = 0 \tag{2.11}$$

$$\ddot{z} = 0. \tag{2.12}$$

By substituting

$$\zeta = \frac{\Omega t}{2}, \quad a_u = \frac{8eU_0}{m\Omega^2 r_0}, \text{ and } \quad q_u = \frac{4eV_0}{m\Omega^2 r_0} \tag{2.13}$$

they can be transformed into the Mathieu differential equation

$$\frac{d^2u}{d\zeta^2} + \left[a_u - 2q_u \cos(2\zeta)\right] = 0, \tag{2.14}$$

where labels $u$ represent one of the corresponding Cartesian coordinates. The Mathieu equation belongs to the class of differential equations with periodic coefficients and their solutions are of two types: Periodic but unstable, and periodic and stable. Parameters $a$ and $q$ characterize stable trajectories of ion confinement and the conditions for optimal mass selection. The operation of a quadrupole can be visualized in a stability diagram as shown in (a) of Figure 2.1. In case of $U_0 = 0$, all ions irrespective of their mass to charge ratio are guided along the $z$-axis. By adding a static potential, the region closer to the cusp of the triangle has to be considered is shown in (b) of Figure 2.1. This is the region of the mass filtering mode, where only specific $m/z$ ratios provide simultaneous $x, y$- stable confinement.

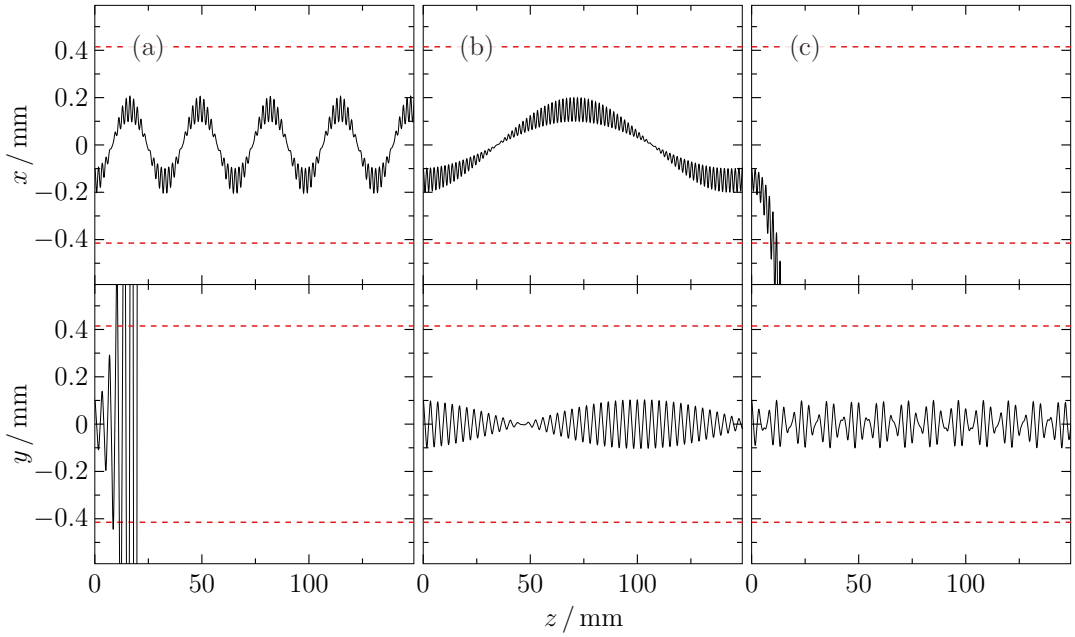


Figure 2.2: Trajectories of particles $m/z = 27$, 28, and 29 in the regions exhibiting (a) $y$ instability, (b) no instability, and (c) $x$ instability. For all simulations $E_{\text{kin}} = 600\,\text{meV}$, $U_0 = 8.395\,\text{V}$, $V_0 = 50.11\,\text{V}$, $f = 1.2\,\text{MHz}$, and initial particle position $y_0, x_0 = \pm 0.1\,\text{mm}$. The dashed lines (--) indicate the boundaries $r_0$ of the quadrupole.

Simulations of trajectories for particles using an ideal, infinitely long quadrupole are shown in Figure 2.2. These are calculated for the three masses $m/z = 27$, 28, and 29 as indicated in Figure 2.1 (b).

### 2.1.2 Ion Trapping

Two different ion traps have been used for the experiments presented in this thesis, a quadrupole and a 22-pole trap. For the former, the parameters in equation (2.7) can be changed such that the potential is written as

$$\Phi(x, y, z) = \frac{\Phi_0}{r_0}(x^2 - y^2 - 2z^2), \tag{2.15}$$

which allows confinement in the $x, y$ and $z$-direction. However, for higher order multipoles the equations of motion in the time-dependent field are no longer decoupled and analytical solutions do not exist. The position of a particle $\vec{r}(t)$ can be expressed by a composition of two motions [5]:

$$\vec{r}(t) = \vec{R}_0(t) + \vec{R}_1(t). \tag{2.16}$$

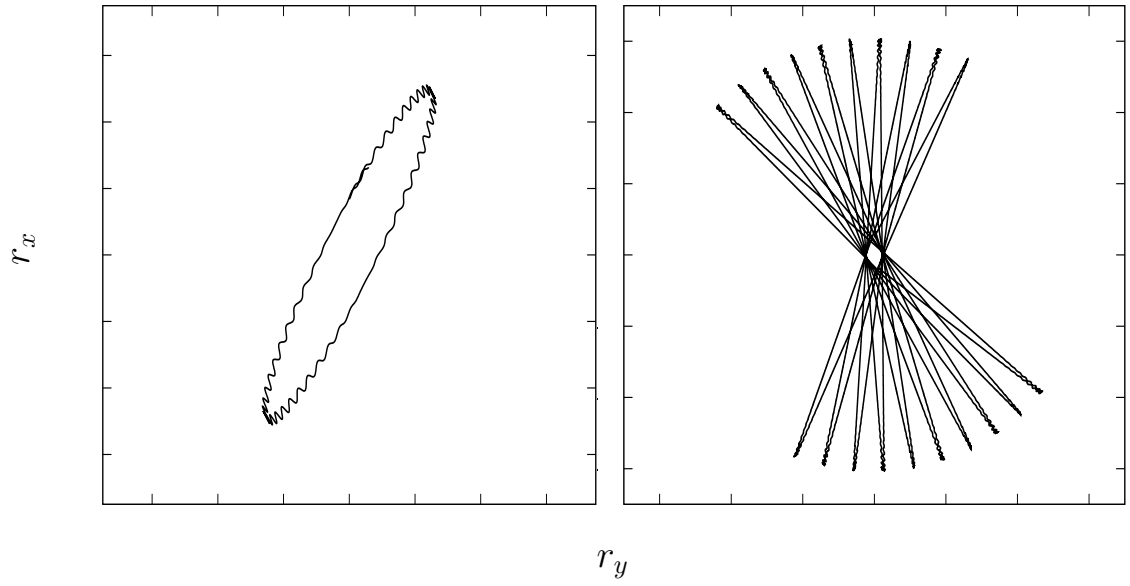


(a) (b)

Figure 2.3: Typical radial trajectory of an ion in a quadrupole (a) and a 22-pole (b) simulated by integrating the equation of motion using a velocity verlet algorithm.

The second term defines a rapidly oscillating motion with amplitude A(t)

$$\vec{R}_1(t) = \vec{A}(t)\cos(\Omega t). \tag{2.17}$$

The first term is the contribution of a slow varying drift in the location of the particle. A second order Taylor expansion for the electric field $\vec{E}_0(\vec{r}(t))$ yields for the time averaged case the differential equation of a non-oscillating motion $\vec{R}_0(t)$

$$m\ddot{\vec{R}}_0 = -\frac{q^2}{4m\Omega^2}\nabla E_0^2. \tag{2.18}$$

Equation (2.18) describes a charged particle that experiences a force which pushes it toward weaker fields. By adding a static potential an equation is obtained which is known as the effective or pseudo potential:

$$V_{\text{eff}} = \frac{qE_0^2}{4m\Omega^2} + q\Phi_{\text{static}} \tag{2.19}$$

In a last step expressions for the components $E_0$ and $\Phi_{\text{static}}$ have to be found. As the problem obeys no $z$-dependence, the solutions can be described in plane polar coordinates $(r, \varphi)$ and for the ideal multipole in two dimensions it has been shown

that the effective potential is given by [5]

$$V_{\text{eff}} = \frac{(qnV_0)^2}{4m\Omega^2 r_0^2} \left(\frac{r}{r_0}\right)^{2n-2}. \tag{2.20}$$

From this formula it becomes obvious, that with increasing $n$ large radial field-free regions with steep walls can be achieved.

The total kinetic energy was assumed to be an adiabatic constant of the particle motion. Therefore, multipole stable and unstable conditions exist. Similar to the $(a, q)$ stability parameters for the quadrupole trap, an adiabaticity parameter is introduced. This empirical quantity is derived to

$$\eta = 2n(n-1)\frac{qV_0}{m\Omega^2 r_0^2} \left(\frac{r}{r_0}\right)^{n-2}. \tag{2.21}$$

Stable confinement is obtained for $\eta < 0.3$ at a critical radius of $r_{\max}/r_0 \leq 0.8$. Two stable radial ion trajectories are shown in Figure 2.3 for $m/z = 28$. Close to the turning points, where the inhomogeneous field repels the ion, a micromotion becomes visible. A region which is avoided by the ion trajectories is found in the center. This is a consequence of the rotational symmetry of the potential, which leads to conservation of angular momentum.

## 2.2 Buffer Gas Cooling of Ions

A major advantage of confined ions in traps is the possibility of relaxing the translational and internal degrees of freedom by collisions with a neutral buffer gas. The velocity distribution of a gas is well represented by a Maxwell-Boltzmann distribution

$$f(v) = 4\pi \left(\frac{m}{2\pi k_{\text{B}} T}\right)^{3/2} v^2 \exp\left(-\frac{m}{2k_{\text{B}} T} v^2\right). \tag{2.22}$$

In ion traps, translational temperatures of buffer gas and ions usually deviate and the distribution of the ensemble is approximated by two Maxwellians with temperatures $T_1$ and $T_2$. From this, a mass weighted collision temperature reflecting the internal temperature of the ion can be estimated with [6]:

$$T_{\text{int}} = (m_2 \cdot T_1 + m_1 \cdot T_2)/(m_1 + m_2). \tag{2.23}$$

In order to achieve efficient cooling, the mass and temperature of the buffer gas have to be low. For the presented experiments helium has been the first choice as it fulfills these requirements. Additionally, it is chemically inert, has a high ionization

threshold, and posses a high enough vapor pressure at cryogenic temperatures ($T_{\mathrm{nom}} < 10\,\mathrm{K}$) [7]. Depending on buffer gas densities achieved in the trap, sufficient collisions are provided to equilibrate the internal temperature of the ion to that of the buffer gas. This is a major advantage compared to cooling in supersonic expansion. Especially in the case of large molecules it has been shown to be inefficient of relaxing their internal energy [8]. With spectroscopic methods it is possible to determine $T_{\mathrm{int}}$ if rotational resolution can be achieved.

## 2.3 Electronic Spectroscopy

The term spectrum goes back to the $17^{\mathrm{th}}$ century when Sir Isaac Newton described the appearance of colors produced by narrow beam of sunlight passing a prism. In 1814 Joseph von Frauenhofer found that the dispersed solar spectrum observed by Newton is congested with fine dark lines (Figure 2.4). The lines have not be seen by Newton, as he used a pinhole instead of a slit before passing the prism offering higher resolution. These were the first spectral lines observed and marked the beginning of modern spectroscopy. Frauenhofer extended his experiments by using in addition a telescope for investigating other interstellar objects establish astronomical spectroscopy. Despite his many developments in optics such as the diffraction grating, he did not understand the origin of the lines. Several scientists have investigated the spectra of sources like flames or arcs, and found that these sources emit bright spectral lines, which were characteristic for the chemical elements in the flame. A first theoretical description was provided by Gustav Kirchhoff, who stated that the emitted and absorbed power of light at a given wavelength are the same for all bodies at the same temperature. With this knowledge, Kirchhoff and Robert W. Bunsen could explain the observed Frauenhofer lines by absorption of a continuous spectrum emitted from the sun by the elements in the atmosphere.

A qualitative theoretical interpretation by classical considerations failed to explain the observed absorption features and measured spectral densities of hot light emitting objects. In 1900 Max Planck introduced the idea that light is absorbed and emitted in discrete energy quanta. A single photon keeps an energy that is proportional to its frequency multiplied with a constant

$$E = h\nu. \tag{2.24}$$

This finding marked a new era in science as it was then possible to develop a new theory named "Quantum Mechanics". The time-dependent evolution of a quantum


Figure 2.4: Stamp dedicated to the 200 th birthday of Joseph von Frauenhofer. Indicated is the solar spectrum with the Frauenhofer lines.

system is explained by a differential equation suggested by Erwin Schrödinger in 1926:

$$\hat{H}\Psi = i\hbar\frac{\partial\Psi}{\partial t}. \tag{2.25}$$

The central concept of this equation is that of a wave function $\Psi$. It describes a system composed of $N$ particles in a certain state, where the classical deterministic approach is replaced by expectation values. The probability of finding a particle at a position $\vec{r}$ at a time $t$ is given by

$$p(\vec{r},t) = |\Psi(\vec{r},t)|^2\,, \tag{2.26}$$

whose integral over the full space has to be 1 in order to fulfill the normalization condition. For a particle of mass $m$ in a potential $V(\vec{r},t)$ equation (2.25) is written as

$$-\left(\frac{\hbar^2}{2m}\frac{\partial^2}{\partial\vec{r}^2} + V(\vec{r},t)\right)\Psi(\vec{r},t) = i\hbar\frac{\partial\Psi(\vec{r},t)}{\partial t}, \tag{2.27}$$

and a general solution can be constructed by a linear combination of plane waves

$$\Psi(\vec{r},t) = \sum_i c_i \exp\left(-iE_it/\hbar\right)\psi_i(\vec{r}). \tag{2.28}$$

The result is obtained by the fact, that the probability (2.26), as well as the expectation value of any time-independent operator $\hat{A}$ are time-independent. Only certain values of $E$ lead to normalizable solutions which are called eigenvalues of $\Psi$.

Thus, the state described by $\Psi$ is stationary although the particle it describes is not.

To find an analytical solution of equation (2.27) for more than a single particle, e.g. a diatomic molecule, is challenging as the nuclear and electronic motions are coupled. However, in many situations it can be assumed that the wave function depends only on a fixed position of the nuclei as the electron velocity is much faster. This is called the Born-Oppenheimer approximation and allows an individual evaluation of their contributions using a product Ansatz for the wave function. If all interactions between electrons and nuclei are neglected the total wave function is given by

$$\Psi_{\mathrm{tot}} = \Psi_{\mathrm{el}}(\vec{r}) \times \Psi_{\mathrm{nuc}}(\vec{R}), \tag{2.29}$$

with $\vec{r}$ and $\vec{R}$ as the position vector of the electron and nuclei, respectively. The total energy of the system is determined by the sum of kinetic energy of nuclei and the electronic energy and can be expressed by

$$E_n = E_n^{\mathrm{el}}(\vec{R}) + E_{\mathrm{vib}}(\vec{R}) + E_{\mathrm{rot}}(\vec{R}), \tag{2.30}$$

where $n$ is the electronic state. Each electronic level has a set of vibrational levels and each of these states have multiple rotational levels reflecting the internal degrees of freedom of a molecule. This can be illustrated by the concept of the potential energy surface along a certain nuclear axis as shown in Figure 2.5 for a diatomic molecule. The energy spacing between vibrational levels in the quantum harmonic oscillator is constant at $h\omega_0$, whereas in a molecule the energy between adjacent levels decreases with increasing $v$ due to nonlinear oscillation. Rotational absorption or emission lies in the microwave region of the electromagnetic spectrum. The largest energies are between the rovibrational transitions of two electronic states between NIR and the deep UV.

A molecular term symbol

$$^{2|\Sigma|+1}|\Lambda|^{\pm}_{g/u} \tag{2.31}$$

denotes the electronic state, similar to atomic ones, providing the information of the total spin $\Sigma$, reflection symmetry ($\pm$), electronic parity ($g/u$) and projection of the total angular momentum $\Lambda$. Moreover, the electronic states are labeled with $X$ for the ground state and $A, B, C, ...$ for the excited states in ascending order of energy. Molecules posses a variety of angular momenta which can couple to one another and strongly influence the molecular energy level structure. A set of rules, known as Hund's cases, are used to determine the involved couplings [9]. For a fixed

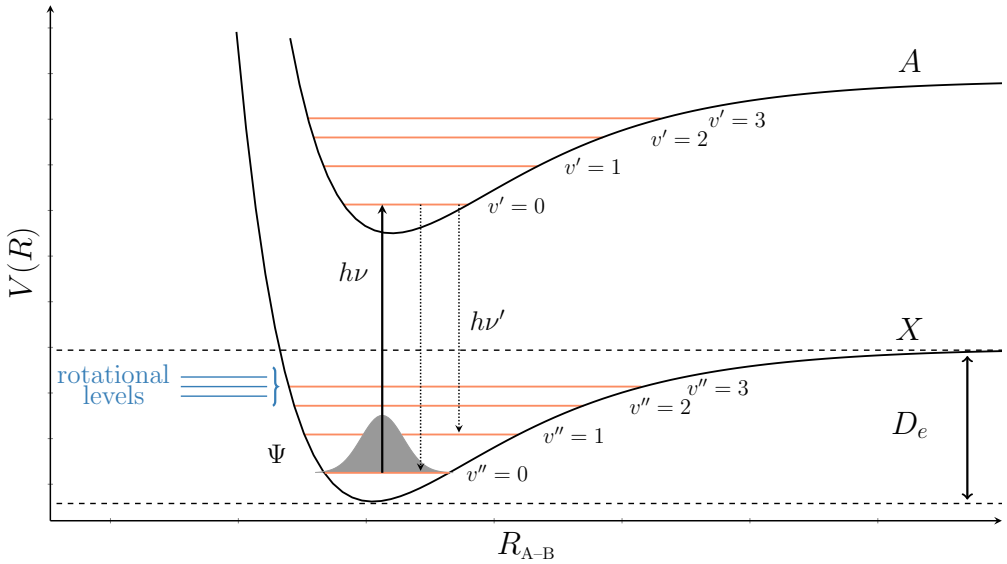


Figure 2.5: Schematic of a potential energy curve (–) for two electronic states $X$ and $A$ of a diatomic molecule with indicated vibrational (–) and rotational levels (–). The binding energy $D_e$ is larger than the dissociation energy $D_0$ due to the zero point energy of the lowest vibrational level ($v'' = 0$).

distance between two atoms, $R$, the Hund's cases are classified according to the relative strengths of three basic interactions present in the molecular Hamiltonian. These are the electrostatic coupling of the orbital angular momentum **L** to the molecular axis, the coupling between **L** and the electron spin **S**, and the coupling of **L** and **S** to the total angular momentum **J**. Five different cases (a-e) can be derived from three different strengths (strong, intermediate, weak) of the couplings defining a good set of quantum numbers.

### 2.3.1 The Franck-Condon Principle

The strength of an electronic transition is estimated in first order by the dipole moment operator $\mu$ and is proportional to

$$M = \int \Psi''_{\text{el}} \hat{\mu} \Psi'_{\text{el}} d\tau = \langle e'' v'' | \hat{\mu} | e' v' \rangle, \tag{2.32}$$

where the integration is over the electronic and nuclear coordinates. The total dipole moment operator $\hat{\mu}$ is the sum of nuclear and electronic dipole moment

operators, and within the Born-Oppenheimer approximation

$$\langle e''v''|\hat{\mu}|e'v'\rangle = \langle e''v''|\hat{\mu}_{\mathrm{el}} + \hat{\mu}_{\mathrm{nu}}|e'v'\rangle \tag{2.33}$$

$$\approx \langle v''|v'\rangle\langle e''|\hat{\mu}_{\mathrm{el}}|e'\rangle + \langle e''|e'\rangle\langle v''|\hat{\mu}_{\mathrm{nu}}|v'\rangle \tag{2.34}$$

is valid. For simplification, the spin wave function has been neglected. The second term vanishes as the electronic wave functions are orthonormal. The product $\langle v''|v'\rangle$ is defined as the overlap integral or Franck-Condon factor. A remaining integral is the transition dipole moment and exhibits the orbital selection rule. Therefore, the relative intensity of a transition between two vibrational states is given by the square of the overlap integral.

For electronic transitions in absorption, the oscillator strength $f_{osc}$ is used. It is determined by the integral of the frequency dependent absorption cross-section of an electronic transition

$$f_{osc} = 4\frac{\epsilon_0 m_{\mathrm{e}} c}{e^2}\int \sigma(\nu)d\nu. \tag{2.35}$$

For an absorption band with a Gaussian profile, $f$ can be estimated by

$$f_{osc} = 2\frac{\epsilon_0 m_{\mathrm{e}} c}{e^2}\cdot\sigma\cdot\Delta\nu\cdot\sqrt{\frac{2\pi}{\ln(4)}}, \tag{2.36}$$

where $\Delta\nu$ is the FWHM in Hz and $\sigma$ the absorption cross-section in $\mathrm{m}^2$. The dimensionless oscillator strength has a value between 0 and 1 and can be interpreted as the ratio of the strength of the absorption/emission to the strength of a single electron using a harmonic oscillator [10].

The previous discussions were only valid for diatomic molecules. In the case of polyatomics, the treatment is more complicated. For totally symmetric vibrations the principles are similar, except that one has to account for each normal mode. As the electronic transition is assumed to be fast compared to the vibrational motion, progressions appear in the spectrum upon geometrical changes.

### 2.3.2 Selection Rules

The transition between two states is constrained by selection rules. In general, the integral in equation (2.32) defines an "allowed" electronic transition. In practice it is sufficient to show that the direct product $\Psi''_{\mathrm{el}}\hat{\mu}\Psi'_{\mathrm{el}}$ spans the totally symmetric

irreducible representation of the point group to which the molecule belongs

$$\Gamma(\Psi''_{\mathrm{el}}) \times \Gamma(\hat{\mu}_{\mathrm{el}}) \times \Gamma(\Psi'_{\mathrm{el}}) = A_{(1,g)}. \tag{2.37}$$

Further selection rules are derived from the Hund's coupling cases which include total angular momentum and spin. If the spin-orbit coupling is not large (cases a,b), the electronic spin wave function can be separated from the electronic wave functions. As a result, the spin multiplicity should not change during the electronic dipole transition and

$$\Delta S = 0. \tag{2.38}$$

## 2.4 Spectroscopic Methods

The techniques used to investigate the rotational, vibrational or electronic structure of a molecule can be categorized in two classes. One is based on the attenuation in light intensity following the principle of the well-known Beer-Lambert law and is thus called direct methods. Indirect methods make use of all other phenomena which can be observed as a consequence of photon absorption processes. These can be, e.g., the emission of light as an internal relaxation process or the fragmentation of a molecule. As light sources especially lasers have evolved as a standard tool. They offer high spectral intensities and narrow linewidths. The availability of ultrashort pulses including pulse shaping have enabled a vast number of special spectroscopic techniques.

### 2.4.1 Absorption Spectroscopy

If a flux of photons $F$ travels through a system of molecules, photons can be absorbed or induce stimulated emission. This can be expressed in a steady state approximation of a two level system with populations $N_i$ by the rate equation

$$\frac{dN_1}{dt} = -B_{10}\rho N_1 + B_{01}\rho N_0 \tag{2.39}$$

with Einstein coefficients

$$B_{10} = B_{01} = \frac{2\pi^2}{3\epsilon_0 hc^3}\mu_{10}^2 g(\nu - \nu_{10}). \tag{2.40}$$

Factors $\rho$ denote the radiation density and $g(\nu - \nu_{10})$ the line shape function describing an absorption profile. Equation (2.39) can be simplified by introducing a

quantity which represents an effective area that the molecule opposes to the stream of photons called absorption cross-section

$$\sigma_{\mathrm{M}} = \frac{2\pi^2 \mu_{10}^2}{3\epsilon_0 hc} \nu g(\nu - \nu_1 0), \tag{2.41}$$

leading to

$$\frac{dN_1}{dt} = \sigma_{\mathrm{M}} F(N_0 - N_1). \tag{2.42}$$

The change in flux along a small element of thickness $dx$ is then given by

$$dF = -\sigma_{\mathrm{M}} F(N_0 - N_1) dx. \tag{2.43}$$

Integration over the full length $L$ of an absorber and by replacing the flux with intensity results in the Beer-Lambert law

$$I = I_0 \exp\{-\sigma_{\mathrm{M}}(N_0 - N_1)L\}. \tag{2.44}$$

This is the basic principle of techniques such as Matrix Isolation or Cavity Ring-Down spectroscopy.

### 2.4.2 Photodissociation Spectroscopy of Weakly Bound Complexes

A method employed in this thesis belongs to the group of indirect methods. The principle is based on fragmentation upon photon absorption

$$XYZ + h\nu \rightarrow XY + Z. \tag{2.45}$$

In the case of single photon absorption, usually in the UV/VIS or NIR, a molecule is promoted from the ground electronic to an excited electronic state. Depending on the shape of the excited state potential along the dissociation bond, a molecule will fall apart immediately on a time-scale smaller than a typical internal vibrational period, or after a particular lifetime. Indirect or delayed dissociation requires that a molecule is trapped for some time, either by a potential barrier or a dynamical effect, before sufficient energy is accumulated in the dissociation coordinate, enabling the bond to break [11]. Immediate dissociation occurs if the excited potential energy curve is purely repulsive. A molecule starts its motion in the upper electronic state from the Franck-Condon point until the fragments are irreversibly formed. In multiphoton dissociation, several photons, mostly in the IR region,

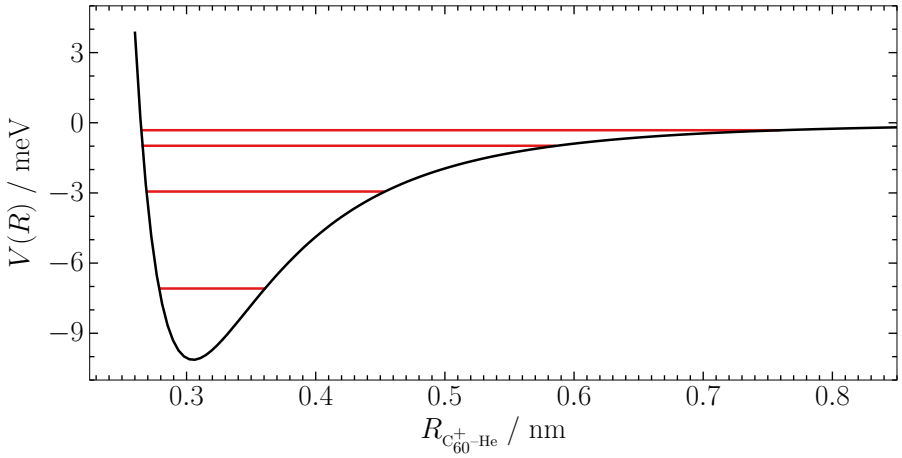


Figure 2.6: Averaged potential energy curve of $C_{60}^+$–He (–) obtained from ion mobility measurements, with calculated bound states (–). Potential reproduced from [18].

excite the molecule until the energy exceeds the dissociation energy. Generally it is a background free technique as fragments are only detected when an absorption event occurs.

Polyatomic cations are considered to be very stable due to fast internal non-radiative transitions. For example, $C_{60}^+$ can store up to $\sim 45\,\mathrm{eV}$ of internal energy and would require multiple photons to fragment [12]. Consequently, a high laser fluence is necessary to provide enough photons leading to saturation or nonlinear absorption effects. This constraint can be circumvented by attaching a weakly bound rare gas atom (or molecule) to the species of interest. The ejection of the messenger results from intermolecular energy transfer within the complex. The formation of such complexes are well established in IR and electronic spectroscopy and only small deviations to the spectrum of the unperturbed molecule are expected [13–17]. Helium appears to be the best candidate for fullerenes as the potential energy curve of $C_{60}^+$–He is extremely shallow with $\sim 10$ meV (Figure 2.6). Only three vibrational modes are obtained before reaching the continuum.

In ion traps the complexes are usually formed by a three-body collision process

$$X^+ + 2Y \underset{k_{\mathrm{CID}}}{\overset{k_3}{\rightleftharpoons}} [X^+ - Y] + Y \tag{2.46}$$

where $k_3$ denotes the ternary rate coefficient. Typical values range from $10^{-26}$ to $10^{-30}\,\mathrm{cm^6 s^{-1}}$, at suitable temperatures below 10 K, depending on the binding energy of the ion-neutral compound. The stationary equilibrium is determined by

the reverse bimolecular process, which is called collision induced dissociation.

Resonant absorption of radiation by the complex leads to vibrational predissociation and an ultimate change in the ion concentration. Thus, the spectroscopy of the cation can be studied by mass selective monitoring of the attenuation in the $X^+$–He ion yield as a function of a laser frequency. A connection between equation (2.44) to the observed ion signal can be derived assuming that a single photon leads to dissociation. In that case, the loss of complexes is given by

$$N = N_0 \exp(-\sigma N_{\mathrm{ph}}), \tag{2.47}$$

where $N_0$ is the number of complexes, $N_{\mathrm{ph}}$ the number of absorbed photons per area, and $\sigma$ the total absorption cross-section. Typical values involved in electronic transitions are $10^{-14}$ to $10^{-17}\,\mathrm{cm}^2$. In practice neither absorption cross-section nor the number of photons are measured directly [16]. However it is possible to replace these by accessible quantities

$$N_{\mathrm{ph}} = \frac{P\Delta t}{A} \cdot \frac{1}{E_{\mathrm{ph}}}, \tag{2.48}$$

where $P$ is laser power, $\Delta t$ irradiation time, $A$ irradiated area, and $E_{\mathrm{ph}}$ the photon energy. By further substituting

$$\Phi = \frac{P\Delta t}{A} \text{ and } \Phi_0 = \frac{E_{\mathrm{ph}}}{\sigma} \tag{2.49}$$

equation (2.47) changes to

$$N(\Phi) = N_0 \exp\left(-\frac{\Phi}{\Phi_0}\right), \tag{2.50}$$

which describes the number of remaining complexes $N$ after irradiation by a laser fluence $\Phi$. An absorption cross section can be estimated from the characteristic fluence $\Phi_0$ obtained from the attenuation at a fixed wavelength.

### 2.4.3 Line-Shape Functions

The transition between two states is not observed as an infinitely sharp line in the spectrum, but exhibits a finite band structure. Several effects others than instrumental can contribute to the characteristic profile of the observed absorption. In the following, relevant factors causing specific shapes are discussed.

### Natural Lifetime Broadening

The release of a molecule's excitation energy by spontaneous emission can be described by a damped harmonic oscillation with a damping constant $\gamma$. The equations of motions are well-known and its solution yields for the approximation $\gamma << \omega_0$

$$x(t) = x_0 \exp\left(-\frac{\gamma t}{2}\right) \cos(\omega_0 t), \tag{2.51}$$

where $\omega_0 = 2\pi\nu_c$ corresponds to the central frequency of the transition. A Fourier transformation shows that the decrease in amplitude causes a frequency distribution whose shape is represented by a Lorentz function

$$g_L(\nu - \nu_c) = \frac{\gamma}{(2\pi)^2(\nu - \nu_c)^2 + (\gamma/2)^2}. \tag{2.52}$$

The linewidth is

$$\Delta\nu_L = \frac{\gamma}{2\pi} = \frac{1}{\tau}, \tag{2.53}$$

where $\tau$ is related to the lifetime of the excited state and can be derived from Heisenberg's uncertainty relation.

### Doppler Broadening

A moving atom or molecule that interacts with an electromagnetic wave sees a Doppler-shifted frequency $\nu' = \nu(1 \pm v/c)$. In a laboratory experiment the ions have a distribution of different velocities at a certain temperature. This is expressed by the Maxwell-Boltzmann distribution and leads to an inhomogeneous lineshape function

$$g_{\mathrm{D}}(\nu - \nu_c) = \frac{1}{\nu_c}\sqrt{\frac{mc^2}{2\pi k_{\mathrm{B}} T}} \cdot \exp\left(\frac{mc^2(\nu - \nu_c)^2}{2k_{\mathrm{B}} T \nu_c^2}\right). \tag{2.54}$$

By substituting the full-width-at-half-maximum

$$\Delta\nu_{\mathrm{D}} = 2\nu_c\sqrt{\frac{2k_{\mathrm{B}} T \ln(2)}{mc^2}} \tag{2.55}$$

in equation (2.54), the typical Gaussian function is obtained. If a transition is Doppler broadened, equation (2.55) allows the calculation of the average temperature of the probed ensemble.

### Power Broadening

The use of very intense radiation in spectroscopic measurements leads to a line broadening, or even splitting. This effect is observed when the optical pumping exceeds the relaxation rates. The transition of the molecule undergoes Rabi oscilla-

tion at high fluences with a frequency $\Omega_{\mathrm{R}} = \mu_{10}E/\hbar$. In a semiclassical picture the factor $\mu_{10}$ describes an oscillating dipole. Assuming spontaneous decay processes, a (normalized) Lorentz line shape is obtained [19]:

$$g_{\mathrm{L}}(\nu) = \frac{1}{4(\nu - \nu_c)^2/\Delta\nu_{\mathrm{PB}}^2 + 1} \tag{2.56}$$

The FWHM is now broadened by the lifetime given by the Rabi frequency $\Omega_{\mathrm{R}}$. With the Heisenberg relation

$$\Delta E \Delta t \geq \hbar \tag{2.57}$$

and a period of $\Delta t \sim \mu_{10}E/h$ for the system oscillating in the excited state yields

$$\Delta E \frac{h}{\mu_{10}E} \sim \hbar. \tag{2.58}$$

Furthermore is $h\Delta\nu = \Delta E$ and thus

$$\Delta\nu_{\mathrm{PB}} \sim \frac{\mu_{10}E}{2\pi h}. \tag{2.59}$$

For photofragmentation experiments an observed power broadened line shape for an absorption band can be expressed with equation (2.50) by

$$\frac{N(\nu)}{N_0} = \exp\left(-g_L(\nu)\frac{\Phi}{\Phi_0}\right). \tag{2.60}$$

This equation allows a correction of a broadened FWHM if the characteristic fluence $\Phi_0$ is known.

# Bibliography


[1] S. Willitsch, "Coulomb-crystallised molecular ions in traps: Methods, applications, prospects", *International Reviews in Physical Chemistry*, vol. 31, no. 2, pp. 175–199, 2012. DOI: 10.1080/0144235X.2012.667221.

[2] R. Wester, "Radiofrequency multipole traps: Tools for spectroscopy and dynamics of cold molecular ions", *Journal of Physics B: Atomic, Molecular and Optical Physics*, vol. 42, no. 15, pp. 1–12, 2009. DOI: 10.1088/0953-4075/42/15/154001.

[3] J. A. Stearns, C. Seaiby, O. V. Boyarkin, and T. R. Rizzo, "Spectroscopy and conformational preferences of gas-phase helices", *Physical Chemistry Chemical Physics*, vol. 11, pp. 125–132, 2009. DOI: 10.1039/B814143F.

[4] J. D. Jackson, *Classical electrodynamics*, 1st ed. Wiley & Sons, Inc., 1962.

[5] D. Gerlich, "Inhomogeneous electrical radio frequency fields: A versatile tool for the study of processes with slow ions", in *State–Selected and State-to-State Ion-Molecule Reaction Dynamics*, C.Y.Ng and M. Baer, Eds., J. Wiley & Sons, 1992. DOI: 10.1002/9780470141397.ch1.

[6] D. Gerlich, "The study of cold collisions using ion guides and traps", in *Low Temperatures and Cold Molecules*, I. W. M. Smith, Ed. Imperial College Press, 2008.

[7] D. R. Lide, "Ionization potentials of atoms and atomic ions", in *Handbook of Chemistry and Physics*, D. R. Lide, Ed., 73rd ed. CRC Press. Boca Raton, Florida, 1992, pp. 10–211.

[8] J. T. Stewart, B. E. Brumfield, B. M. Gibson, and B. J. McCall, "Inefficient vibrational cooling of $C_{60}$ in a supersonic expansion", *ISRN Physical Chemistry*, vol. 2013, pp. 1–10, 2013. DOI: 10.1155/2013/675138.

[9] E. E. Nikitin and R. N. Zare, "Correlation diagrams for Hund's coupling cases in diatomic molecules with high rotational angular momentum", *Molecular Physics*, vol. 82, no. 1, pp. 85–100, 1994. DOI: 10.1080/00268979400100074.

[10] J. M. Hollas, *High Resolution Spectroscopy*, 2nd ed. John Wiley & Son Ltd, 1998.

[11] R. Schinke, *Photodissociation dynamics: Spectroscopy and fragmentation of small polyatomic molecules*. Cambridge University Press, 1995.

[12] M. Foltin, M. Lezius, P. Scheier, and T. D. Märk, "On the unimolecular fragmentation of $C_{60}^+$ fullerene ions: The comparison of measured and calculated breakdown patterns", *The Journal of Chemical Physics*, vol. 98, no. 12, pp. 9624–9634, 1993. DOI: 10.1063/1.464393.

[13] J. Roithová, A. Gray, E. Andris, J. Jašík, and D. Gerlich, "Helium tagging infrared photodissociation spectroscopy of reactive ions", *Accounts of Chemical Research*, vol. 49, pp. 223–230, 2016. DOI: 10.1021/acs.accounts.5b00489.

[14] P. J. Kelleher, C. J. Johnson, J. A. Fournier, and M. A. Johnson, "Persistence of dual free internal rotation in the helium "tagged" $NH_4^+(H_2O)\cdot He_{n=0-3}$ ion-molecule complexes: Expanding the case for quantum delocalization in he tagging", *The Journal of Physical Chemistry A*, vol. 119, no. 18, pp. 4170–4176, 2015. DOI: 10.1021/acs.jpca.5b03114.

[15] M. Brümmer, C. Kaposta, G. Santambrogio, and K. R. Asmis, "Formation and photodepletion of cluster ion–messenger atom complexes in a cold ion trap: Infrared spectroscopy of $VO^+$ , $VO_2^+$ , and $VO_3^+$", *The Journal of Chemical Physics*, vol. 119, no. 24, pp. 12 700–12 703, 2003. DOI: 10.1063/1.1634254.

[16] T. Pino, N. Boudin, and P. Bréchignac, "Electronic absorption spectrum of cold naphthalene cation in the gas phase by photodissociation of its van der Waals complexes", *Journal of Chemical Physics*, vol. 111, no. 16, pp. 7337–7347, 1999. DOI: 10.1063/1.480105.

[17] E. J. Bieske, A. M. Soliva, A. Friedmann, and J. P. Maier, "Electronic spectra of $N_2^+$-$(He)_n$ ($n$=1, 2, 3)", *The Journal of Chemical Physics*, vol. 96, no. 28, pp. 28–34, 1992. DOI: 10.1063/1.462517.

[18] M. F. Mesleh, J. M. Hunter, A. A. Shvartsburg, G. C. Schatz, and M. F. Jarrold, "Structural information from ion mobility measurements: Effects of the long-range potential", *Journal of Physical Chemistry*, vol. 100, no. 40, pp. 16 082–16 086, 1996. DOI: 10.1021/jp961623v.

[19] W. Demtröder, *Laser spectroscopy*, 3rd ed. Springer, 2003.

# 3

*I suppose it is tempting, if the only tool you have is a hammer, to treat everything as if it were a nail.*

■ Abraham H. Maslow

# Experimental

The approach used in this thesis is based on trapped ions at cryogenic temperatures combined with mass spectrometry. The basic setup is shown in Figure 3.1. Charged molecules are typically produced by evaporation in the source and subsequently guided into a quadrupole mass filter by electrostatic elements. A quadrupole bender turns the ions into a trap, where they are held for a well defined time and probed by laser radiation. The experiment is developed such, that an investigation of the confined species produce fragments which can be analyzed by a mass spectrometer coupled to a Daly detector. For proper operation of all devices, a decent vacuum is required in order to prevent arcing due to high DC and AC voltages applied and to avoid uncontrolled chemical reactions with residual gas. Each chamber has a turbomolecular pump, providing low pressures of $\sim 10^{-9}$ mbar. Furthermore, differential walls between chambers minimize gas flow.

Throughout the thesis the experimental setup has been under development. A modular arrangement made it possible to change individual parts in short times. The first experiments have been carried out in a linear configuration. An improvement has been achieved by implementing a quadrupole bender. This ensured less contamination of a neutral effusive beam and easier alignment of the laser through the trap.

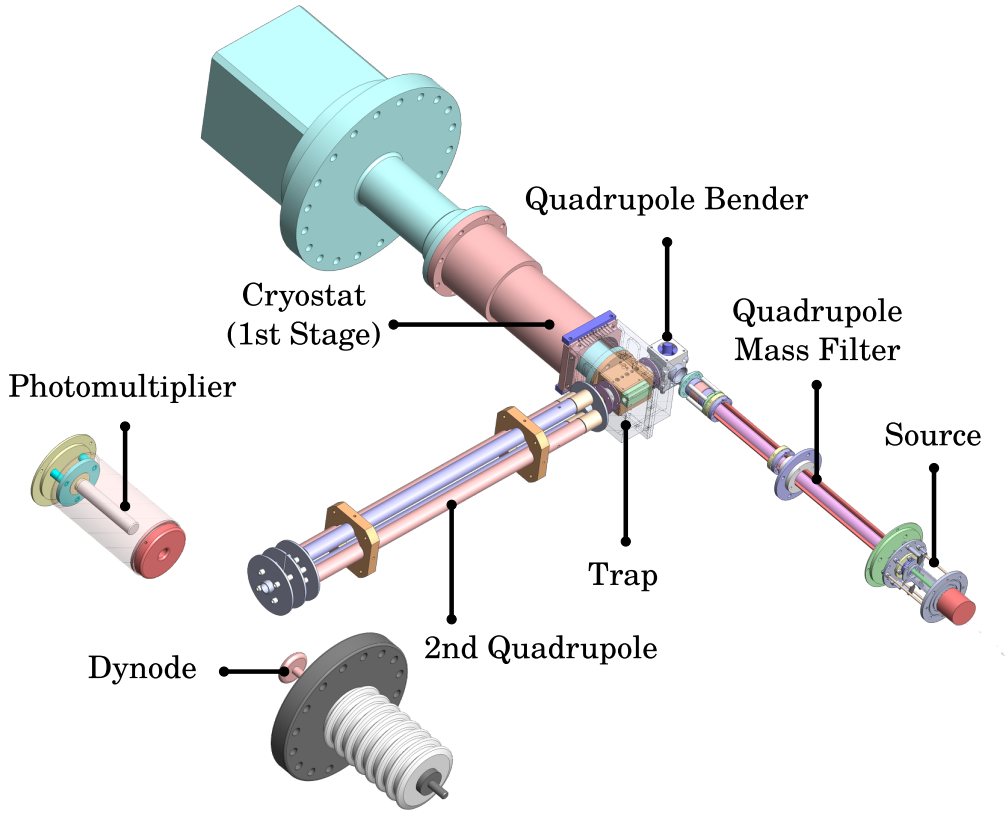


Figure 3.1: Overview of the basic elements of the ion trapping apparatus.

## 3.1 Electron Impact Source

Cationic molecules or atoms are produced in the electron impact source shown in Figure 3.2. Neutral vapor gas is either leaked in to the chamber directly or created by heating a solid sample in an oven. The tubular oven is made of oxygen-free high thermal conductivity copper (OHFC) and mounted between plates via four small sticks ($\varnothing = 0.5\,\mathrm{mm}$) on each side to avoid heat losses. An attached cartridge heater (Watlow, Firerod 50 W) provides temperatures of $\sim 700\,^{\circ}\mathrm{C}$, which can be monitored with a thermocouple.

The central element is a rhenium filament ($\varnothing = 0.3\,\mathrm{mm}$) which is spot-welded on electrically insulated holders. This transition metal has been established as the best choice for the samples that were used, especially because of its long term stability. Lifetimes of more than 6 months could be achieved, depending on the degradation due to the investigated species. The emission current of the filament is set to $\sim 300\,\mu\mathrm{A}$ at an applied power of $P = 30$-$40\,\mathrm{W}$. A cylindrical metal grid is placed inside the filament and held at a positive voltage with respect to reference, which defines the kinetic energy of the electrons.

Three electrodes creating an einzel lens are utilized to extract the cations from the ionization region and inject them into the first quadrupole. The whole source is fully enclosed to maintain a high pressure of neutral sample and thus efficient ionization. Evacuation is only possible through the electrodes and a small gate with a diameter of 8 mm. The source already predefines the kinetic energy distribution of the ions. Therefore, the settings have to be carefully chosen to obtain optimal conditions for ion guiding, mass selection, and trapping.

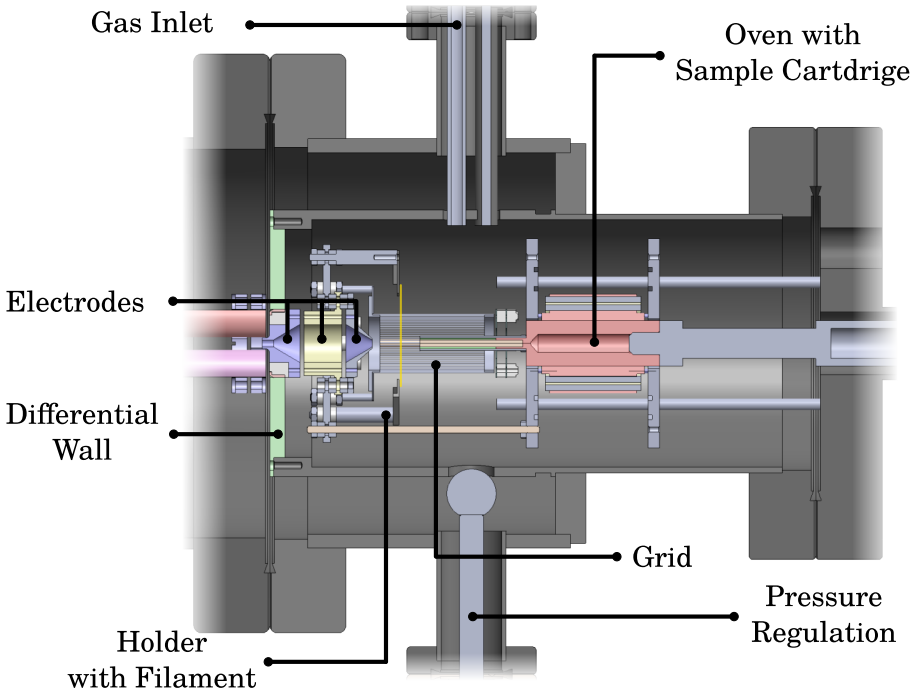


Figure 3.2: Electron impact source. Basic elements are: gas inlet, oven, filament, grid and extraction electrodes.

## 3.2 Quadrupole Mass Filter

The apparatus uses two quadrupoles for mass selection, the principles have been discussed in detail in section 2.1. The first one is a home-build mass filter to guide ions from the source to the quadrupole bender and is typically operated in RF-mode only. A pole bias and DC voltage for preselection of ions can be applied in a range of ±15 V. A DC splitting of the two phases larger than this caused instabilities in the ion beam. The rods ($\varnothing = 10\,\mathrm{mm}$) of the quadrupole have a special shape on the outside ("half moon") and provide a compact design for differential pumping. On both ends, a set of electrodes is mounted. The applied potentials of typically ±5 V on the electrodes are crucial as they determine the spatial distribution of the ion beam, which influences the transmission properties. To drive the mass filter, a push-pull RF oscillator based on the design by Dieter Gerlich was used [1].

The second quadrupole is necessary for mass selection. It is a commercial system (Extrel GP-203D) with a rod diameter of $\varnothing = 9.5\,\mathrm{mm}$. The RF generator is also a commercial device (Extranuclear) operated with an external crystal at 1.2 MHz. This setup allows a mass range $m/z < 2000$ at transmission ratios of max 25 % for a 10% valley. For better focusing properties of the ion beam, the quadrupole has a pre- and post-filter system. The applied voltages on the extraction electrodes of the quadrupole are usually higher with ±200 V. From this point, the mass selected ions are accelerated to the detector.

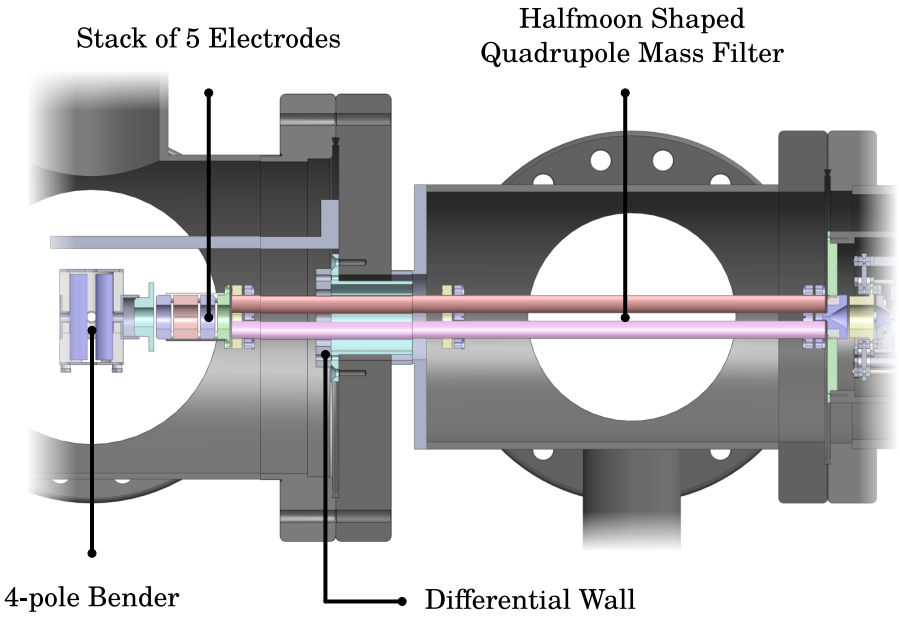


Figure 3.3: Quadrupole mass filter.

## 3.3 Multipole Radio Frequency Ion Traps

For confining positively charged particles, two traps have been used: a 4-pole and a 22-pole trap. The trap is placed in the L-shaped configuration between the bender and the mass spectrometer. A polished aluminum-shield (Figure 3.1) is mounted onto the first stage of a closed cycle He-refrigerator (Sumitomo RDK-250D 4K) operated by a CKW-21A Compressor. This ensures a maximum of 40-50 K of black body radiation emitted to the trap which is mounted to the second stage. A minimal wall temperature of 3.4 K can be reached without any gas load. This is measured by a silicon diode (Lakeshore DT-670) on top of the cover, where the warmest spot is assumed. To control the trap temperature a cartridge heater (Lakeshore HTR-50) can be attached. The inner electrodes are pulsed for ion injection and extraction. Both are in the vicinity of RF elements and to reduce the induced noise, RC-filters close to the feed through connectors were implemented. This improved trapping efficiency drastically.

The traps have individual characteristics as can be seen from their potential fields in Figure 3.4. Steep walls of the harmonic potential for the quadrupole and large field free regions in the 22-pole trap offer different trapping volumes for specific applications. The amount of stored ions in both traps is limited by space charge effects. Even below the threshold of strong Coulomb repulsion, it has been shown that the average translational temperature of molecules decreases in higher order multipoles [2].

### 3.3.1 22-Pole Trap

In Figure 3.6 (a) the 22-pole trap is shown. It consists of $2 \times 11$ stainless steel rods arranged equally spaced onto two copper plates with an inscribed radius of 1 mm. The trap is shielded by a Π-shaped block in order to cover it from the 40-50 K black body radiation emitted from an Al-shield. Electrical insulation from the RF side plates is maintained by ceramic rods. The trap together with the Π-cover are mounted via a base plate onto the cryostat.

For the two end-cap electrodes ($\varnothing_{\text{inner}} = 6.6\,\text{mm}$) on either side, several designs have been used over the years. Initially, large ring shaped stainless steel electrodes as shown in Figure 3.6 (a) were utilized. To minimize the surface area for absorption of black body radiation they have been replaced by small metal tubes encased inside a ceramic cylinder. The drawback of the latter system is to ensure a parallel

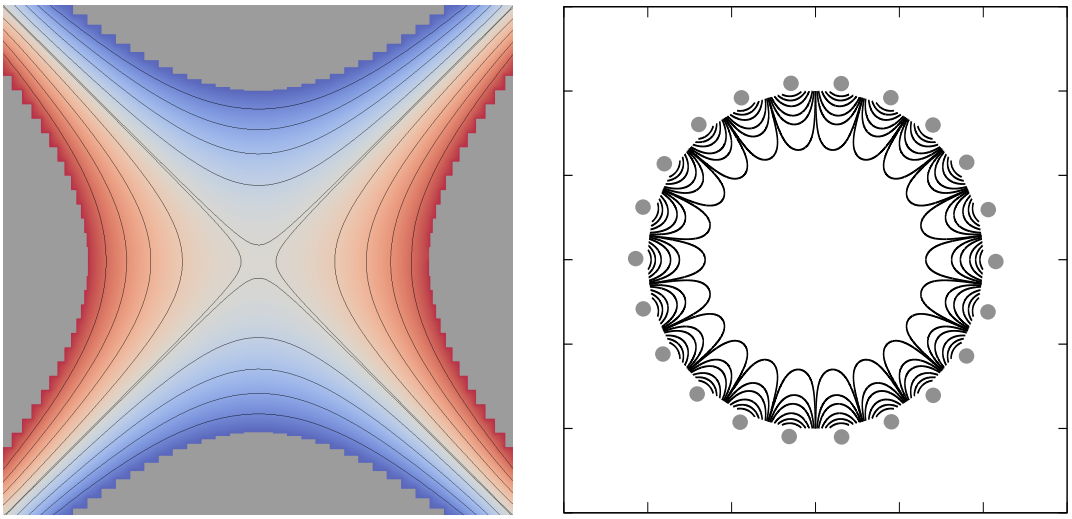

(a) (b)

Figure 3.4: Contour plot with isolines for 4-pole (a) and 22-pole trap (b). The quadrupole potential is obtained from calculations using finite elements, the higher order multipole was calculated from the analytical solution. The isolines in both figures represent the same $V(r)/V_0$ value indicating the large field-free region for the 22-pole.

alignment to the trap axis, as they are only pushed into ceramic spacers which are mounted to the RF side plates. The side plates themselves are electrically insulated to the base plate by sapphire plates to allow proper thermal conductivity. A RF-generator similar to the design used for the mass filter has been utilized and operated at frequency of $f = 5\,\mathrm{MHz}$. For certain experiments it was necessary to avoid accumulation of ions over several trapping cycles. Therefore, it was possible to switch off the RF using a TTL-pulse to empty the trap after extraction.

### 3.3.2 4-Pole Trap

The quadrupole trap shown in Figure 3.6 (b) has a housing entirely manufactured in one piece (OHFC) for maximum thermal conductance. Hyperbolic shaped rods have been approximated by a step function

$$y_i = \sqrt{\left(x_{i-1} + \Delta x + \frac{r_0}{2}\right)^2 + r_0^2}, \tag{3.1}$$

with an inscribed radius of $r_0 = 5\,\mathrm{mm}$ and a step size $\Delta x = 0.5\,\mathrm{mm}$. Although the latter has been chosen rather large, the calculated potential shown in Figure 3.4 resembles the harmonic one. Only very close to the rods it becomes anharmonic. However, these are regions where even in case of an ideal quadrupole potential

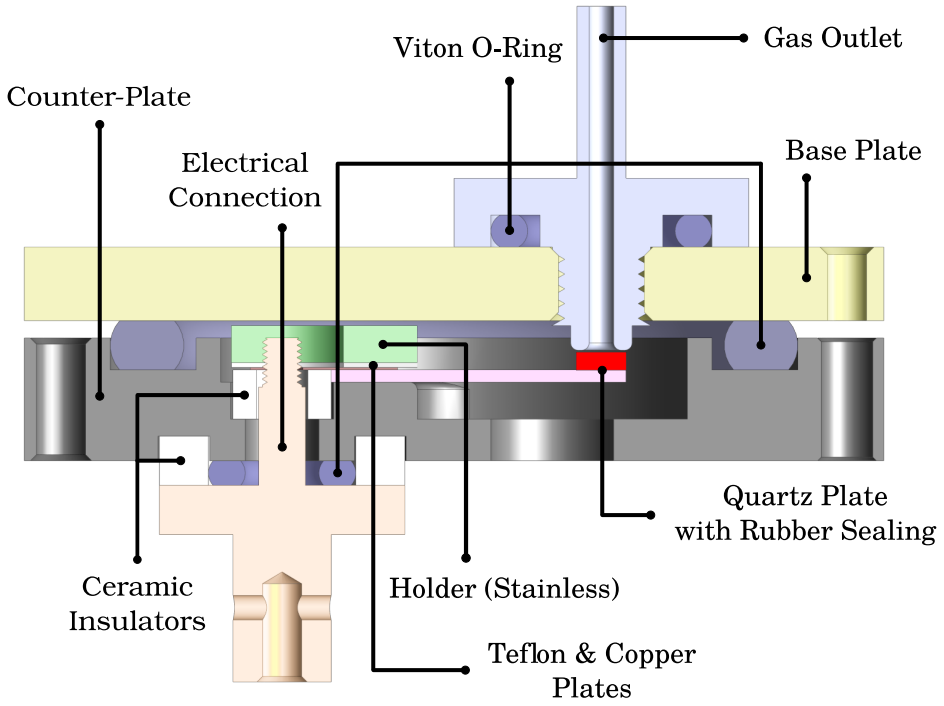


Figure 3.5: Schematic drawing of the piezo valve.

unstable trajectories are expected due to RF-heating. The end-cap electrodes are made from copper tubes press fit into ceramic holders which themselves are press fit into copper holders. One pair of electrodes is mounted directly onto the trap housing, while the second one is mounted to the Al-shield. Special care has to be taken for the high purity copper used to avoid fast degeneration of the material due to oxidation. The trap was driven by a RF-generator with $f = 780\,\mathrm{kHz}$ as the geometry requires lower frequencies.

### 3.3.3 Piezo Valve

Directly attached to the trap is a piezo valve (Figure 3.5) based on the construction of Dieter Gerlich [3]. It offers a compact design and can be operated in a pulsed (TTL) or resonant mode. The basic element is a bimorph piezoelectric plate which can be actuated using pulse amplitudes of 100-300 V. It produces $< 20\,\mu\mathrm{s}$ short and intense pulsed atomic beams allowing flexible application possibilities. For complex formation and buffer gas cooling, the piezo valve was usually gated for a well-defined time at a typical resonance frequency of 3.4 kHz.

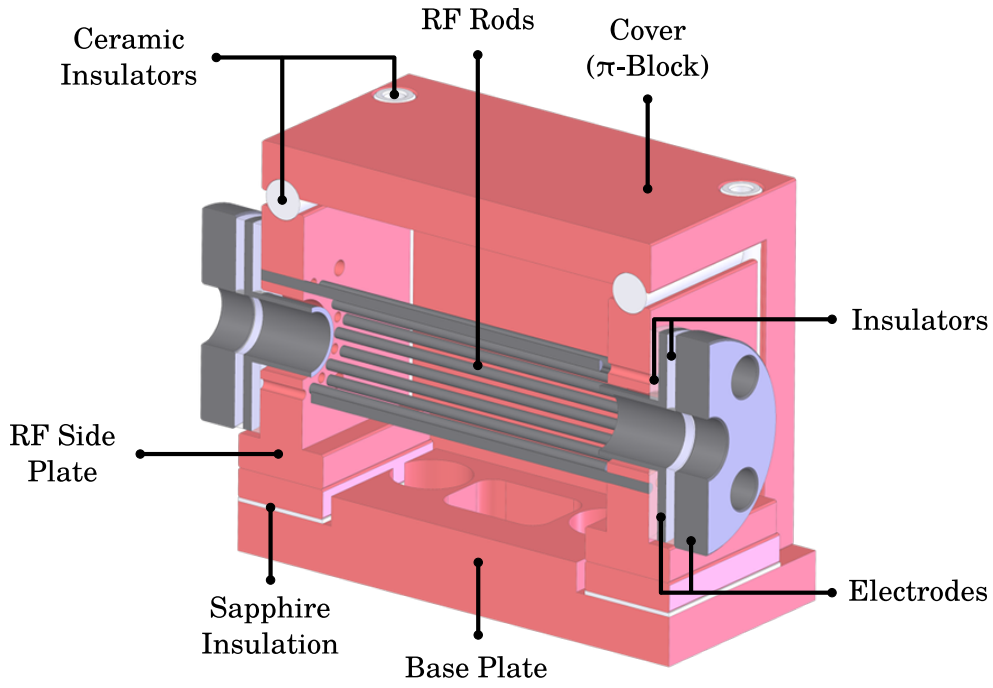


(a)

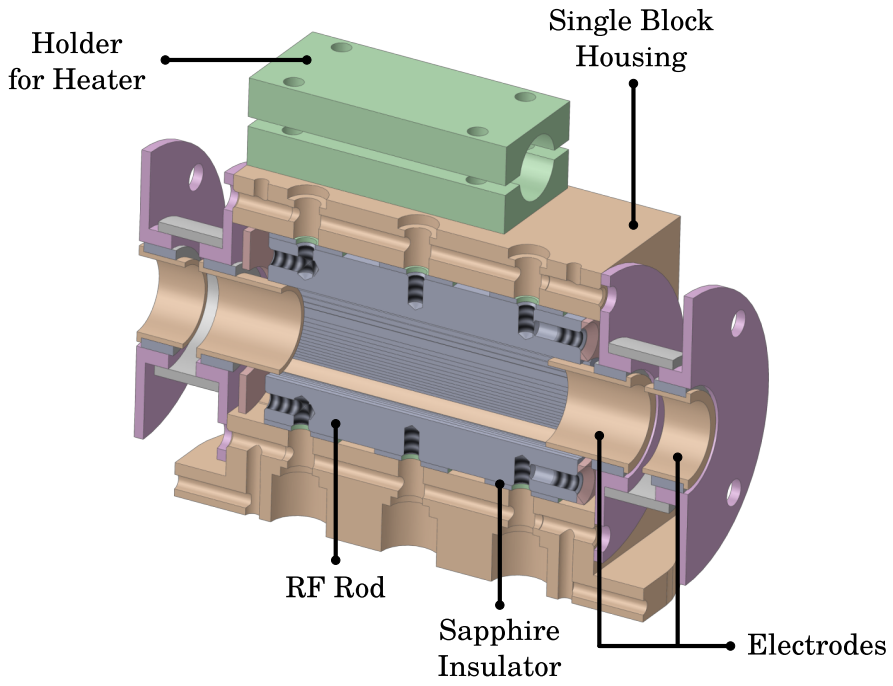


(b)

Figure 3.6: Detailed schematic of the 22-pole (a) and 4-pole (b) indicating the basic elements.

## 3.4 Ion Detection

A Daly type detector (Figure 3.7) is used to count ions [4]. It is composed of a highly polished conversion dynode with $-30\,\mathrm{kV}$ applied. The mass selected ions are therefore accelerated toward the dynode and upon impact secondary electrons are emitted. The same high voltage accelerates the electrons onto a scintillator (BC400, Saint-Gobain Crystals) where they are converted into photons. This is a consequence of internal excitation of the polymer, resulting in radiative relaxation with decay times below 4 ns. The photons are detected by a photomultiplier (PMT, Hamamatsu R647p) with a gain factor of $1 \times 10^6$. The PMT is mounted outside the vacuum chamber if fast replacement is necessary and an easier implementation of (non vacuum suitable) electronics for signal processing. Dynode and scintillator are housed inside of a grounded cylinder to prevent interaction between the RF of the quadrupole and the high voltages applied. The cylinder has a hole to let laser radiation pass to the view port at the end of the chamber.

The signal provided from a PMT can be measured directly with an ammeter (Keithley 6485) which is sensitive down to picoampere. Another possibility is to convert the signal into short pulses. A 300 MHz discriminator (Phillips Scientific Model 6904) ensures a constant pulse signal which is read by frequency counter (Picotest U6220A) allowing an estimation for the number of ions reaching the detector. Both methods work simultaneously. The counter receives a gate from a pulse generator (Berkeley Nucleonics 565) which has been used as the reference clock. In later experiments this device has been synchronized to the cycle of the cryostat. Furthermore, the pulse generator provided the trigger signal for the extraction electrodes of the trap, the piezo valve, pulsed lasers or in case of continuous-wave (cw) laser, the shutter.

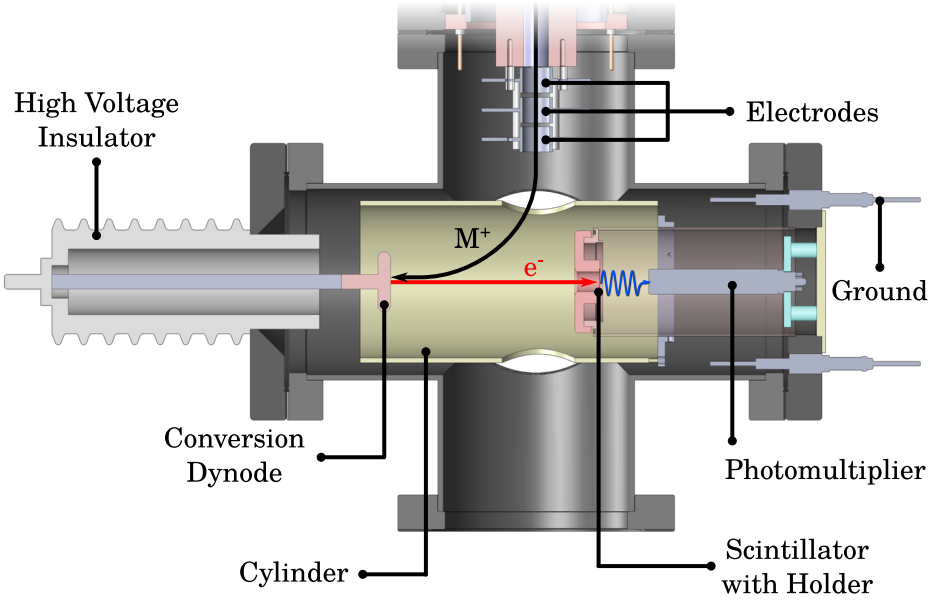


Figure 3.7: Schematic of the chamber with the Daly type detector and illustration of the Ion detection scheme. Ions are extracted from the quadrupole mass spectrometer, accelerated to the dynode and converted into electrons. These are moving toward a scintillator which emits photons which are detected by a PMT.

## 3.5 Laser Systems

Several different laser systems for the experiments were employed and are briefly described in the following. An estimation of the laser frequency was obtained from a wavemeter (High Finesse WS6-200) allowing an absolute accuracy of 200 MHz in the typical ranges used. As a calibration source the HeNe emission at 633 nm was utilized. For vacuum to air wavelength conversion the formula from Ref. [5] for the refractive index was used.

**External Cavity Diode Laser:** This type of laser has been employed for NIR scans in the range of 930 - 980 nm. A narrow linewidth (<10 MHz) was achieved by a Littrow configuration [6]. The setup includes an one-side anti-reflection coated laser diode (Sacher) together with a collimating lens followed by a diffraction grating. The first order diffracted beam acts as an optical feedback and is sent back to the laser diode. For scanning ranges below 0.1 $cm^{-1}$ the diode current has been changed. Tuning ranges of 1 $cm^{-1}$and up to $\sim$ 20 $cm^{-1}$ could be achieved by rotating the diffraction grating either via a piezo element or a stepper motor, respectively. A moving of the grating causes a horizontal offset in the beam path. For compensation a rotating mirror controlled by another stepper motor was used. A beam splitter guides a fraction of the laser beam onto a camera for optical feedback of the beam position.

**Coherent 899 Ti:Sapphire Ring Dye Laser:** This second cw system uses a Ti:Sapphire solid state crystal as the gain medium. The setup allowed a narrow linewidth of 500 kHz with scanning ranges of 30 GHz. Removing of the internal etalon allowed also long range scans at a higher bandwidths of 3-5 GHz. Depending on the optical setup, a wavelength range between 750-930 nm could be covered at output powers between 50-750 mW.

**EKSPLA OPO:** The EKSPLA optical parametric oscillator has been mainly used for survey scans in the region between 240-1100 nm. It provides pulse energies between 10-20 mJ with a bandwidth of about 5 $cm^{-1}$ at a typical pulse length of 5 ns.

**Sirah Dye Laser:** The Nd:YAG pumped dye laser was employed, whenever measurement below 750 nm have been necessary. It offered pulses with bandwidths of $< 0.1$ $cm^{-1}$. The scanning range and output power was dependent on the conversion efficiency of the dye.

## 3.6 Operating procedures

Several experimental aspects that were essential for optimal ion trapping and complex formation are presented with examples in the following sections. Furthermore, constraints of the apparatus, which have to be considered for spectroscopic studies are discussed.

### 3.6.1 Estimation of Number Densities

A direct estimation of absolutes pressures from the ion gauge mounted to the chamber is not possible, because pressures inside and outside the trap can differ by two orders of magnitude. Therefore, a capacitance manometer (CMR-365) is used for absolute values inside the trap. Before the number density can be derived, the effect of thermal transpiration has to be considered. Manometer and trap are connected through a tube of length $\sim 20\,\mathrm{cm}$ exhibiting different temperatures. This introduces a gas flow, leading to false pressure indication. The critical parameter of the effect is the Knudsen number. In the given situation molecular flow conditions can be assumed leading to a relation for the pressure at the manometer

$$p_1 = p_2 \cdot \sqrt{\frac{T_1}{T_2}}, \tag{3.2}$$

where $p_1$ and $p_2$ are the pressure at $T_1$ and $T_2$, respectively. The relation is only an approximation for small tubes derived from kinetic gas theory. A variety of empirical studies provide more precise estimates and the one used here is based on the Takaishi-Sensui equation with unified parameters for helium [7]:

$$\frac{p_\mathrm{M}}{p_\mathrm{trap}} = 1 + \frac{\sqrt{T_\mathrm{trap}/T_\mathrm{M}} - 1}{6.11 \cdot (X/X_0)^2 + 4.26 \cdot X/X_0 + 0.52 \cdot \sqrt{X/X_0} + 1} \tag{3.3}$$

and

$$X = \frac{2dp_\mathrm{M}}{T_\mathrm{M} + T_\mathrm{trap}}. \tag{3.4}$$

The factor $X_0 = 1\,\mathrm{mm\,Pa/K}$ accounts for the correction of the units, $d = 3\,\mathrm{mm}$ is the diameter of the connecting pipe and $Y_\mathrm{M}$ conditions of the manometer. Knowing the correction of the pressure, a number density can be determined from the ratio of the ideal gas laws at normal conditions and in the trap. At $T_\mathrm{trap} = 4\,\mathrm{K}$ and $p_\mathrm{M} = 5 \times 10^{-3}\,\mathrm{mbar}$ a pressure inside the trap of $p_\mathrm{trap} = 1 \times 10^{-3}\,\mathrm{mbar}$ is given and

thus a number density of

$$n_{\mathrm{trap}} = \frac{V_{\mathrm{m}}}{N_{\mathrm{A}}} \cdot \frac{p_{\mathrm{trap}} \cdot T_0}{p_0 \cdot T_{\mathrm{trap}}} \tag{3.5}$$

$$= 2.65 \times 10^{19}\,\mathrm{cm}^{-3} \cdot \frac{1 \times 10^{-3}\,\mathrm{mbar} \cdot 273\,\mathrm{K}}{4\,\mathrm{K} \cdot 1000\,\mathrm{mbar}} \tag{3.6}$$

$$= 1.8 \times 10^{15}\,\mathrm{cm}^{-3} \tag{3.7}$$

is calculated. The factors $V_{\mathrm{m}}$ and $N_{\mathrm{A}}$ are the standard molar volume and Avogadro's number. The resulting number density is a typical value obtained in the experiments.

### 3.6.2 Ion Trapping and Complex Formation

The scheme for ion trapping, including a typical timing sequence, is illustrated in Figure 3.8. Depending on the formation efficiency in the source, charged molecules are accumulated for 10 to 300 ms by keeping the entrance electrode below their kinetic energy. During the same time the exit electrode is held above this energy, while simultaneously buffer gas is introduced. The latter creates a cold bath for the ions to dissipate their translational and also internal energy. After one axial round trip in the trap, the ion's kinetic energy has to be lower than the potential applied to the entrance electrode. If a sufficient amount of ions is captured, the entrance electrode potential is raised to avoid space charge effects and collisions with hot ions. Several collisions with buffer gas produces cold ions which are subsequently probed by laser radiation. Finally, they are released by lowering the exit electrode potential and guided into the mass spectrometer.

Efficient trapping and cooling of ions are crucial for the formation of weakly bound complexes. The potentials applied on the end-cap electrodes have a large impact on the trapped particles. The radial component of the potential pushes the ions toward the RF electrodes. Heating effects due to strong coupling between the fast oscillating field and the ion motion have been shown in experimental and theoretical studies [2, 8]. For example, crystal properties observed for laser cooled $Ca^+$ in a linear octupole trap vanishes due to excessive increase of the end-cap electrodes [9]. The magnitude of the electrostatic potentials is determined by the initial kinetic energy of the ions. An estimate of the ion's energy distribution can be obtained by a retarding field analysis. Figure 3.9 shows an example of such a measurement for an $Ar^+$ beam. The dependency $N(Ar^+)$ versus the retarding field voltage $V$ allows the determination of the mean energy and a corresponding spread of the charged

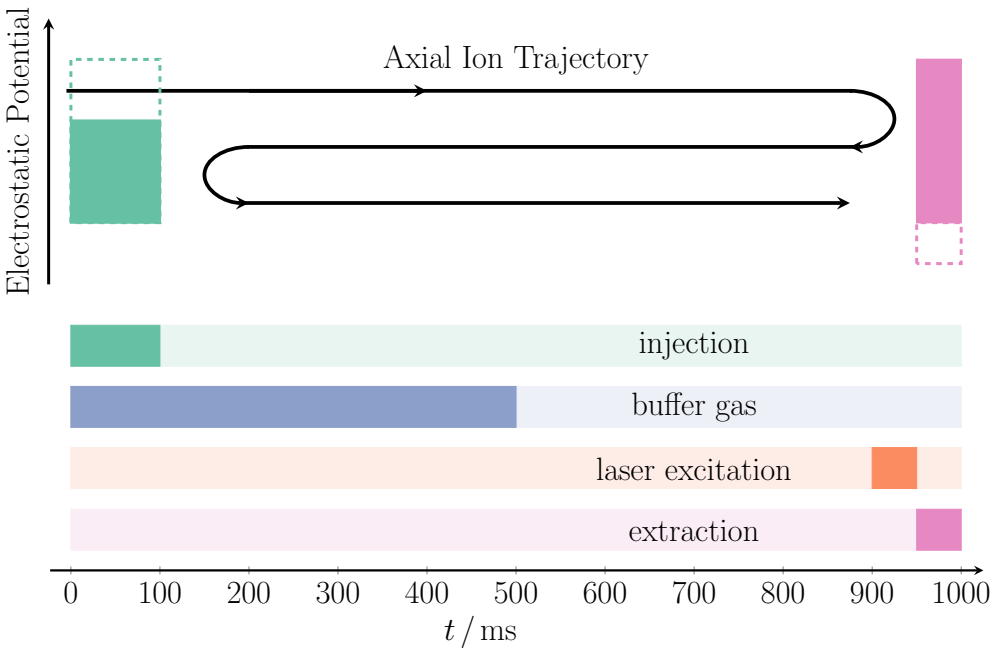


Figure 3.8: Typical trapping sequence at a repetition rate of 1 Hz: The trap is filled for 100 ms (■) with some thousands of ions by lowering the entrance electrode potential. During the first 500 ms they interact with helium buffer gas (■) in order to reduce their kinetic and internal energy. For photodissociation spectroscopy, the ions are irradiated (■) after evacuating the trap from the buffer gas. Ions are released to the mass spectrometer by lowering the exit electrode (■). The timings can be varied according to the needs of the experiment, indicated by the dimmed colors.

particles. The values can be extracted from a Gaussian fit of the first derivative of the recorded retarding curve. In the presented example $E_{\mathrm{mean}}(\mathrm{Ar}^+) = 240\,\mathrm{meV}$ and $\Delta E(\mathrm{Ar}^+) = 540\,\mathrm{meV}$ were obtained.

The formation of complexes in a three body collision is represented by the ternary association rate coefficient $k_3$ and its competing process collisional induced dissociation (equation 2.46). Different types of neutral collision partners have been used in the past. As already discussed, the ion-to-neutral mass ratio is an important factor for the internal energy of the ion, consequently helium offers the best properties [2]. In Figure 3.10 the time dependent evolution of complex growth of $\mathrm{NCCN}^+$–He is shown. With a helium density of $8 \times 10^{14}\,\mathrm{cm}^{-3}$ a ternary rate coefficient $k_3 = 5 \times 10^{-31}\,\mathrm{cm}^6\mathrm{s}^{-1}$ at 4 K was obtained. A stationary equilibrium between complex formation and dissociation is reached after ∼100 ms. The uncertainty for the rate coefficient is rather large as the pressure and temperature reading varied

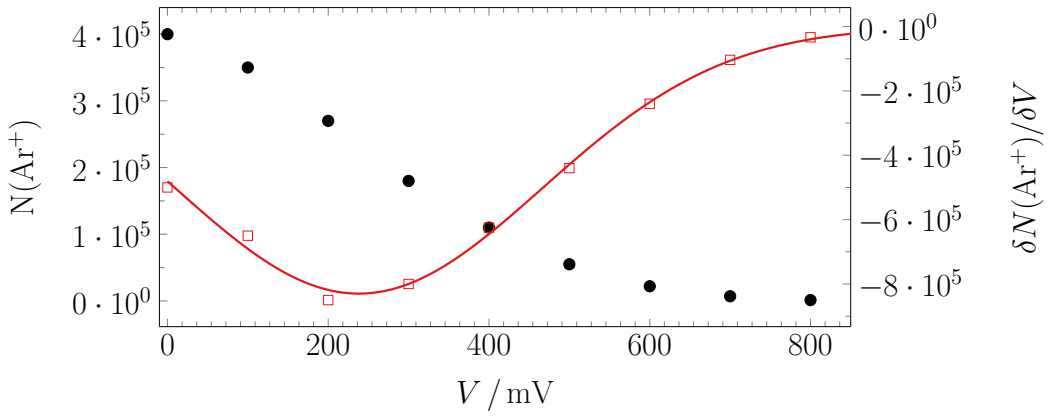


Figure 3.9: Retarding field analysis of an $Ar^+$ beam by changing the field axis of the 22-pole trap. The number of ions (●) is shown as a function of the applied voltage. The first derivative (□) for the experimental data is fit with a Gaussian function (–) providing information of the energy distribution.

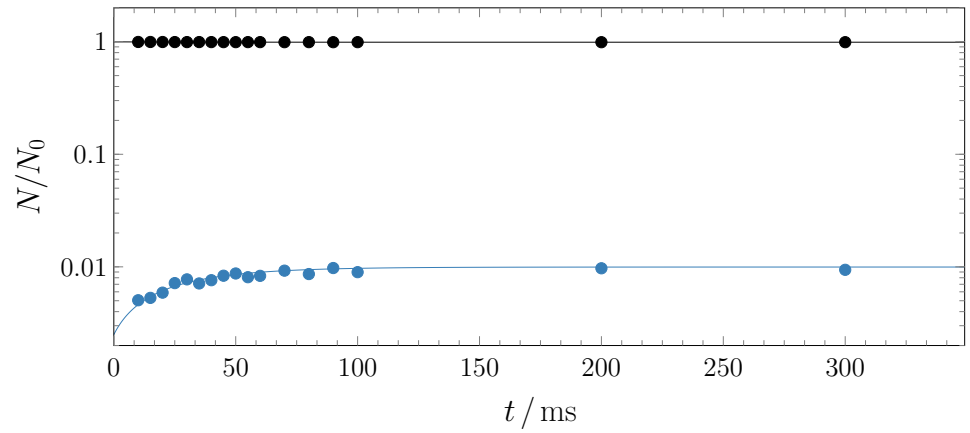


Figure 3.10: $NCCN^+$–He (●) growth as a function of the storage time. Only $\sim 1\,\%$ of $NCCN^+$ (●) can be converted into complexes. A stationary equilibrium between formation and dissociation is reached after ∼100 ms. The solid lines indicate the numerical simulation of the process.

significantly with the cold-head cycle. At temperatures below 4.5 K helium condenses on the walls leading to the observed effect. The reversed reaction rate is estimated from simulations to $k_{\mathrm{CID}} = 4 \times 10^{-14}\,\mathrm{cm^3 s^{-1}}$.

### 3.6.3 Absorption Cross-Sections

The cross-section can be experimentally estimated by measuring the attenuation of the complexes as a function of the laser fluence at a fixed wavelength (equation (2.50)). However, one has to account for the different properties of the traps. In the case of the 22-pole trap, the ion cloud is larger than the laser beam due to geometrical constraints of the electrodes. The ions are then exposed to a fluence

$$\Phi = \frac{P\Delta t}{\pi r_{\mathrm{c}}}, \tag{3.8}$$

where $P$ is the measured power of the cw laser beam, $\Delta t$ the irradiation time and $r_{\mathrm{c}}$ the radius of the ion cloud. Using $r_{\mathrm{c}}$ is valid under the assumption that all ions interact with the radiation field.

For the 4-pole trap the ion cloud is expected to be smaller than the spatial width of the laser beam. The radial intensity distribution of a Gaussian beam profile is given by [10]

$$I(r) = \frac{2P}{\pi\omega^2} \cdot \exp\left(-\frac{2r^2}{\omega^2}\right), \tag{3.9}$$

with a beam waist $\omega$. The fraction that overlaps with the ion cloud is obtained by the integral

$$\frac{P(r_{\mathrm{c}})}{P} = \frac{2}{\pi\omega^2}\int_0^{r_{\mathrm{c}}} 2\pi r \exp\left(-\frac{2r^2}{\omega^2}\right) \mathrm{d}r \tag{3.10}$$

$$= 1 - \exp\left(-\frac{2r_{\mathrm{c}}^2}{\omega^2}\right), \tag{3.11}$$

which leads to

$$\Phi = \frac{P\Delta t}{\pi r_{\mathrm{c}}^2}\left(1 - \exp\left(-\frac{2r_{\mathrm{c}}^2}{\omega^2}\right)\right). \tag{3.12}$$

An estimation of the characteristic fluence with a Gaussian beam profile requires a parallel overlap in axial direction of ion cloud and laser beam. This can be challenging and small deviations will lead to large errors. Therefore, the profile was modified to a Flat-Top (FT) shape providing a nearly constant power density (Figure 3.11). This was achieved by expanding the beam over a distance $L = 7\,\mathrm{m}$ and using the bender rods/electrodes as an aperture. In the near field a Fressnel-like

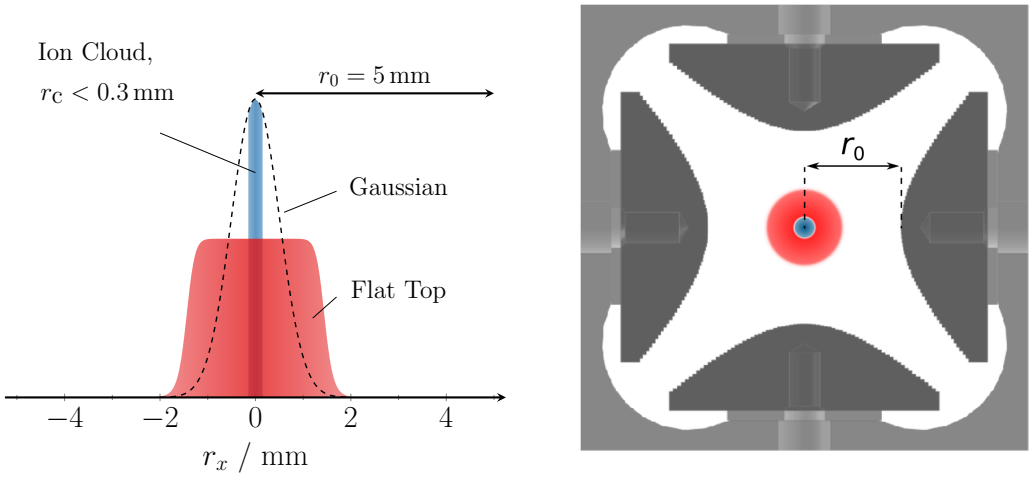


(a) (b)

Figure 3.11: (a) Illustration of a parallel overlap of a Gaussian and a Flat-Top beam profile with an ion cloud in a 4-pole trap. The power density for a Flat-Top is nearly constant over the whole cross-section. In contrast the Gaussian profile will lead to different results for small deviations from a coaxial alignment. Dimensions are chosen, as used in the experiment. (b) Radial view on the 4-pole trap with the overlapped Flat-Top profile with the ion cloud.

diffraction pattern can be observed which stays almost constant over the length of the trap and collapses back to a Gaussian profile in the far-field. In Figure 3.12 two such profiles are presented. The right Figure (b) represents the profile measured directly at the location of the trap. The D-shaped profile is a result of the bender rods. To the left (a) the pattern created with an iris at the assumed position of the trap outside the machine is shown. In order to estimate the total power of the laser beam irradiating the ion cloud, this iris has been used to mimic the bender electrode. Inspection of the cuts through the profile reveals an interference patter instead of a flat curve. However the integrated power density for an ion-cloud with radii of $r_c = 0.18\,\mathrm{mm}$ and $r_c = 0.21\,\mathrm{mm}$ yields deviations of less than 10 %, assuming the overlap of laser beam and ion-cloud within an offset of at most $r = 0.5\,\mathrm{mm}$ (Figure 3.13). The radii $r_c$ correspond to translational temperatures of $T = 100\,\mathrm{K}$ and $T = 75\,\mathrm{K}$ and a RF-amplitude of $V = 150\,\mathrm{V}$.

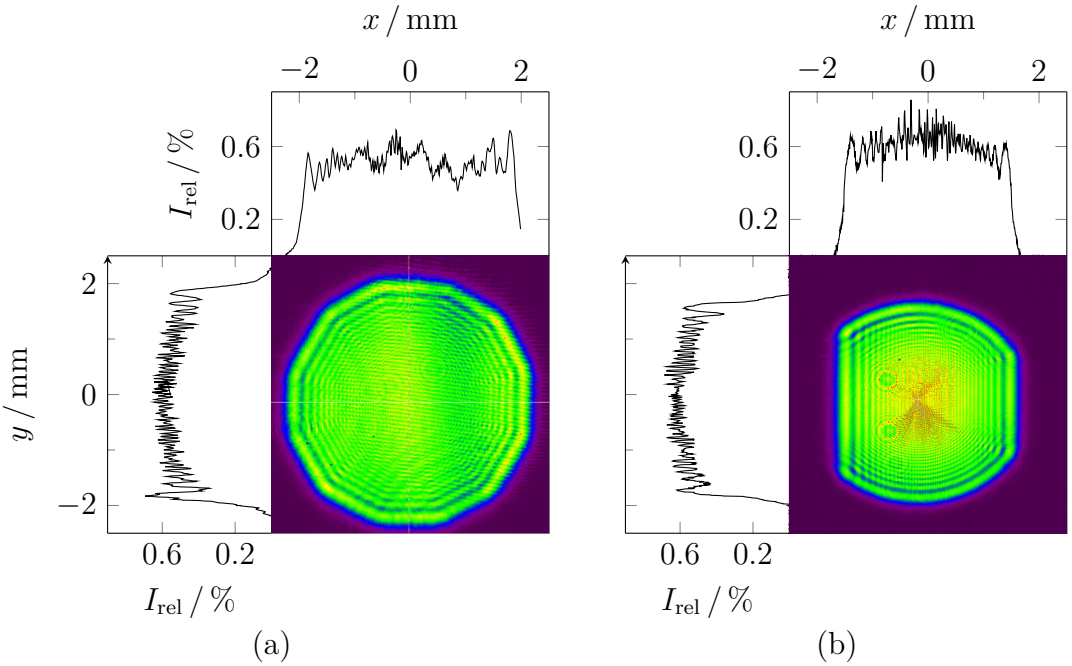


Figure 3.12: Two-dimensional map of the Flat-Top intensity distribution with vertical and horizontal cuts through the center of the profile at $\tilde{\nu} = 10438\,\mathrm{cm}^{-1}$. (a) Profile created with an iris used to estimate the beam profile at the center of the trap. (b) Beam profile recorded behind the bender at the location of the trap.

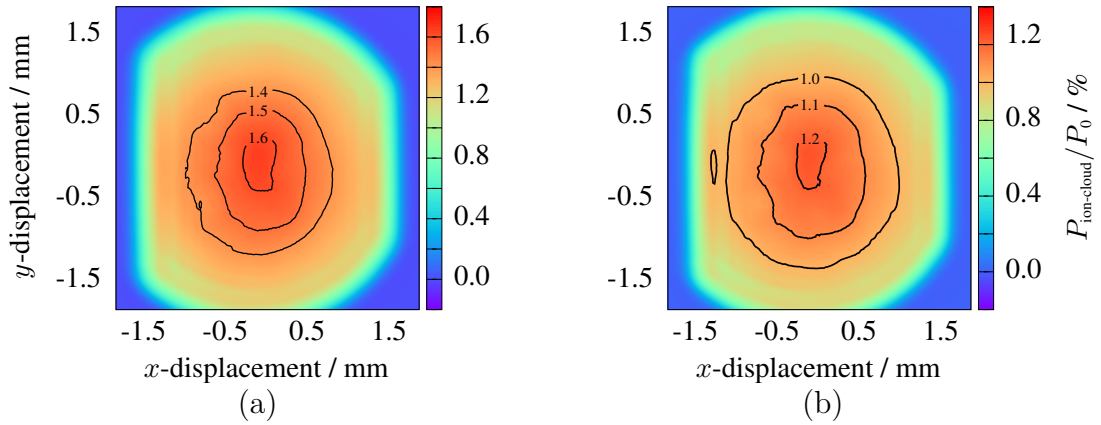


Figure 3.13: Ratio of the power-density covering the ion cloud and the total power density as a function of the displacement between laser and ion cloud. (a): $r_c = 0.21$ mm, (b): $r_c = 0.18$ mm. The D-shaped profile is caused by the bender rods.

# Bibliography


[1] D. Gerlich. (2016). RF and AC generators, [Online]. Available: https://www.tu-chemnitz.de/physik/ION/Technology/RF_AC_oscillator/ (visited on 08/10/2016).

[2] O. Asvany and S. Schlemmer, "Numerical simulations of kinetic ion temperature in a cryogenic linear multipole trap", *International Journal of Mass Spectrometry*, vol. 279, no. 2–3, pp. 147–155, 2009. DOI: 10.1016/j.ijms.2008.10.022.

[3] D. Gerlich, G. Jerke, U. Muck, and U. Person. (1990). Schnelles ventil zur erzeugung sehr kurzer gasimpulse, [Online]. Available: https://www.tu-chemnitz.de/physik/ION/Technology/Piezo_Valve/documentation%20pulsed%20valve.pdf (visited on 08/10/2016).

[4] N. R. Daly, "Scintillation type mass spectrometer ion detector", *Review of Scientific Instruments*, vol. 31, no. 3, pp. 264–267, 1960. DOI: 10.1063/1.1716953.

[5] D. C. Morton, "Atomic data for resonance absorption lines. II. Wavelengths longward of the Lyman limit for heavy elements", *The Astrophysical Journal Supplement Series*, vol. 130, no. 2, pp. 403–436, 2000. DOI: 10.1086/317349.

[6] L. Ricci, M. Weidemüller, T. Esslinger, A. Hemmerich, C. Zimmermann, W. K. V. Vuletic, and T. Hänsch, "A compact grating-stabilized diode laser system for atomic physics", *Optics Communications*, vol. 117, no. 5–6, pp. 541–549, 1995. DOI: 10.1016/0030-4018(95)00146-Y.

[7] H. Tanuma, H. Fujimatsu, and N. Kobayashi, "Ion mobility measurements and thermal transpiration effects in helium gas at 4.3 k", *The Journal of Chemical Physics*, no. 113, pp. 1738–1744, 5 2000. DOI: 10.1063/1.481976.

[8] S. Trippel, J. Mikosch, R. Berhane, R. Otto, M. Weidemüller, and R. Wester, "Photodetachment of cold $OH^-$ in a multipole ion trap", *Physical Review Letters*, vol. 97, pp. 1–4, 193003 2006. DOI: 10.1103/PhysRevLett.97.193003.

[9] K. Okada, K. Yasuda, T. Takayanagi, M. Wada, H. A. Schuessler, and S. Ohtani, "Crystallization of $Ca^+$ ions in a linear rf octupole ion trap", *Physical Review A*, vol. 75, pp. 1–10, 033409 2007. DOI: 10.1103/PhysRevA.75.033409.

[10] W. Demtröder, *Laser spectroscopy*, 3rd ed. Springer, 2003.

4

*I am slowly coming to the conclusion that it's more important to learn to work with what you've got, under the circumstances you've been given, than wishing for different ones.*

Charlotte Eriksson

# Laser Induced Inhibition of Complex Growth

A variety of spectroscopic methods have been used to probe trapped ions. Most of these schemes have specific requirements and are not universally applicable. For example, a reasonable quantum yield is necessary for laser induced fluorescence or a suitable reaction pathway needs to be known in case of laser induced reactions [1]. The stability of large molecules such as $C_{60}^+$ or PAHs require several photons for photofragmentation spectroscopy and bearing further difficulties [2]. Usually, tagging experiments have been used to overcome the constraints in cases where spectra of the bare species are difficult to obtain with the drawback of possible shifts of the observed absorptions. On the other hand, it is possible to excite the parent ion such, that the attachment of the weakly bound atom is suppressed. This effect has been observed when the association reaction

$$CO^+ + 2\,CO \rightarrow (CO)_2^+ + CO \tag{4.1}$$

was impeded by resonant rotational excitation of the primary Ions [3]. In case of vibrational or electronic transitions, this method has not been applied. A basic scheme of a laser induced inhibition of complex growth (LIICG) is illustrated in Figure 4.1. In the following sections it will be discussed in further detail for the example $N_2^+$. The advantage of using $N_2^+$ as a benchmark system is that this molecule is one of the most investigated diatomic molecule. This is beneficial for analyzing and understanding the involved processes of LIICG.

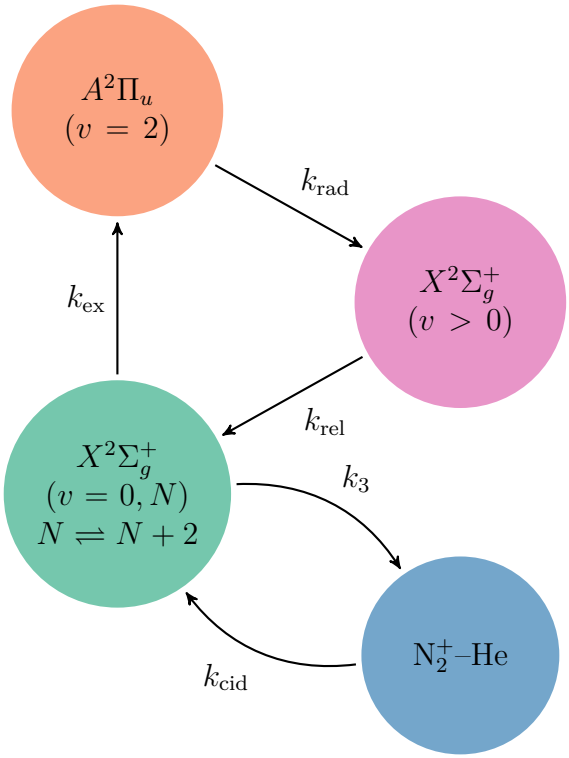


Figure 4.1: Diagram illustrating the involved processes for laser induced inhibition of complex growth on the example of $N_2^+$: Vibrationally hot $N_2^{+*}$ ions (●) enter the trap and relax via collisions with the buffer gas to the $X^2\Sigma_g^+$ vibrational ground state (●). $N_2^+$–He complexes (●) are formed via ternary association with a rate constant $k_3$ and are recycled by collision induced dissociation, $k_{\mathrm{CID}}$. The inhibition takes place by permanent resonant excitation into the $A^2\Pi_u$ excited state (●) from where it radiates back with $k_{\mathrm{rad}}$ into an excited vibrational level of the ground state.

## 4.1 Proof of Principle on $N_2^+$

The LIICG scheme has been studied for the $A^2\Pi_u \leftarrow X^2\Sigma_g^+$ electronic transition of $N_2^+$. This system was first identified in 1951 in the aurora glow by Meinel and observed experimentally by Dalby & Douglas [4, 5]. The $X^2\Sigma_g^+$ ground state is a Hund's case (b), where the rotational angular momentum **N** couples with the electronic spin-angular momentum **S** to form the total angular momentum **J**. The $A^2\Pi_u$ excited state can be described with Hund's case (a), exhibiting a strong spin-orbit splitting [6]. The resulting energy level diagram based on these considerations is illustrated in Figure 4.2 together with the involved transitions that will be studied in the LIICG experiment.

### 4.1.1 Experimental Conditions

The experiment has been performed in the linear configuration of the apparatus using a 22-pole trap. $N_2^+$ ions were created by electron bombardment of the neutral gas. The trap has been filled for 10 ms with $N_2^+$, while a piezo valve was gated for 500 ms. During that time ions were irradiated continuously with 10 mW using the cw Ti:Sapphire ring laser having bandwidth of 500 kHz. After another 480 ms, when the helium pressure had decreased by orders of magnitude, the ions were extracted. The trap temperature has been kept at $T_{\mathrm{nom}} = 5\,\mathrm{K}$, which is also the temperature of the helium buffer gas.

### 4.1.2 Spectroscopy

In Figure 4.3 the resulting spectrum of $N_2^+$ measured by LIICG is shown. The number of complexes per filling is plotted against the wavenumber, where each data point represents an average of 10 samples. The observed absorption lines were evaluated with Gaussian functions and the obtained parameters are summarized in Table 4.1 together with literature values for comparison. All lines are well-resolved, except the $Q_{11}(J = 1.5)$ and $R_{12}(J = 0.5)$. Deviations of the rotational lines to the literature values can be explained by an uncalibrated wavemeter. Assuming an offset of $\Delta\tilde{\nu} = 0.015\,\mathrm{cm}^{-1}$, the observed lines agree within $\Delta\tilde{\nu} = 0.005\,\mathrm{cm}^{-1}$.

The Franck-Condon factor of the vibronic transition reveals that 56 % of electronically excited $N_2^+$ ions relax directly back in to $X^2\Sigma_g^+(v = 0)$ ground state and thus only 44 % of the complexes contribute to the spectrum [7]. Furthermore, the

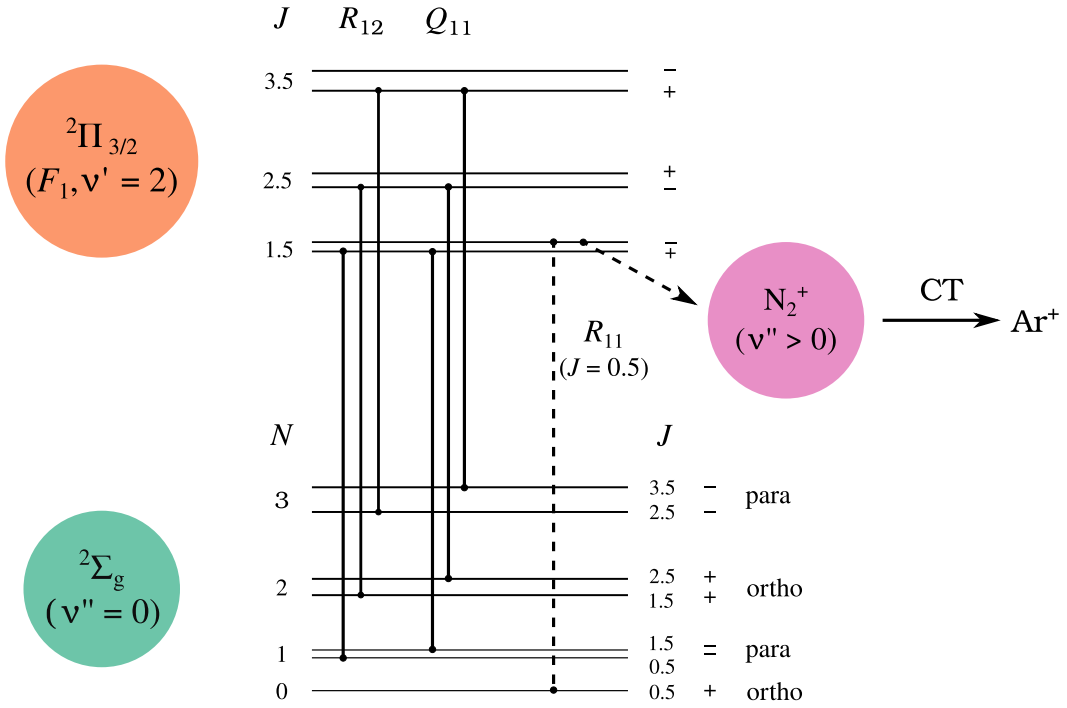


Figure 4.2: Schematic energy level diagram of $N_2^+$ depicting some of the involved transitions together with the charge transfer reaction pathway to $Ar^+$. The $^2\Pi_{1/2}$ level has been neglected.

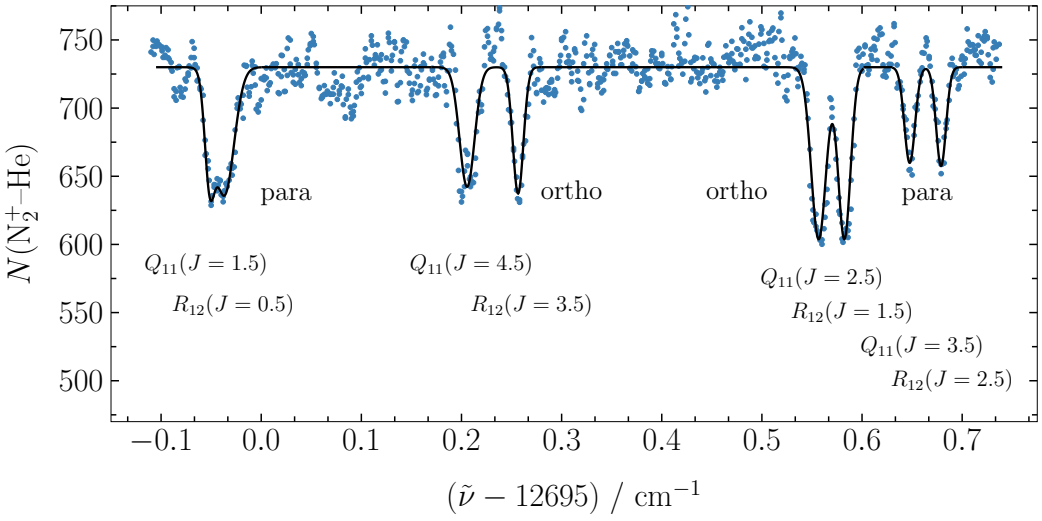


Figure 4.3: Part of the (2,0) band of the $A^2\Pi_u \leftarrow X^2\Sigma_g^+$ system of $N_2^+$ spectrum measured with LIICG. The number of $N_2^+$–He complexes per filling (●) is plotted against the wavenumber. Gaussian functions (—) have been used for fitting.

| $\tilde{\nu}_{\mathrm{exp}}$ / cm$^{-1}$ | atten. / % | assignment | $\tilde{\nu}_{\mathrm{lit}}$ / cm$^{-1}$ | $\Delta\tilde{\nu}$ / cm$^{-1}$ |
|---|---|---|---|---|
| 12694.952 | 37 | $Q_{11}(J = 1.5)$ para | 12694.967 | -0.015 |
| 12694.963 | | $R_{12}(J = 0.5)$ para | 12694.967 | -0.004 |
| 12695.206 | 19 | $Q_{11}(J = 4.5)$ ortho | 12695.226 | -0.020 |
| 12695.257 | | $R_{12}(J = 3.5)$ ortho | 12695.269 | -0.012 |
| 12695.557 | 26 | $Q_{11}(J = 2.5)$ ortho | 12695.574 | -0.017 |
| 12695.582 | | $R_{12}(J = 1.5)$ ortho | 12695.599 | -0.017 |
| 12695.648 | 32 | $Q_{11}(J = 3.5)$ para | 12695.654 | -0.016 |
| 12695.678 | | $R_{12}(J = 2.5)$ para | 12698.689 | -0.011 |
| 12698.805 | | $R_{11}(J = 0.5)$ | 12698.800 | +0.005 |

Table 4.1: Observed lines for the (2,0) band of the $A^2\Pi_u \leftarrow X^2\Sigma_g^+$ system of $N_2^+$ using LIICG. For comparison literature values are also given, taken from Ref. [8].

ortho:para ratio of 2:1 has to be considered and leads to the observed attenuations listed in Table 4.1. Surprisingly, they do not represent the population of the rotational levels. For example the $N = 4$ rotational state has a theoretical population of 1.6 %, while the obtained depletion is 19%. This reflects a very efficient inhibition of complex formation and could be explained by fast rotational relaxation.

### 4.1.3 Laser Induced Charge Transfer Reaction to Ar

The spectrum shown in Figure 4.3 is not observed if the laser is irradiated after switching off the piezo valve. This indicates that the photons interact with the bare ion and the spectrum is not obtained by fragmentation of the complex. To unequivocally conclude that the spectrum is not shifted, another approach was employed called laser induced charge transfer (LICT). This is based on the electron transfer reaction

$$N_2^+ + Ar \rightarrow N_2 + Ar^+. \tag{4.2}$$

The charge transfer is very efficient if $N_2^+$ is vibrationally excited because the reaction is exothermic, whereas the reaction from the ground vibrational and rotational state is 0.18 eV endothermic [9]. A LICT spectrum obtained for the $R_{11}(J = 0.5)$ transition of $N_2^+$ is shown in Figure 4.4 together with the one recorded with LIICG. Analysis of the measured profiles gives FWHMs of $\Delta\nu_{\mathrm{LIICG}} = 345$ MHz and $\Delta\nu_{\mathrm{LICT}} = 325$ MHz which yields translational temperatures of $T_{\mathrm{LIICG}} = 45$ K and $T_{\mathrm{LICT}} = 40$ K, respectively. These are much higher than the expected Doppler width of $\Delta\nu = 121$ MHz at a nominal temperature of 5 K. Parasitic heating effects in the trap due the end-cap electrodes or patch potentials may be possible

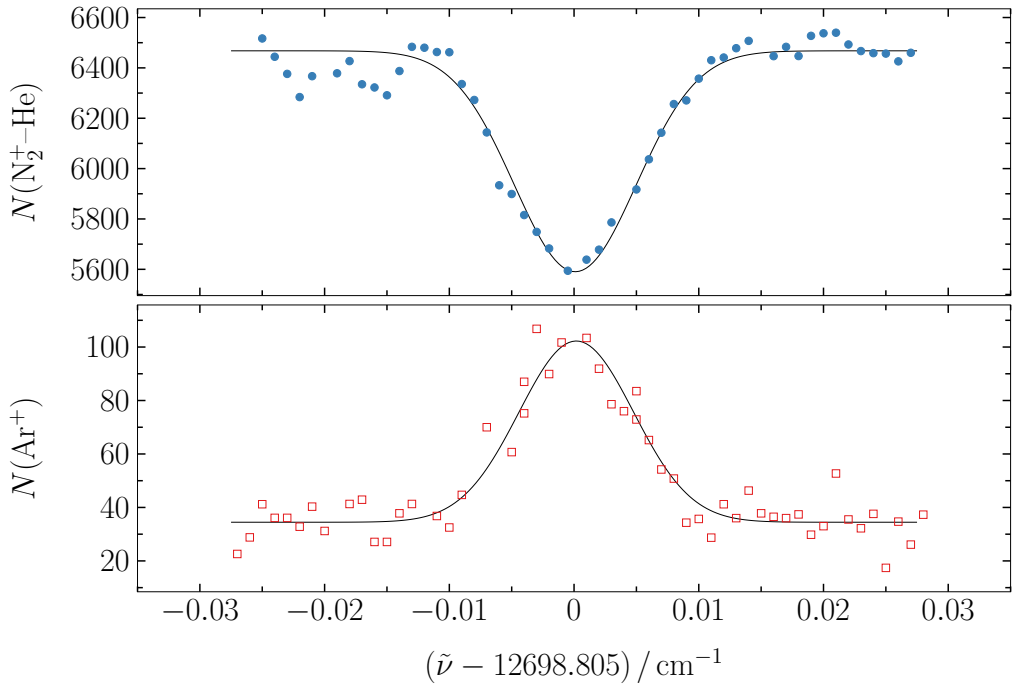


Figure 4.4: $R_{11}(J = 0.5)$ line measured with (●) LIICG and (□) LICT using a laser power of $P = 5\,\mathrm{mW}$. The extracted linewidths from Gaussian fits (–) are $\Delta\nu_{\mathrm{LIICG}} = 345\,\mathrm{MHz}$ for the inhibition and $\Delta\nu_{\mathrm{LICT}} = 325\,\mathrm{MHz}$ for the charge transfer method.

reasons. A rotational temperature can be calculated from the mass weighted average of the translational temperatures of the collision partners using equation (2.23) to $T_{\mathrm{rot}} = 10.6\,\mathrm{K}$. Furthermore, both methods agree in frequency within $\Delta\tilde{\nu} = 0.001\,\mathrm{cm}^{-1}$.

### 4.1.4 Dynamical Processes

For a qualitative discussion about the obtained results and involved processes, numerical simulations have been employed. An ion ensemble is assumed to be composed of ortho-$N_2^+$ with rotational states $N = 0, 2, 4, 6$; $N_2^+$–He and vibrationally excited $N_2^+(v > 0)$. Laser excitation has been achieved from the $N = 2$ rotational level with a calculated rate of $500\,\mathrm{s}^{-1}$, although an explicit electronic excitation is neglected [10]. This approximation is valid, because the radiative lifetime of about $10\,\mu\mathrm{s}$ is short compared to all other time constants (ms) [6] . Rotational relaxation is accounted for by three rates $k_{N\to N-2}$. The reverse rates are then determined from the detailed balance relation using microscopic reversibility (Appendix A). The values used, derived rate constants and conditions are summarized in Table

| Parameter | Initial Value | Result | |
|---|---|---|---|
| | | Without Laser | With Laser |
| $N_2^+$–He | 0.0 | 0.045 | 0.012 |
| $N_2^+(v > 0)$ | 0.5 | 0.000 | 0.743 |
| $N_2^+(N = 0)$ | 0.0 | 0.453 | 0.082 |
| $N_2^+(N = 2)$ | 0.0 | 0.474 | 0.071 |
| $N_2^+(N = 4)$ | 0.0 | 0.025 | 0.048 |
| $N_2^+(N = 6)$ | 0.5 | 0.002 | 0.015 |
| $k_3$ | $1 \times 10^{-31}\,\mathrm{cm^6 s^{-1}}$ | | |
| $k_{\mathrm{CID}}$ | $1 \times 10^{-14}\,\mathrm{cm^3 s^{-1}}$ | | |
| $k_{\mathrm{rel}}$ | | $1 \times 10^{-14}\,\mathrm{cm^3 s^{-1}}$ | |
| $k_{0\to2}$ | | $1 \times 10^{-13}\,\mathrm{cm^3 s^{-1}}$ | |
| $k_{2\to4}$ | | $1 \times 10^{-13}\,\mathrm{cm^3 s^{-1}}$ | |
| $k_{4\to6}$ | | $1 \times 10^{-13}\,\mathrm{cm^3 s^{-1}}$ | |
| $k_{\mathrm{laser}}$ | $500\,\mathrm{s^{-1}}$ | | |
| $n$[He] | $4.75 \times 10^{15}\,\mathrm{cm^{-3}}$ | | |
| $T_{\mathrm{rot}}$ | 10.6 K | | |

Table 4.2: Parameters used and derived from simulations. The initial rates are obtained from the experiment.

4.2.

An initial population of 0.5 for vibrationally excited ions was assumed, accounting for the conditions from the ion source due to electron bombardment. This population is equilibrated much slower than the rotational relaxation with ~ 40 ms (Figure 4.5 (a)). Collision induced dissociation is responsible for an inefficient production of $N_2^+$–He complexes and leads to the experimentally observed 4.5 % reached after 100 ms. With a given Langevin rate of $k_L = 6 \times 10^{-10}\,\mathrm{cm^3 s^{-1}}$, the vibrational relaxation into the ground state requires $3 \times 10^5$ collisions with helium. This corresponds to a rate coefficient of $k_{\mathrm{rel}} = 1 \times 10^{-14}\,\mathrm{cm^3 s^{-1}}$. Theoretical calculations of the rate for quenching the $(v = 1, j = 0)$ level of $N_2^+$ in collision with He are reported to be similar with 1-3 $\times 10^{-14}\,\mathrm{cm^3\,s^{-1}}$ [11].

### 4.1.5 Conclusion

Formation of ion–He complexes via ternary association is always achievable providing cryogenic conditions and sufficient collisions; therefore, LIICG is considered to be generally applicable. It is not yet understood why the fragmentation of the $N_2^+$–He could not be observed. This has also been reported recently for measurements of vibrational spectra of $CH_5^+$ using LIICG [12, 13]. A possibility could be

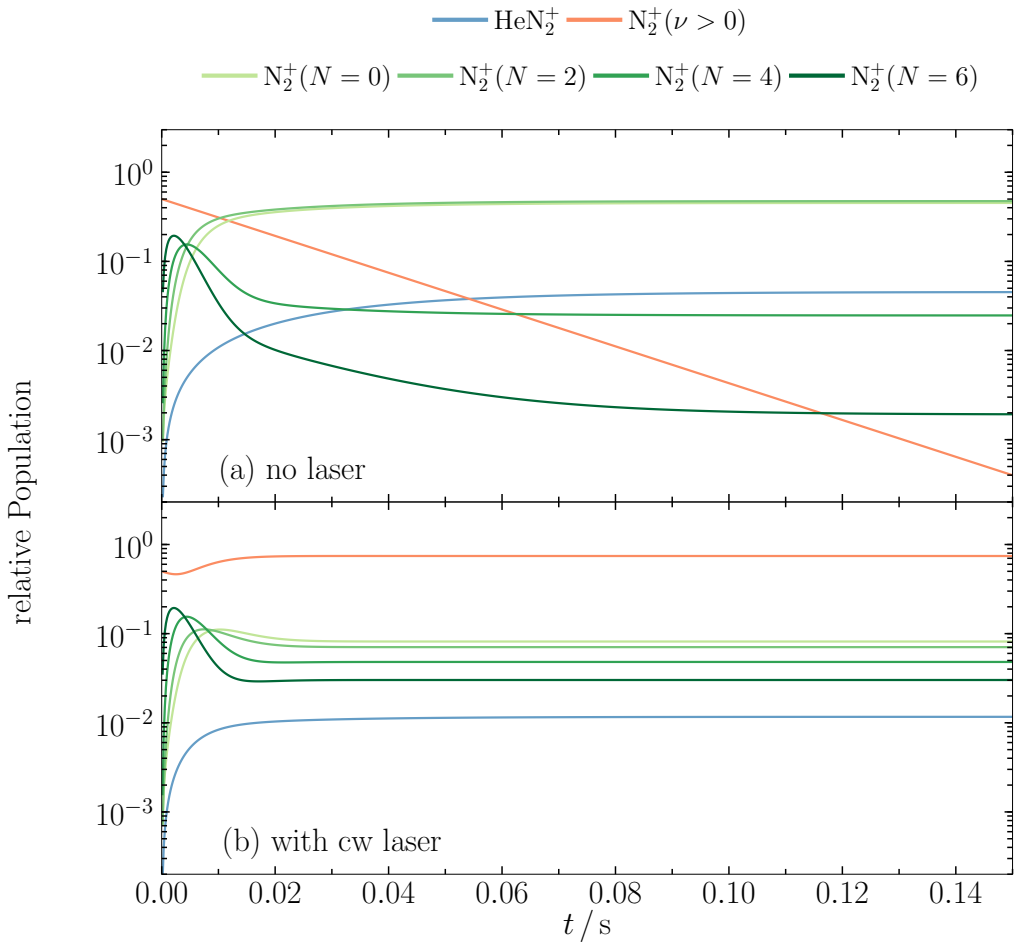


Figure 4.5: Simulation of the relative populations for a trapped ortho-$N_2^+$ ensemble. Considered are the rotational states $N = 0, 2, 4, 6$, vibrationally excited $N_2^+$ and $N_2^+$–He complexes. In (a) the dynamics are simulated without laser, in (b) with laser excitation via the rotational state $N = 2$.

large induced shifts by the helium messenger. Another reason could be the short lifetime of the dissociating complex resulting in a broad transitions. In case of $N_2^+$ gas-phase spectra have been very well-characterized which allowed a detailed analysis of the underlying processes. However, utilizing LIICG to obtain electronic spectra of other molecules appears to be a difficult task as will be discussed in the following sections.

## 4.2 $NCCN^+$–He

The $B^2\Sigma_u^+ \leftarrow X^2\Pi_g$ electronic transition of the cyanogen cation was previously studied using photoelectron spectroscopy, matrix isolation and a two-color, two-photon dissociation scheme in the gas-phase [14–16]. The neutral and cationic species are of astrophysical relevance as both have been identified in Titan's atmosphere [17, 18]. However, the lack of a dipole moment of symmetric dicyano analogues impede their detection by radio astronomy in the ISM. It was reported to exhibit lifetimes of a few picoseconds in the $B^2\Sigma_u^+$ state because of fast intramolecular redistribution of energy and thus made it an interesting candidate for obtaining spectra with LIICG.

Several known absorption bands of $NCCN^+$–He were recorded, from which the $2_0^1$ and the $2_0^1 5_0^2/4_0^4$ combination bands are shown in Figure 4.6 (b). Apart from the latter band system, all transition could be fit with Lorentzian functions reflecting a natural broadening. A summary of the observed band maxima compared to reported values are listed in Table 4.3. Transitions have been measured using the Ti:Sapphire ring laser with a 3 GHz bandwidth. In the upper trace, the reproduced spectrum by Rudnev *et al.* is plotted as a reference [16]. The reported values for the frequencies do not reflect the band maxima, which has been found by an one-color, two-photon fragmentation experiment of $NCCN^+$. A column with corrected values $\nu^*$ for better comparison are therefore given in Table 4.3.

Large shifts ranging from 11-19 $cm^{-1}$ with respect to the absorption bands of $NCCN^+$ were observed, indicating that the spectra were obtained due to photofragmentation of the complex. Attempts to observe any inhibition by irradiating the ions while gating the piezo valve did not reveal the spectrum of the cyanogen cation. The ternary rate constant of $k_3 = 5 \times 10^{-31}\,cm^6s^{-1}$ is slightly larger as in case of $N_2^+$, which allowed measurements with 2 He and 3 He attached to cyanogen. The slope of a linear interpolation from the central wavelengths yields a shift of $11.5 \pm 0.3\,cm^{-1}$ per He, also implicating that the absorptions were obtained via photodissociation. The intercept at $n = 0$ leads in case of the origin band to $\nu = 11\,253 \pm 1\,cm^{-1}$ which is in a good agreement to the value of the two-color, two-photon experiment. The FWHMs compare well with the bare cation, consequently the ions are equilibrated to the vibrational ground state.

In the lower trace of Figure 4.6 the spectrum of the $2_0^1$ absorption band is shown, when the piezo valve was actuated using a 5 ms TTL-pulse at an amplitude of

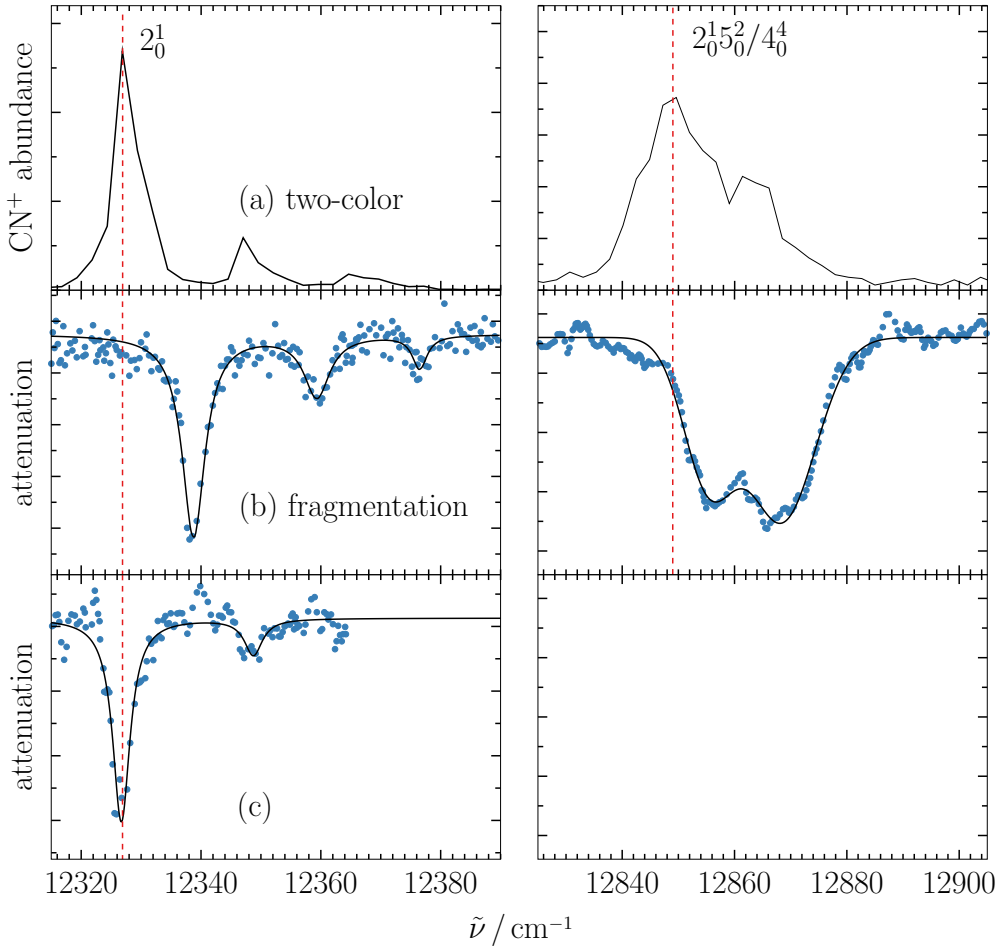


Figure 4.6: Absorption spectra of two bands of the $B^2\Sigma_u^+ \leftarrow X^2\Pi_g$ electronic transition of cyanogen cation obtained with two-color, two-photon dissociation (a) and fragmentation of the complex (b). In (c) the piezo valve was actuated by a 5 ms TTL pulse. Shown are the $2_0^1$ and $2_0^1 5_0^2/4_0^4$ absorption bands. Experimental data (•) are fit with Lorentzian (–, left panel (b,c)) and Gaussian functions (–, right panel (b)). The dashed line (--) indicates the band maximum of the reference spectrum (a) which was reproduced from Ref. [16].

| NCCN$^+$–He | | | NCCN$^+$ [16] | |
|---|---|---|---|---|
| $n$He | $\tilde{\nu}_c$ / cm$^{-1}$ | $\tilde{\nu}^*$ / cm$^{-1}$ | $\tilde{\nu}$ / cm$^{-1}$ | assignment |
| 1 | 11 268 | 11 265 | 11 253 | $0_0^0$ |
| 2 | 11 280 | 11 277 | | |
| 3 | 11 291 | 11 288 | | |
| 1 | 11 817 | 11 814 | 11 799 | $5_0^2$ |
| 2 | 11 829 | 11 824 | | |
| 1 | 12 051 | 12 048 | 12 032 | $4_0^2$ |
| 1 | 12 339 | 12 335 | 12 319 | $2_0^1$ |
| 1 | 12 584 | 12 581 | 12 562 | ? |
| 2 | 12 595 | 12 591 | | |
| 3 | 12 607 | 12 603 | | |
| 1 | 12 855 | 12 848 | 12 837 | $2_0^1 5_0^2/4_0^4$ |

Table 4.3: Comparison of the properties of band maxima obtained for electronic transition $B^2\Sigma_u^+ \leftarrow X^2\Pi_g$ of NCCN$^+$–He and NCCN$^+$. $^*$ denotes shifted values for $\nu_c$, because the literature values do not represent the band maxima.

300 V. Conditions could also be created such, that the absorption bands in (b) and (c) were recorded in the same spectrum. In that particular case, the piezo valve was gated for 500 ms and the complexes have been probed at the end of the trapping cycle after evacuation of the buffer gas. This indicates, that (c) is the result of photofragmentation and different binding sites for the helium exist. A slow excitation and a fast relaxation rate of NCCN$^+$ may be reasons for not observing the inhibition signal.

## 4.3 $C_{14}H_{10}^+$–He

Phenanthrene belongs to the group of PAHs that have been considered as a carrier of the DIBs. PAHs need a large amount of energy before they start to fragment. This requires usually high laser power densities leading to unwanted side effects like saturation broadening. First gas-phase data have been reported by Bréchignac and coworkers for the $D_2 \leftarrow D_0$ electronic transition [19]. A special technique, the so-called shift additivity rule, allows an extrapolation from measurements of M$^+$–Ar and M$^+$–Ar$_2$ back to the spectrum of the bare cation [20].

Phenanthrene was evaporated slightly above room temperature and ionized by electron bombardment. The spectrum for $C_{14}H_{10}^+$–He covering the regions of the two strongest bands in Figure 4.7 was obtained by probing the complex in a 22-pole trap at 4.5 K. The band maxima are almost identical within the uncertainty

| | $C_{14}H_{10}^+$–He | | $C_{14}H_{10}^+$ [19] | |
|---|---|---|---|---|
| $n$He | $\tilde{\nu}$ / cm$^{-1}$ | $\Delta\tilde{\nu}$ / cm$^{-1}$ | $\tilde{\nu}$ / cm$^{-1}$ | $\Delta\tilde{\nu}$ / cm$^{-1}$ |
| 1 | $11212 \pm 1$ | $9 \pm 2$ | 11212 | 16 |
| 2 | $11211 \pm 1$ | | | |
| 1 | $11752 \pm 2$ | $9 \pm 2$ | 11754 | 16 |

Table 4.4: Observed parameters of $C_{14}H_{10}^+$–He absorption bands compared to reported values.

to previously reported values (Table 4.4) [19]. In case of a second helium attached, a shift for the origin band of $\sim 0.5\,\mathrm{cm}^{-1}$ is observed compared to $C_{14}H_{10}^+$–He also indicating fragmentation of the complex rather than inhibition of its formation. Conditions to identify LIICG could not be obtained, probing the complex with LIICG or in the fragmentation mode result in the same spectra.

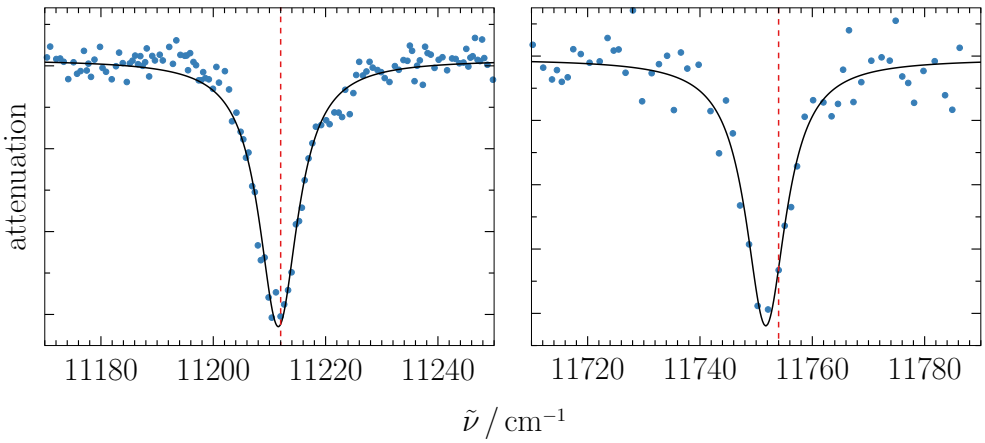


Figure 4.7: Two absorption bands of the $D_2 \leftarrow D_0$ electronic transition of $C_{14}H_{10}^+$–He. Experimental data (•) are fit with Lorentzian functions (–). Dashed lines (--) indicate the band maxima from Ref. [19].

## 4.4 Conclusion

Laser induced inhibition of complex growth was successfully applied to $N_2^+$, but could not be observed in the cases of $NCCN^+$ and $C_{14}H_{10}^+$. Finding the right conditions for LIICG is challenging and the dynamics of the underlying processes still need further investigations. Positive results have been reported recently in the case of $H_3^+$ and $CH_5^+$ by state-specific excitation of trapped molecules via their IR transitions indicating the relevance of LIICG as a spectroscopic method [12, 13].

Furthermore, electronic spectra could be measured by photofragmentation of the complexes. The cyanogen cation yields significant discrepancies in the band maxima with and without the presence of a He atom revealing shifts of up to $19\,\mathrm{cm}^{-1}$. In an earlier study by Bieske *et al.* . the $B^2\Sigma_u^+ \leftarrow X^2\Sigma_g^+$ electronic transition of $N_2^+$–He was recorded with shifts of less than $1\,\mathrm{cm}^{-1}$ [21]. This agrees more with the results for $C_{14}H_{10}^+$–He where only small shifts are present. By attachment of 2 He and 3 He to $NCCN^+$, an extrapolation of the center wavelength of the $2_0^1$ transition to the bare cation could be achieved. In case of neutral PAH–helium complexes produced in a supersonic jet expansion, it has been shown that by increasing the number of rings unpredictable spectral shifts occur [22]. However, the results from photofragmentation experiments of weakly bound complexes using helium as a messenger could be an alternative spectroscopic method to LIICG. The widths of the absorption bands are comparable with reported values, if not even narrower. This indicates that the internal degrees of freedom of the two molecules have been equilibrated to the vibrational ground state.

# Bibliography


[1] S. Schlemmer and O. Asvany, "Laser induced reactions in a 22-pole ion trap", *Journal of Physics: Conference Series*, vol. 4, no. 1, pp. 134–141, 2005. DOI: 10.1088/1742-6596/4/1/018.

[2] M. Foltin, M. Lezius, P. Scheier, and T. D. Märk, "On the unimolecular fragmentation of $C_{60}^+$ fullerene ions: The comparison of measured and calculated breakdown patterns", *The Journal of Chemical Physics*, vol. 98, no. 12, pp. 9624–9634, 1993. DOI: 10.1063/1.464393.

[3] D. Gerlich and T. Rox, "Association reactions with state selected ions at meV collision energies: $CO^+(v = 0, j) + 2\,CO \rightarrow (CO)_2^+ + CO$", *Zeitschrift für Physik D Atoms, Molecules and Clusters*, vol. 13, no. 3, pp. 259–268, 1989. DOI: 10.1007/BF01436963.

[4] A. B. Meinel, "The auroral spectrum from 6200 to 8900 Å", *Astrophysical Journal*, vol. 113, p. 583, 1951. DOI: 10.1086/145427.

[5] F. W. Dalby and A. E. Douglas, "Laboratory observation of the $A^2\Pi - X^2\Sigma$ bands of the $N_2^+$ molecule", *Physical Review*, vol. 84, no. 4, p. 843, 1951. DOI: 10.1103/PhysRev.84.843.

[6] T. A. Miller, T. Suzuki, and E. Hirota, "High resolution, cw laser induced fluorescence study of the $A^2\Pi_u - X^2\Sigma_g^+$ system of $N_2^+$", *The Journal of Chemical Physics*, vol. 80, no. 10, pp. 4671–4678, 1984. DOI: 10.1063/1.446530.

[7] F. R. Gilmore, R. R. Laher, and P. J. Espy, "Franck-Condon factors, r-centroids, electronic transition moments, and Einstein coefficients for many nitrogen and oxygen band systems", *Journal of Physical and Chemical Reference Data*, vol. 21, no. 5, pp. 1005–1107, 1992. DOI: 10.1063/1.555910.

[8] I. Bachir, H. Bolvin, C. Demuynck, J. Destombes, and A. Zellagui, "High-resolution optogalvanic spectrum of $N_2^+$ using a Ti:Sapphire Laser: The (2,0) vibration band of the Meinel system $A^2\Pi_u - X^2\Sigma_g^+$", *Journal of Molecular Spectroscopy*, vol. 166, no. 1, pp. 88–96, 1994. DOI: 10.1006/jmsp.1994.1174.

[9] F. Grieman, J. Hansen, and J. Moseley, "Ion spectroscopy of the $N_2^+(4,0)$ Meinel band using Ar charge exchange detection", *Chemical Physics Letters*, vol. 85, no. 1, pp. 53–56, 1982. DOI: 10.1016/0009-2614(82)83459-3.

[10] S. Schlemmer, T. Kuhn, E. Lescop, and D. Gerlich, "Laser excited $N_2^+$ in a 22-pole ion trap: Experimental studies of rotational relaxation processes", *International Journal of Mass Spectrometry*, vol. 185, no. 185, pp. 589–602, 1999. DOI: 10.1016/S1387-3806(98)14141-6.

[11] T. Stoecklin and A. Voronin, "Strong isotope effect in ultracold collision of $N_2^+$ ($\nu = 1$, $j = 0$) with He: A case study of virtual-state scattering", *Physical Review A*, vol. 72, pp. 1–4, 042714 2005. DOI: 10.1103/PhysRevA.72.042714.

[12] I. Savić, D. Gerlich, O. Asvany, P. Jusko, and S. Schlemmer, "Controlled synthesis and analysis of He-$H_3^+$ in a 3.7 K ion trap", *Molecular Physics*, vol. 113, no. 15–16, 2015. DOI: 10.1080/00268976.2015.1037802.

[13] O. Asvany, S. Brünken, L. Kluge, and S. Schlemmer, "COLTRAP: A 22-pole ion trapping machine for spectroscopy at 4 K", *Applied Physics B: Lasers and Optics*, vol. 114, no. 1, pp. 203–211, 2014. DOI: 10.1007/s00340-013-5684-y.

[14] M. Hochlaf, T. Baer, X.-M. Qian, and C. Y. Ng, "A vacuum ultraviolet pulsed field ionization-photoelectron study of cyanogen cation in the energy range of 13.2-15.9 eV", *The Journal of Chemical Physics*, vol. 123, no. 144302, pp. 1–8, 2005. DOI: 10.1063/1.2037607.

[15] E. Riaplov, M. Wyss, J. P. Maier, M. Hochlaf, and P. Rosmus, "Electronic and infrared absorption spectra of $NCCN^+$", *International Journal of Mass Spectrometry*, vol. 223–224, pp. 107–114, 2003. DOI: 10.1016/S1387-3806(02)00784-4.

[16] V. Rudnev, C. A. Rice, and J. P. Maier, "$B^2\Sigma_u^+ \leftarrow X^2\Pi_g$electronic spectrum of $NCCN^+$ in the gas phase", *The Journal of Chemical Physics*, vol. 129, no. 134315, pp. 1–4, 2008. DOI: 10.1063/1.2989982.

[17] J. H. Waite Jr., D. T. Young, T. E. Cravens, A. J. Coates, F. J. Crary, B. Magee, and J. Westlake, "The process of Tholin formation in Titan's upper atmosphere", *Science*, vol. 316, no. 5826, pp. 870–875, 2007. DOI: 10.1126/science.1139727.

[18] M. J. McEwan, G. B. Scott, and V. G. Anicich, "Ion-molecule reactions relevant to Titan's ionosphere", *International Journal of Mass Spectrometry and Ion Processes*, vol. 172, no. 3, pp. 209–219, 1998. DOI: 10.1016/S0168-1176(97)00236-X.

[19] P. Bréchignac and T. Pino, "Electronic spectra of cold gas phase PAH cations: Towards the identification of the diffuse interstellar bands carriers", *Astronomy and Astrophysics*, vol. 343, pp. L49–L52, 1999.

[20] P. Hermine, P. Parneix, B. Coutant, F. G. Amar, and P. Bréchignac, "Resonant two-photon two-color photoionization (R2P2CI) spectra of aniline-$Ar_n$ clusters: Isomer structures and solvent shifts", *Zeitschrift für Physik D Atoms, Molecules and Clusters*, vol. 22, no. 2, pp. 529–539, 1992. DOI: 10.1007/BF01426095.

[21] E. J. Bieske, A. M. Soliva, A. Friedmann, and J. P. Maier, "Electronic spectra of $N_2^+$-$(He)_n$ ($n$=1, 2, 3)", *The Journal of Chemical Physics*, vol. 96, no. 28, pp. 28–34, 1992. DOI: 10.1063/1.462517.

[22] U. Even, I. Al-Hroub, and J. Jortner, "Small He clusters with aromatic molecules", *The Journal of Chemical Physics*, vol. 115, no. 5, pp. 2069–2073, 2001. DOI: 10.1063/1.1385154.

5

*We must trust to nothing but facts: These are presented to us by Nature, and cannot deceive. We ought, in every instance, to submit our reasoning to the test of experiment, and never to search for truth but by the natural road of experiment and observation.*

■ Antoine Lavoisier

# Electronic Spectra of Fullerenes

This chapter discusses the electronic spectra of weakly bound fullerene-helium complexes obtained by photofragmentation spectroscopy. Although the results presented in the preceding chapter are promising, finding the right conditions for LIICG can be a challenging task. The interaction between singly charged fullerenes and He is expected to be weaker than that of the previously investigated complexes. Binding energies of $\sim 90$ cm$^{-1}$ compared to, e.g., $\sim 135$ cm$^{-1}$ have been estimated in cases of $C_{60}^+$–He and $N_2^+$–He, respectively [1, 2]. Consequently, their electronic spectra are obtained via photofragmentation of these weakly bound complexes. The species of interest includes $C_{60}^+$, $C_{70}^+$, $C_{70}^{2+}$, and $C_{84}^+$. A focus is set to the characteristics of the obtained absorption bands namely frequencies, absorption cross-sections, relative intensities, and widths. These are the most important criteria for a comparison of laboratory spectra with DIBs [3].

All cations are produced via electron impact ionization. Therefore, a solid sample of the neutral compound is heated to 350-600°C until a vapor pressure of typically $\sim 10^{-6}$ mbar is reached. Complexes are then synthesized and probed in a 4-pole trap. In case of $C_{60}^+$ results obtained from measurements using a 22-pole trap are also discussed.

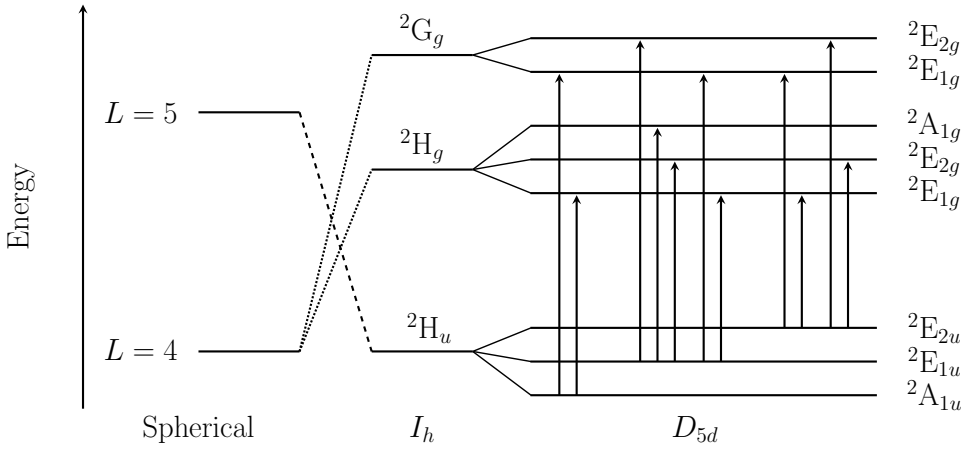


Figure 5.1: Correlation diagram for the reduction from spherical to $I_h$ and finally to the predicted $D_{5d}$ symmetry for $C_{60}^+$. Indicated with arrows are the dipole allowed transitions in the investigated spectral region, using the ordering of the energy levels according to Ref. [6]

## 5.1 $C_{60}^+$

Special attention has been raised when two bands in the astronomical spectrum toward several lines-of-sight at 9632 Å and 9577 Å have been observed, which lie in the proximity of two absorption bands of $C_{60}^+$ measured in a neon matrix experiment [4, 5]. In icosahedral $I_h$ symmetry the NIR absorption bands are assigned to $^2H_g \leftarrow ^2H_u$ and $^2G_g \leftarrow ^2H_u$ (Figure 5.1), respectively, but the terms involved are all distorted by Jahn–Teller effects [6, 7]. However, an unequivocally assignment of $C_{60}^+$ as a carrier of any DIB was awaiting the gas-phase spectra at low temperature because of shifts induced by the matrix environment.

### 5.1.1 $C_{60}^+$–He

The electronic photofragmentation spectrum of $C_{60}^+$–He in the NIR region is presented in Figure 5.2. Following the typical evaluation of astronomical data, the individual absorption bands are fit with Gaussian functions and normalized according to their relative intensities. The resulting parameters are listed in Table 5.5. Two strong absorption bands at (10 378.5±0.1) $cm^{-1}$ and (10 438.1±0.1) $cm^{-1}$ are dominating the spectrum, continued by two bands at (10 603.2 ± 0.1) $cm^{-1}$ and (10 674.2 ± 0.1) $cm^{-1}$ which are around three times weaker. The next absorption band appears at (10 693.3 ± 0.1) $cm^{-1}$ with an intensity of 7% of the 10 438 $cm^{-1}$ band.

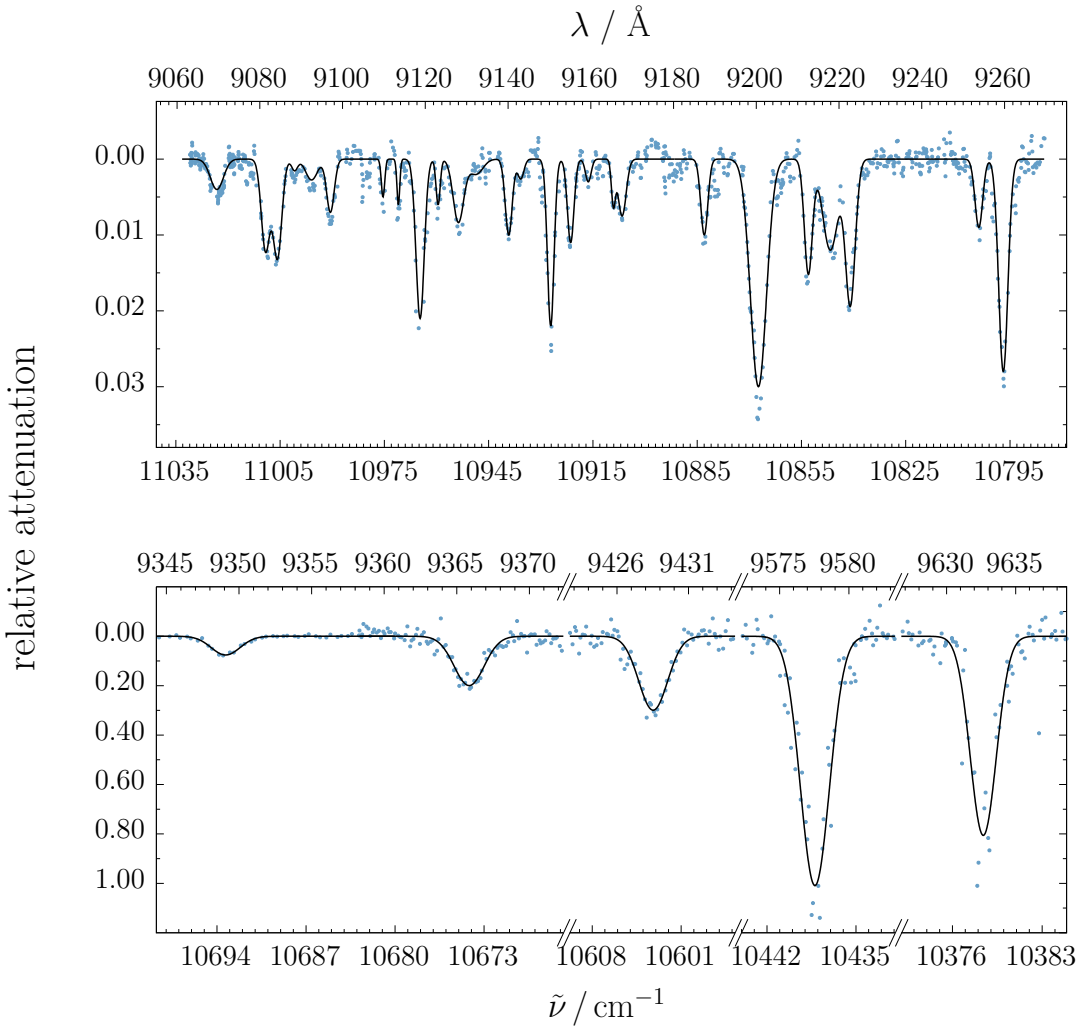


Figure 5.2: Absorption spectrum of $C_{60}^+$–He by measuring the attenuation as a function of the wavelength on the mass channel $m/z = 724$. The intensities of the bands have been normalized to the band maximum at $\lambda = 9577.5$ Å. Experimental data (•) has been individually fit using Gaussian functions (–).

An upper limit for translational temperature of 150 K for $C_{60}^+$ using equation (2.23) leads to $T_{\text{int}} = 5.8$ K. A calculated rotational envelope at these temperatures predicts a width of about 1 Å for $C_{60}$ [8]. A similar value can be expected for $C_{60}^+$ because the structural change from the neutral is assumed to be small. The measured transitions do not exhibit a rotationally resolved profile. FWHMs obtained from the fits with Gaussian functions are $(2.4 \pm 0.2)$ cm$^{-1}$ and $(2.7 \pm 0.2)$ cm$^{-1}$ for the band maxima at 10 379 and 10 438 cm$^{-1}$, respectively. In that case the absorption bands are lifetime broadened and this can be calculated to

$$\tau \approx \frac{1}{2\pi\delta\nu} = 2\,\text{ps}. \tag{5.1}$$

| $\tilde{\nu}$ / cm$^{-1}$ | $\Delta\tilde{\nu}$ / cm$^{-1}$ | $\lambda_c$ / Å | $\Delta\lambda$ / Å | $\sigma_{\mathrm{rel}}$ | $f_\nu \times 10^{-2}$ |
|---|---|---|---|---|---|
| 10378.5 | 2.4 | 9632.7 | 2.2 | 0.89 | 1.28 |
| 10438.1 | 2.7 | 9577.6 | 2.5 | 1.00 | 1.62 |
| 10603.2 | 2.7 | 9428.5 | 2.4 | 0.33 | 0.54 |
| 10674.2 | 2.8 | 9365.9 | 2.4 | 0.24 | 0.40 |
| 10693.3 | 2.7 | 9349.1 | 2.3 | 0.07 | 0.11 |
| 10796.6 | 2.4 | 9259.7 | 2.1 | 0.02 | 0.03 |
| 10803.4 | 2.3 | 9253.8 | 2.0 | 0.01 | 0.01 |
| 10839.9 | 2.4 | 9222.7 | 2.0 | 0.02 | 0.03 |
| 10844.9 | 2.5 | 9218.4 | 2.1 | $*$ | - |
| 10851.7 | 2.1 | 9212.6 | 1.8 | 0.02 | 0.03 |
| 10866.0 | 3.2 | 9200.5 | 2.7 | 0.03 | 0.06 |
| 10881.5 | 2.0 | 9187.4 | 1.7 | $*$ | - |
| 10905.0 | 2.3 | 9167.6 | 1.9 | $*$ | - |
| 10907.5 | 1.4 | 9165.5 | 1.1 | $*$ | - |
| 10915.3 | 2.0 | 9159.4 | 1.7 | $*$ | - |
| 10919.9 | 2.1 | 9155.1 | 1.8 | 0.01 | 0.01 |
| 10926.5 | 1.7 | 9150.3 | 2.0 | 0.01 | 0.01 |
| 10934.2 | 2.9 | 9143.1 | 2.4 | $*$ | - |
| 10937.7 | 2.3 | 9140.2 | 1.9 | 0.01 | 0.01 |
| 10952.2 | 3.1 | 9128.0 | 2.6 | 0.01 | 0.02 |
| 10958.2 | 0.6 | 9123.1 | 0.5 | $*$ | - |
| 10963.5 | 2.5 | 9118.7 | 2.1 | 0.02 | 0.03 |
| 10969.6 | 1.6 | 9113.5 | 1.3 | $*$ | - |
| 10974.2 | 1.2 | 9109.8 | 1.0 | $*$ | - |
| 10989.6 | 2.5 | 9097.1 | 2.2 | 0.01 | 0.02 |
| 10995.0 | 4.0 | 9092.5 | 3.4 | $*$ | - |
| 11000.0 | 1.6 | 9088.4 | 1.4 | $*$ | - |
| 11005.9 | 2.6 | 9084.3 | 2.1 | 0.01 | 0.02 |
| 11008.4 | 2.3 | 9081.4 | 1.9 | $*$ | - |
| 11022.9 | 4.0 | 9069.5 | 3.2 | $*$ | - |

Table 5.5: Wavenumbers and air wavelength of the band maxima and their corresponding FWHMs obtained from Gaussian fits. $*$ indicates relative cross-sections $< 0.01$. Uncertainties for the first five bands are given with $\pm 0.1$ cm$^{-1}$ in frequency and $\pm 0.2$ cm$^{-1}$ in widths. Others have $\pm 0.2$ cm$^{-1}$ in frequency and 20 % in widths. Uncertainties for cross-sections have to be considered with 35 %.

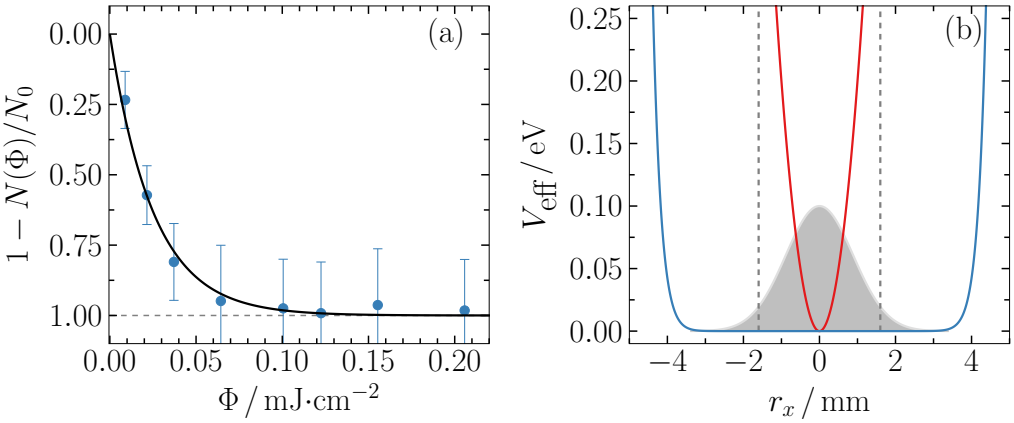


Figure 5.3: (a) Fragmentation of $C_{60}^+$ –He at 9632.5 Å as a function of laser fluence. Experimental data (●) were obtained by monitoring the number of ions as a function of laser fluence, $N(\Phi)$. The exponential fit (–) provides characteristic fluence $\Phi_0$. The data have been corrected for the background ions appearing at $m/z = 724$. (b) Effective potentials for 22-pole (–) and the 4-pole trap (–) for the parameters: $V_0 = 150\,\text{V}$, $m/z = 724$, $r_0 = 5\,\text{mm}$ $f_{22} = 5\,\text{MHz}$, $f_4 = 780\,\text{kHz}$. The dashed lines (--) indicate the boundaries of the bender electrode, that limits the size of the beam profile (■).

The spectrum in the upper trace of Figure 5.2 shows the region between 11 000 and 10 790 $\text{cm}^{-1}$ and was recorded with an increased fluence. It reveals a complicated pattern of transitions with relative intensities below 3%.Probing the ions in the non-linear regime will lead to a broadening of the bands. Thus, the listed values in Table 5.5 are corrected using equation (2.60).

An absolute absorption cross-section $\sigma$ can be determined under the assumption that a single photon ultimately leads to fragmentation of the complex [9]. A typical measurement of the attenuation as a function of the laser fluence for the 10 378 $\text{cm}^{-1}$ band is shown in Figure 5.3. Results obtained from 22-pole trap measurements differ by almost two orders of magnitude compared to the 4-pole trap (Table 5.6). The reason for this is found in the different effective potentials and the constructions of the two traps and the bender. An illustration of the circumstances is shown Figure 5.3 (b). In case of a 22-pole trap, laser radiation does not interact with the full ion cloud. The beam has to pass the bender electrode which has a diameter of 3.2 mm and any broader beam profile will be reduced to an approximate FWHM of $\sim 1.6\,\text{mm}$. This is smaller than the radial cross-section of the ion cloud with a diameter of $\sim 3.5\,\text{mm}$. The problem would still be persistent if this electrode is replaced. In the current construction the end cap electrodes

| $n$-Trap | $r_c$ / mm | $\tilde{\nu}$ / cm$^{-1}$ | profile | $\Phi_0$ / mJ·cm$^{-2}$ | $\sigma_{abs}$ / cm$^2$ | ratio |
|---|---|---|---|---|---|---|
| 4 | 0.18 | 10378 | FT | $5.2 \times 10^{-2}$ | $4 \times 10^{-15}$ | 0.8 |
| 4 | 0.18 | 10438 | FT | $4.8 \times 10^{-2}$ | $5 \times 10^{-15}$ | 1.0 |
| 22 | 0.37 | 10378 | G | $1.4 \times 10^{-3}$ | $7 \times 10^{-17}$ | 0.8 |
| 22 | 0.37 | 10438 | G | $1.1 \times 10^{-3}$ | $9 \times 10^{-17}$ | 1.0 |

Table 5.6: Comparison of the absorption cross-sections for $C_{60}^+$–He obtained from measurements using the 4-pole and 22-pole trap for a G=Gaussian and FT=Flat-Top beam profile.

of the 22-pole trap are also smaller and cannot be enlarged. A fraction of the complexes is not permanently irradiated with the same power density, especially if patch potentials prevent the interaction with photons at all. Consequently, the 22-pole measurements can only provide relative cross-sections.

Absolute values are extracted from the 4-pole measurements. A Flat-Top beam profile covers the whole ion cloud with a nearly constant power density. The derived characteristic fluence $\Phi_0$ from the exponential fit in Figure 5.3 (a) can be directly converted using equation (2.49) into an absolute cross-section $\sigma$. For the two distinct transitions they are determined to

$$\sigma(10\,379) = (4 \pm 2) \cdot 10^{-15}\ \text{cm}^2 \tag{5.2}$$

$$\sigma(10\,438) = (5 \pm 2) \cdot 10^{-15}\ \text{cm}^2 \tag{5.3}$$

A large uncertainty has to be given, because several systematic sources of errors have to be accounted for in this measurement. The largest contribution arises from the effective power density. The bender electrode acts as an iris and provides a nearly constant power density over the ion cloud (Figure 3.12). On the other hand, a slight shift of 3 mm in the laser beam leads to a different interference pattern and reduces the cross-section by 20 %. Mechanical accuracy of the shutter caused fluctuations in the irradiation time of up to 2 ms and contributes with another 20 %. The setting of the wavelength to the band maximum can introduce an error of almost 10 %. Further uncertainties that have to be accounted for are the determination of the $^{12}C_{56}{}^{13}C_4$ background and the overlap of the ion cloud with the laser beam (Figure 3.13), leading to errors of 10 % each. Contributions of other errors, e.g. statistical error, are much smaller and can be neglected. The uncertainty for the cross-section is then estimated to $\delta\sigma = 35\,\%$. A very important factor is the possibility of a re-growth of the complexes during the irradiation times of typically 10 to 40 ms. Measurements have shown that several 100 ms

of evacuation of buffer gas are necessary to reduce the collision rate such that competing complex formation is negligible.

### 5.1.2 $C_{60}^+$–$n$He

The spectrum obtained from the tagged cation is assumed to have small deviations in wavelength compared to that of $C_{60}^+$. In order to estimate this shift, spectra in the region of the two strongest absorption bands were recorded with 2 He and 3 He attached at 3.7 K and the results are shown in Figure 5.4. The spectra are well-represented by a Lorentzian and Gaussian function. Deviations in the central wavelengths are $< 0.2\,\mathrm{cm}^{-1}$ slightly more pronounced for the $10\,378\,\mathrm{cm}^{-1}$. In addition, the bands show differences in their FWHMs, compared to $C_{60}^+$–He they increased by $\sim 0.5\,\mathrm{cm}^{-1}$ in case of $C_{60}^+$–3He.

Band maxima obtained from the $C_{60}^+$–$n$He spectra are plotted as a function of $n$ in Figure 5.5. A linear extrapolation of the data can provide an uncertainty range due to the perturbation of the messenger. The slopes yield shifts of $0.7\,\mathrm{cm}^{-1}$ per He, resulting in band maxima for $C_{60}^+$ at $(10379.2 \pm 0.2)$ cm$^{-1}$ and $(10438.7 \pm 0.2)$ cm$^{-1}$. This is consistent with recent results of $C_{60}^+$ in 0.37 K helium nanodroplets. A shift of $\sim$0.7 Å per helium was reported for the $10438\,\mathrm{cm}^{-1}$ band by extrapolating the band maxima frequencies as a function of $n$He, for $n$ = 5-32 [10]. The intercept at $n = 0$ is not given.

The central wavelengths for $n > 1$ are very sensitive to the experimental conditions. For example, the spectrum of $C_{60}^+$–2He at 3.7 K yields a value of $10437.4\,\mathrm{cm}^{-1}$ compared to $10438.0\,\mathrm{cm}^{-1}$ at 5 K, which is shown in Figure 5.6. For the high temperature measurements a stronger laser fluence was chosen to improve the signal-to-noise ratio, because of the lower complex formation rates for $n > 1$. The 10 379 absorption band reveals an asymmetric band shape indicating a substructure caused by the rotational profile or two absorption bands. At temperatures below 4 K $^4$He condensates on the trap walls leading to complex formation via bimolecular reactions between ions and He-clusters rather than ternary association processes. The different formation mechanism may result in a different isomer. Simulations predict similar binding energies for He on the pentagonal and the hexagonal sites of $C_{60}^+$ with the latter favored by only 1.3 meV. A doubtless conclusion requires the gas-phase spectrum of the unperturbed $C_{60}^+$. Another possibility would be the use of $^3$He for complex formation as the boiling point is 1 K lower compared to $^4$He. The low natural abundance and the extensive demand as fusion fuel for this

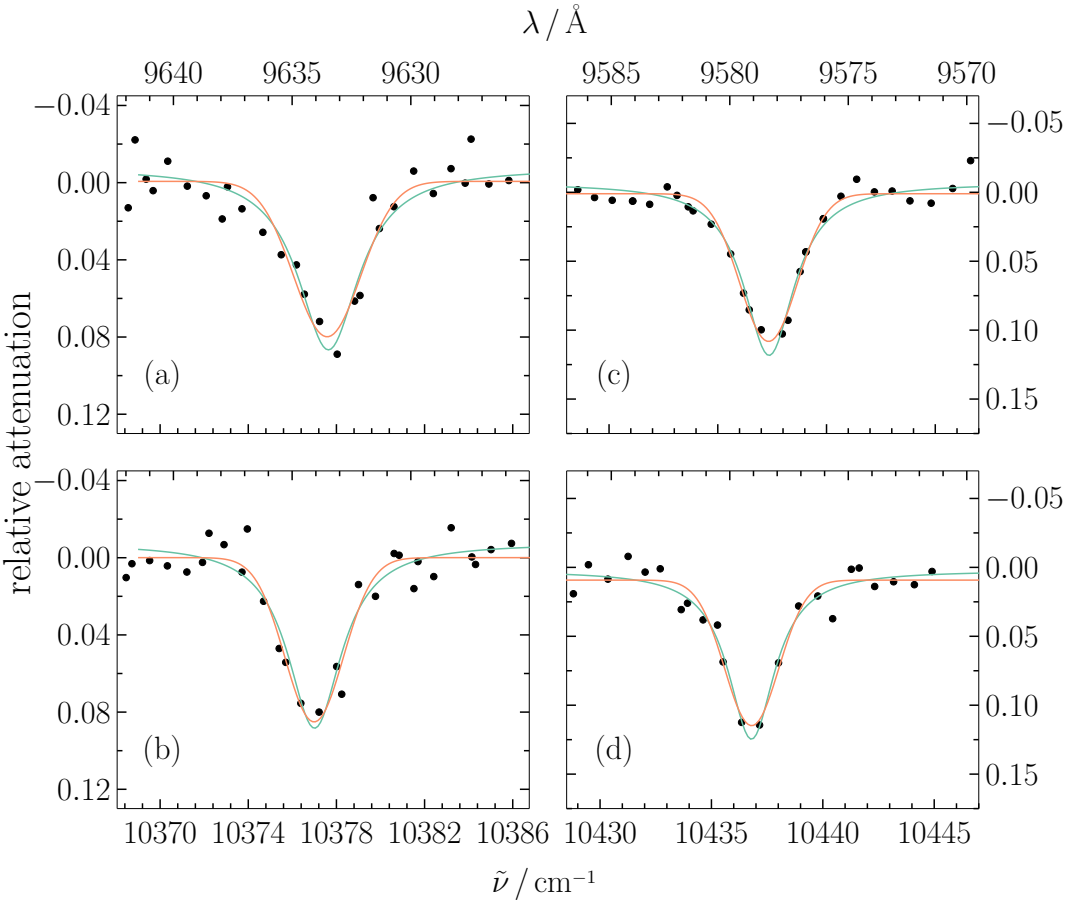


Figure 5.4: 9577 Å and 9632 Å absorption bands of $C_{60}^+$–2He (a,c) and $C_{60}^+$–3He (b,d) at $T_{\mathrm{nom}} = 3.7\,\mathrm{K}$. Experimental data (•) are fit with Gaussian (–) and Lorentzian (–) functions.

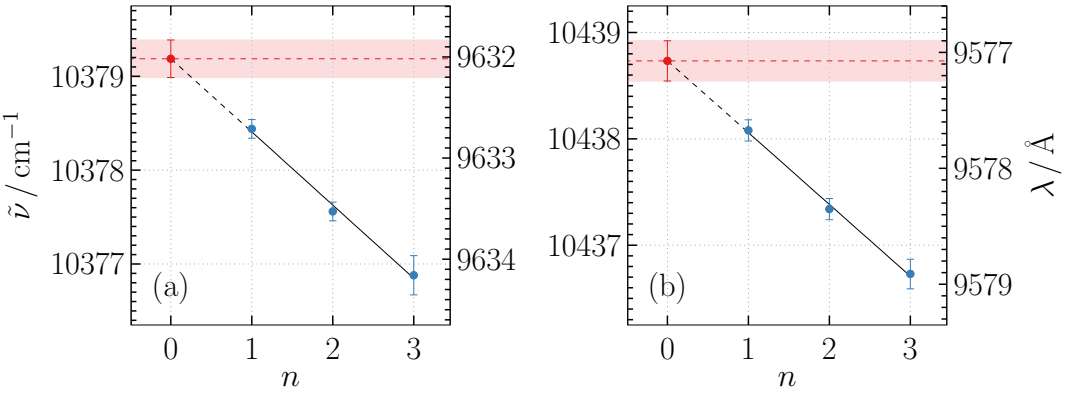


Figure 5.5: Linear fits (–) to the central wavelengths (•) of the $C_{60}^+$–$n$He ($n = 1, 2, 3$) for the two absorption bands at $10\,379\,\mathrm{cm}^{-1}$(a) and $10\,438\,\mathrm{cm}^{-1}$(b), respectively. The experimental data are averaged values with standard deviations. The black dashed line indicates the extrapolation to the wavelength for $n = 0$ (•). The error bars are estimated for a confidence interval of 95%.

isotope is to date not affordable [11]. However, the uncertainty of the absolute band maxima could be narrowed down and allows a confident comparison with astronomical data.

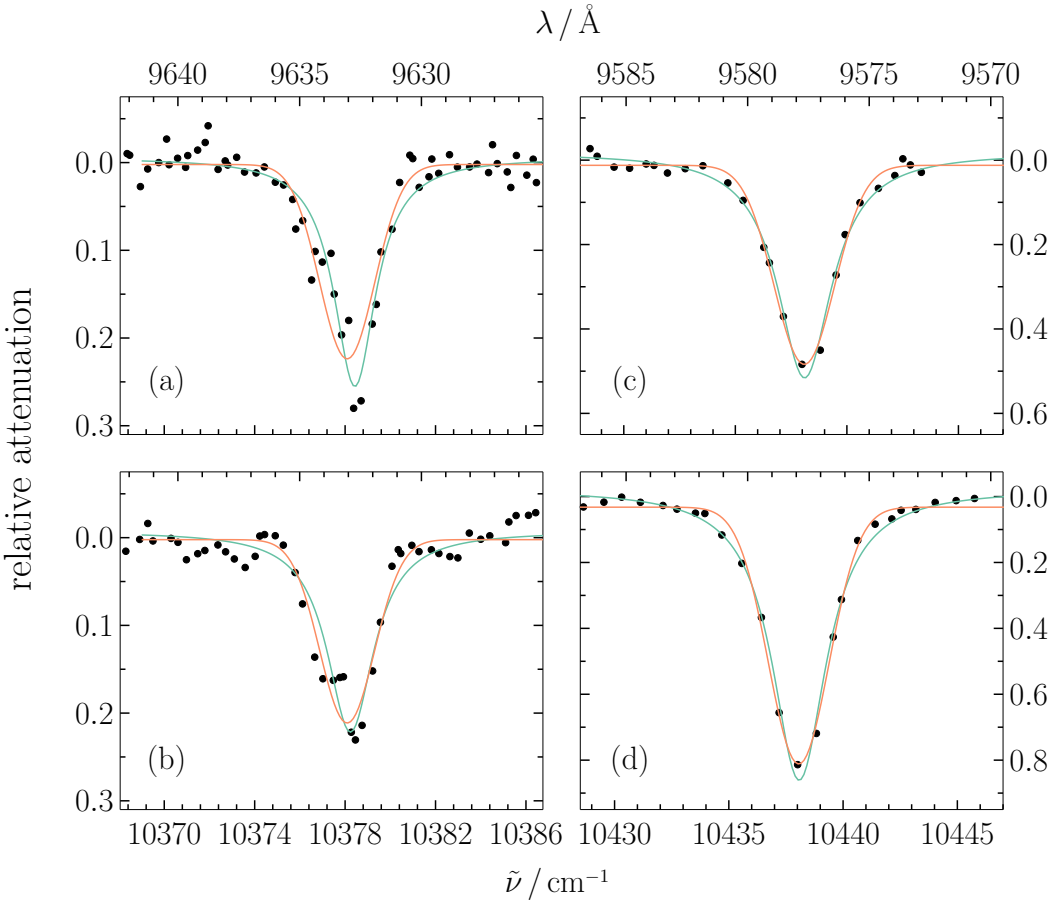


Figure 5.6: 9577 Å and 9632 Å absorption bands of $C_{60}^+$–He (a,c) and $C_{60}^+$–2He (b,d) at $T_{\mathrm{nom}} = 5.0\,\mathrm{K}$. Experimental data (•) are fit with Gaussian (–) and Lorentzian (–) functions.

### 5.1.3 Comparison to the DIBs

Several studies confirming the presence of two DIBs near 9577 Å and 9632 Å toward different lines-of-sight have been published. A majority of these give wavelengths without any error bars and some report only integer values. Furthermore, average values of the wavelengths are provided for observations toward different stars but individual values for other parameters (FWHM, equivalent width) are listed. A summary of available data for central wavelengths, FWHMs, and ratios of their equivalent widths (EW) can be found in Appendix B.

The deviation in the reported wavelengths of the two NIR DIBs is of about 1.9 Å and 1.3 Å for the 9632 Å and 9577 Å bands, respectively. The laboratory results for $C_{60}^+$–He and the inferred values of bare $C_{60}^+$ lie within this range for both absorption bands. Extraction of an accurate wavelength for the 9632 DIB appears more complicated because of the overlap of the MgII stellar lines at 9322.44 and 9631.89 Å [4, 12]. In addition, a continuum level setting needs to be estimated and the spectra have to be corrected for telluric absorption lines, mainly from water vapor in this region. Together with systematic errors from the detector it seems to be difficult to provide uncertainties for the parameters obtained from astronomical observations. The mean values of the wavelengths from all studies are (9577.0±0.3) Å and (9632.0 ± 0.4) Å, where the errors are the standard deviations. These are similar to the results of the the experimental wavelengths of 9632.1 Å and 9577.0 Å for $C_{60}^+$ obtained from the extrapolated data (Figure 5.5).

Reported FWHMs range from 2.3-5.4 Å for the DIB at 9577 Å and 2.0-4.5 Å for the DIB at 9632 Å. The widths are convolutions of instrumental resolution, velocity dispersion of the line-of-sight and the rotational envelope [15]. A Doppler broadening can usually be corrected by reference measurements of known stellar lines. The mean values for the 9632 and 9577 DIBs are 3.2±1.0 Å and 3.6±1.0 Å, respectively, and these are close to those obtained in laboratory spectrum of $C_{60}^+$–He. As discussed earlier, at temperatures below 30 K, the FWHM of ∼2.5 Å is determined by the lifetime of the excited electronic state. An increase in the FWHM from this value indicates temperatures higher than 30 K in the local environment as they are expected for diffuse clouds [16].

A comparison of the EWs for the two bands provides information of their relative intensities. The ratio of the EW has a rather large distribution, and spans the range from 0.8 to 1.6. It also appears to be strongly dependent on the reference

| Laboratory | | | | Interstellar | | |
|---|---|---|---|---|---|---|
| $C_{60}^+$–He | | | $C_{60}^+$ | | | |
| $\lambda_c$ / Å | $\Delta\lambda$ / Å | $\sigma_{rel}$ | $\lambda_c$ / Å | $\lambda_c$ / Å | $\Delta\lambda$ / Å | $\frac{W_{\lambda_c}}{W_{9577}}$ |
| $9632.7 \pm 0.1$ | $2.2 \pm 0.2$ | 0.80 | $9632.1 \pm 0.2$ | $9632.2 \pm 0.4$ | $3.5 \pm 0.9$ | 0.83 |
| $9577.6 \pm 0.1$ | $2.5 \pm 0.2$ | 1.00 | $9577.0 \pm 0.2$ | $9577.0 \pm 0.3$ | $3.2 \pm 0.7$ | 1.00 |
| $9428.5 \pm 0.1$ | $2.4 \pm 0.2$ | 0.33 | $9427.8 \pm 0.2$ | $9428.4 \pm 0.1$ | $3.2 \pm 0.1$ | 0.27 |
| $9365.9 \pm 0.1$ | $2.4 \pm 0.2$ | 0.24 | $9365.2 \pm 0.2$ | $9365.7 \pm 0.1$ | $2.5 \pm 0.1$ | 0.16 |
| $9349.1 \pm 0.1$ | $2.3 \pm 0.2$ | 0.07 | $9348.4 \pm 0.2$ | $9348.5 \pm 0.1$ | $1.4 \pm 0.2$ | 0.05 |

Table 5.7: Summary of the results from laboratory and astronomical observations. Experimental values are given for $C_{60}^+$–He at 5 K and the central wavelengths extrapolated to $C_{60}^+$. Relative intensities have uncertainties of 20%. The astronomical data are provided as mean values. For the ratios the MgII corrected values for $W_{9632}$ have been used. A full list can be found in the Appendix B. Values for DIBs 9249, 9366, and 9349 are from Ref. [13, 14].

star used for the telluric corrections [17, 18]. The mean ratio is obtained to be $1.0 \pm 0.2$ without corrections and $0.8 \pm 0.2$ with extracting the contribution of the overlapping MgII line. This is consistent with the experimentally estimated relative intensity of $0.8 \pm 0.2$.

The next three bands toward shorter wavelengths in the (corrected) laboratory spectrum are at 9428.5 Å, 9365.9 Å, and 9349.1 Å. Their absorption cross-sections are weaker by a factor of 4-5 than the two strong absorption bands. Also these three absorption bands have been observed with similar characteristics in band positions, FWHMs and relative intensities [13, 14].

The five discussed laboratory and experimental absorption bands are shown in Figure 5.7 and summarized in Table 5.7. The agreement of the necessary characteristics is compelling, especially if the extrapolated central wavelengths are considered. By continuing the laboratory and astronomical data, an estimate for the interstellar abundance of $C_{60}^+$ is inferred. A column density $N$ relies on the knowledge of the oscillator strength $f_\nu$, the absorption band maximum $\lambda_c$ and the EW $W_\lambda$ [19]. For the 9577 DIB using the averaged values obtained for HD 183143 the

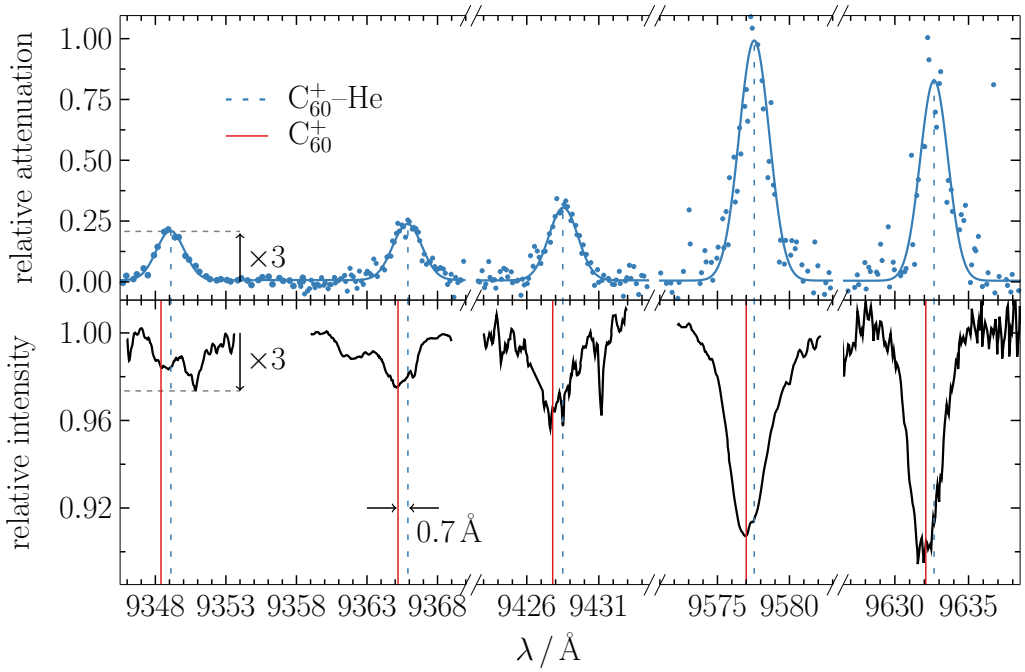


Figure 5.7: Comparison of the laboratory (●, upper trace) to the astronomical (━, lower trace) data. The blue curves (━) are Gaussian fits to the experimental absorption bands. The region around 9349 Å has been enlarged in both spectra by a factor 3. Central wavelengths for $C_{60}^+$–He (╌) and the extrapolated $C_{60}^+$ (━) are shown to indicate experimental uncertainties. The astronomical spectrum is reproduced from observations toward HD 169454 in the region of the 9429 Å band and HD 183143 in case of the other bands [13–15].

column density can be calculated to

$$N = 1.13 \times 10^{20} \cdot \frac{W_\lambda}{\lambda^2 f_\nu} \tag{5.4}$$

$$= 1.13 \times 10^{17} \cdot \frac{267\,\text{mÅ}}{(9577.2\,\text{Å})^2 \cdot 0.0162} \tag{5.5}$$

$$= (2 \pm 1) \times 10^{13}\,\text{cm}^{-2}. \tag{5.6}$$

The error is estimated from the standard deviations. This column density is an order of magnitude smaller than that of $H_3^+$ but is comparable to $CH^+$. Both molecules were also observed toward HD 183143 [20]. An estimate for the fraction $\chi$ of the total interstellar carbon locked up in $C_{60}^+$ can be derived with an empirical relation given by [21, 22]

$$\frac{W_\lambda}{E_{B-V}} = 10 \cdot \left(\frac{\chi}{A \times 10^{-4}}\right) \left(\frac{60}{N_\text{C}}\right) \left(\frac{\lambda}{5500}\right)^2 \left(\frac{f_\nu}{10^{-2}}\right). \tag{5.7}$$

The value for $A$ differs depending on the assumed amount of cosmic carbon with respect to atomic hydrogen in the interstellar gas, while $N_{\mathrm{C}}$ is the number of carbon atoms. Considering only the two strong bands with their averaged values of $W/E_{B-V} = 350\,\mathrm{m\AA/mag}$ toward several lines-of-sight and $N_{\mathrm{C}}/N_{\mathrm{H}} = 4 \times 10^{-4}$, then

$$\chi = (4 \pm 3) \times 10^{-4} = 0.04\,\%. \tag{5.8}$$

This is only a rough estimate, because of the large deviation in the EWs. However, it reflects the significant relevance of $C_{60}^+$ in the interstellar medium and provides an upper limit for other fullerenes.

### 5.1.4 $C_{60}^+$–$L$ ($L$ =Ne, Ar, Kr, $H_2$, $D_2$, $N_2$)

The effects of He attached to $C_{60}^+$ allowed estimations of the band maxima for $C_{60}$. In order to obtain further insights on the influence of weakly bound complexes, several rare-gas atoms and molecules with higher polarizabilities have been physisorbed to $C_{60}^+$ and are discussed in the context of their electronic spectra. To ensure ion-complex formation, the temperature was increased as a diagnostic for the formation process. Typically above 15 K only $C_{60}^+$ can be detected indicating low binding energies. The internal energy of $C_{60}^+$ is still relaxed via buffer gas cooling with He. To avoid the competing formation of $C_{60}^+$–He, complexes are then formed at an elevated wall temperature of $\sim 6\,\mathrm{K}$.

#### $C_{60}^+$–rare-gas spectra

Photofragmentation spectra of $C_{60}^+$–Rg (Rg= Ne, Ar, Kr) at $T_{\mathrm{nom}} = 5.7\,\mathrm{K}$ are shown in Figure 5.8. The absorption bands have been fit with Lorentzian profiles and the obtained parameters are given in Table 5.8.

The $C_{60}^+$–He spectrum is characterized by two distinct absorption bands at $\tilde{\nu}_a = 10\,378.5\,\mathrm{cm^{-1}}$ and $\tilde{\nu}_b = 10\,438.1\,\mathrm{cm^{-1}}$. The attachment of heavier atoms leads to small changes in the frequency of $\tilde{\nu}_b$. For argon and neon shifts of $+0.4\,\mathrm{cm^{-1}}$ and $+0.5\,\mathrm{cm^{-1}}$ are observed, while in the case of krypton the band frequency is almost identical with the one for helium.

In contrast the region of the $\tilde{\nu}_a$ band is more sensitive to the tagged atom. The $C_{60}^+$–Ne spectrum shows a doublet with band maxima at $10\,376.8\,\mathrm{cm^{-1}}$ and $10\,379.0\,\mathrm{cm^{-1}}$. These features are labeled as $\tilde{\nu}_{a'}$ and $\tilde{\nu}_a$ in the following. For argon a splitting of $12.8\,\mathrm{cm^{-1}}$ is observed, and the trend of increasing separation with mass continues to

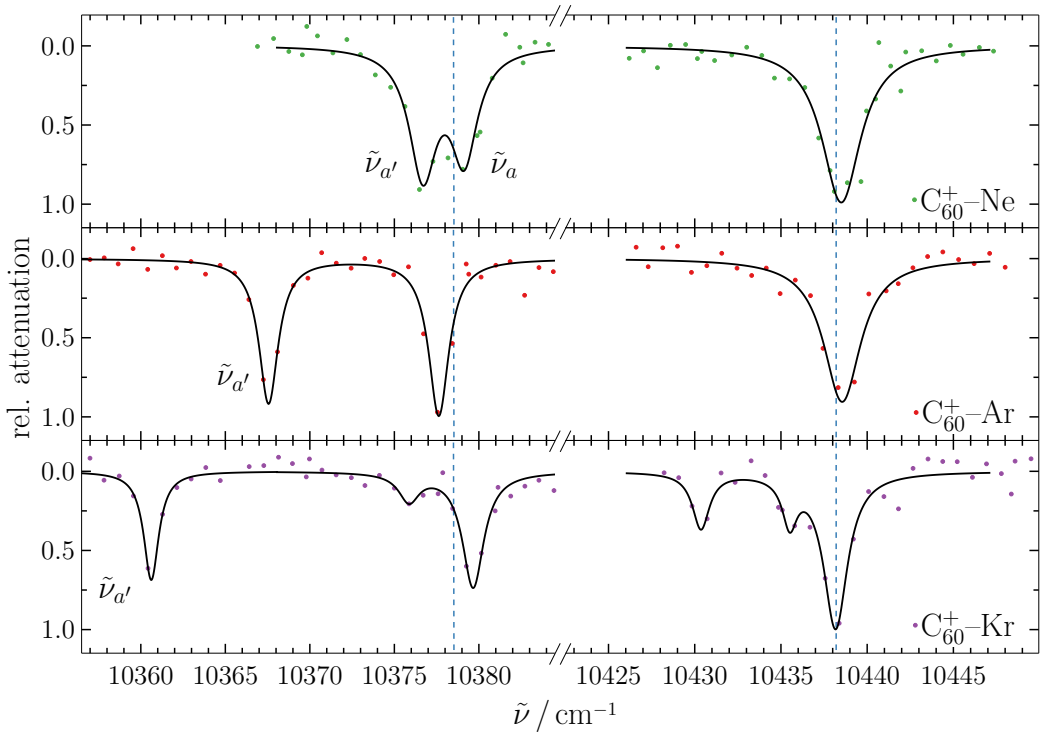


Figure 5.8: Electronic spectra of $C_{60}^+$–$L$, with $L$ = He, Ne, Ar, Kr. Experimental data (dots) have been fit with a Lorentzian profile (**–**). The spectrum of $C_{60}^+$–He has been obtained at $T_{\mathrm{nom}} = 4\,\mathrm{K}$, the others at $T_{\mathrm{nom}} = 5.7\,\mathrm{K}$. The dashed vertical lines (**--**) indicate the $C_{60}^+$–He band maxima.

krypton with $19\,\mathrm{cm}^{-1}$. Additional weak transitions at $10\,375.9\,\mathrm{cm}^{-1}$, $10\,430.4\,\mathrm{cm}^{-1}$ and $10\,435.5\,\mathrm{cm}^{-1}$ are measured in the $C_{60}^+$–Kr spectrum.

### $C_{60}^+$–diatomics

Similar but more pronounced effects are noticed in the spectra of physisorbed diatomic molecules to $C_{60}^+$ (Figure 5.9, Table 5.8). The absorption $\tilde{\nu}_{a'}$ is observed for $H_2$ at $10\,366.7\,\mathrm{cm}^{-1}$, $D_2$ at $10\,364.0\,\mathrm{cm}^{-1}$ and at $10\,357.2\,\mathrm{cm}^{-1}$ in the case of $C_{60}^+$–$N_2$. For the latter $\tilde{\nu}_a$ is also redshifted relative to the frequency in the spectrum of $C_{60}^+$–He by $-1.9\,\mathrm{cm}^{-1}$, those for $H_2$ and $D_2$ are akin with $-2.2\,\mathrm{cm}^{-1}$ and $-2.7\,\mathrm{cm}^{-1}$, respectively.

Larger displacements of the frequencies of $\tilde{\nu}_b$ relative to the $C_{60}^+$–He spectrum are found in comparison to the rare-gas complexes. The bands are redshifted for $H_2$ to $10\,436.0\,\mathrm{cm}^{-1}$ and for $D_2$ to $10\,435.1\,\mathrm{cm}^{-1}$. The trend is reversed by a blueshift for $N_2$ to $10\,440.8\,\mathrm{cm}^{-1}$. The spectra of $D_2$ and $N_2$ have weak shoulders at $\tilde{\nu}_b + 3.7\,\mathrm{cm}^{-1}$ and $\tilde{\nu}_b - 3.8\,\mathrm{cm}^{-1}$, respectively.

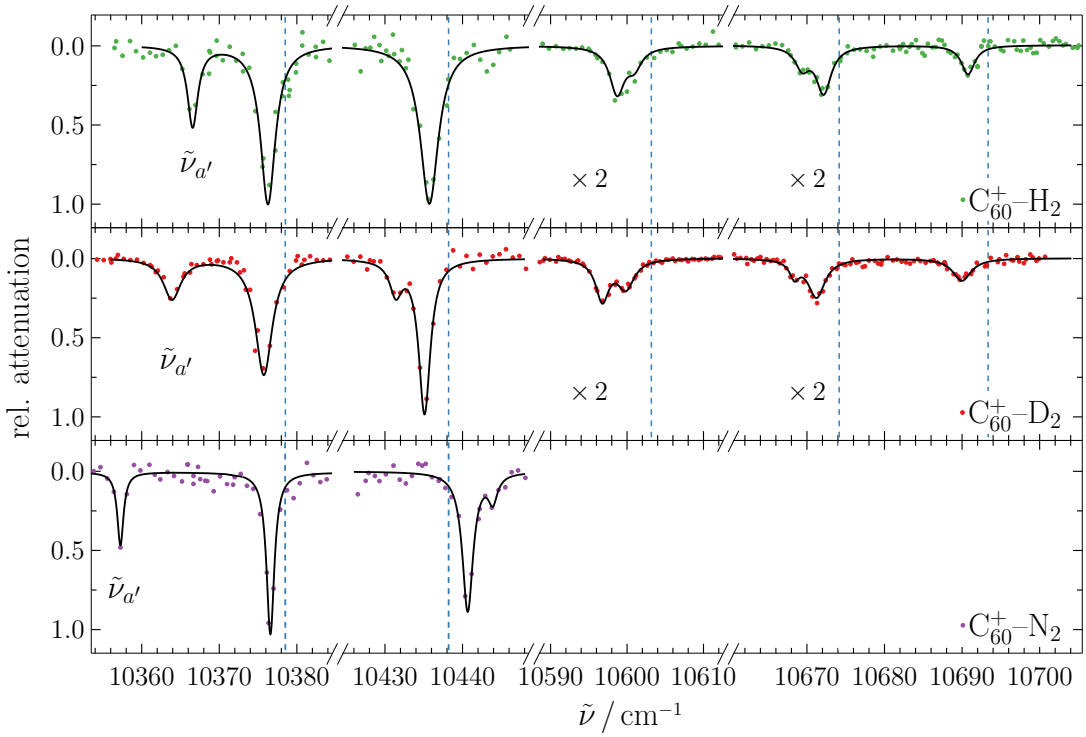


Figure 5.9: Electronic spectra of $C_{60}^+$–$L$, with $L$ = $H_2$, $D_2$, $N_2$ at $T_{\mathrm{nom}}$ = 5.7 K. Experimental data (dots) have been fit with Lorentzian profiles (–). The spectral region between 10 590 and 10 700 cm$^{-1}$ is enlarged by a factor of two.

Measurements of $C_{60}^+$–$H_2$ and $C_{60}^+$–$D_2$ were made toward higher energy where three transitions have been previously observed for $C_{60}^+$–He. Conjointly redshifted, the first two exhibit a doublet structure with separations ranging from 2.3 to 3.2 cm$^{-1}$. The relative intensities are similar in the two spectra but are weaker compared to $C_{60}^+$–He. The doublets have asymmetric intensities. The ratios at $\sim$ 10 600 cm$^{-1}$ are 0.7:1 and 1:0.6 for the doublets at $\sim$ 10 670 cm$^{-1}$ within an uncertainty of 10 %.

The shifts of $\tilde{\nu}_{a'}$, $\tilde{\nu}_a$ and $\tilde{\nu}_b$ relative to the $C_{60}^+$–He bands per reduced mass are larger for the diatomic than for atomic messengers. This suggests a parallel positioning of the internuclear axis of the diatomic molecule to the hexagonal or pentagonal sites of $C_{60}^+$. According to theoretical results for $C_{60}^+$–$H_2$ a perpendicular configuration is energetically less favored by $\sim$ 11 meV [23].

In all measured electronic spectra, the widths of the absorption bands become narrower with increasing mass. A possible explanation is given by treating the complex in a rigid rotor approximation. Assuming only minor changes in the bond

distance of $C_{60}^+$ and the messenger, the moment of inertia becomes larger, resulting in a closer spacing of the rotational energy levels.

### Astronomical Implications

A relevance regarding the DIBs is unlikely, because ionized molecules are more important in HI regions where UV radiation dominates [24]. Only in dense clouds, in which $H_2$ is more abundant and temperatures are lower with 10-50 K, fullerenes could be complexed with molecular hydrogen [16]. The high collision frequency with $H_2$ would exceed the rate of thermal $H_2$ desorption with $10^{-14}\,s^{-1}$, estimated from a simplified Arrhenius relation in nanodroplet experiments [25].

| He | | Ne | | Ar | | Kr | | $H_2$ | | $D_2$ | | $N_2$ | |
|---|---|---|---|---|---|---|---|---|---|---|---|---|---|
| - | - | 10 379.0 | 2.1 | 10 367.6 | 1.4 | 10 360.6 | 1.1 | 10 366.7 | 1.7 | 10 364.0 | 1.9 | 10 357.2 | 1.2 |
| - | - | - | - | - | - | 10 375.9 | 1.5 | - | - | - | - | - | - |
| 10 378.5 | 2.4 | 10 376.8 | 2.1 | 10 377.6 | 1.5 | 10 379.6 | 1.6 | 10 376.3 | 2.2 | 10 375.8 | 2.6 | 10 376.6 | 1.7 |
| - | - | - | - | - | - | 10 430.4 | 1.2 | - | - | - | - | - | - |
| - | - | - | - | - | - | 10 435.5 | 1.0 | 10 431.4 | 1.9 | - | - | - | - |
| 10 438.1 | 2.7 | 10 438.5 | 2.7 | 10 438.6 | 2.2 | 10 438.1 | 2.2 | 10 436.0 | 2.6 | 10 435.1 | 2.4 | 10 440.8 | 1.7 |
| - | - | - | - | - | - | - | - | - | - | 10 431.4 | 1.9 | 10 443.9 | 1.4 |
| - | - | - | - | - | - | - | - | 10 598.7 | 2.4 | 10 597.1 | 1.9 | - | - |
| 10 603.2 | 2.7 | - | - | - | - | - | - | 10 601.0 | 2.4 | 10 600.3 | 2.2 | - | - |
| - | - | - | - | - | - | - | - | 10 669.2 | 1.9 | 10 668.6 | 2.1 | - | - |
| 10 674.2 | 2.8 | - | - | - | - | - | - | 10 672.1 | 2.3 | 10 671.5 | 2.2 | - | - |
| 10 693.3 | 2.7 | - | - | - | - | - | - | 10 690.7 | 2.4 | 10 689.7 | 2.4 | - | - |

Table 5.8: Wavenumbers and full widths at half maxima in $cm^{-1}$ observed in the $C_{60}^+$–$L$ spectra. Uncertainties are $\pm 0.4\,cm^{-1}$ for the widths and $\pm 0.2\,cm^{-1}$ for the band maxima.

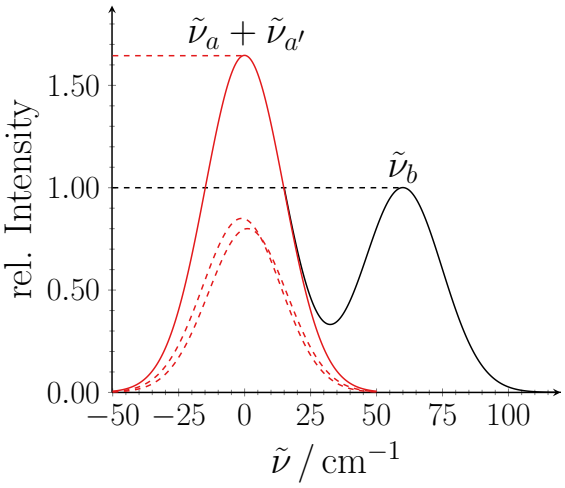


Figure 5.10: Simulation of the neon matrix spectrum (**–**) seen in Ref. [5]. Relative intensities of the $\tilde{\nu}_a$ - $\tilde{\nu}_{a'}$ doublet (**--**) and $\tilde{\nu}_b$ are set corresponding to the results in Figure 5.8. The widths are 35 cm$^{-1}$ in accordance with the neon matrix data.

### Neon Matrix vs. Gas-Phase Intensities

Relative intensities of the two bands $\tilde{\nu}_a$ and $\tilde{\nu}_b$ are different in the neon matrix spectrum compared to the gas-phase spectrum of $C_{60}^+$–He [5, 26]. The ratio in case of the 5 K neon matrix is around 1.6:1. The gas-phase experiment at a similar temperature yields 0.8:1 with an uncertainty of 20 %.

As discussed in the preceding paragraph, the origin band of the Ne complex is split into two 2.1 cm$^{-1}$ broad components that are separated by $\tilde{\nu}_{a'} - \tilde{\nu}_a = 2.2\,\text{cm}^{-1}$. Electronic spectra obtained from matrix isolation spectroscopy are much broader and estimated to be $\approx 35\,\text{cm}^{-1}$.

A simulated spectrum using Gaussian profiles for $\tilde{\nu}_a$, $\tilde{\nu}_{a'}$ and $\tilde{\nu}_b$ is shown Figure 5.10. The relative intensities of the bands are 0.85:0.80:1 according to the results presented in Figure 5.8. A broadening of the $\tilde{\nu}_a$, $\tilde{\nu}_{a'}$ doublet leads to a superposition into a single absorption with a relative intensity 1.6 times larger than $\tilde{\nu}_b$. This is similar to the matrix result. Moreover, two and three neon atoms attached to $C_{60}^+$ lead to shifts of $\tilde{\nu}_{a'}$, $\tilde{\nu}_a$ and $\tilde{\nu}_b$ toward lower energies and an increase in their widths. A comparison between a matrix isolation and a gas phase-experiment is limited; however, the gas phase observations of $C_{60}^+$–Ne allow a rationalization of the relative intensities of the absorptions of $C_{60}^+$ embedded in a neon matrix.

**Implications on the electronic structure of $C_{60}^+$**

The energy differences between the three near infrared bands $\tilde{\nu}_{a'}$, $\tilde{\nu}_a$ and $\tilde{\nu}_b$ do not correspond to rotational or vibrational modes. In the case of $C_{60}^+$–He, irradiation of the two latter transitions leads to complete attenuation in the number of complexes (Figure 5.3). This indicates that the two transitions arise from a single structural isomer. Furthermore, it can be concluded that both transitions originate from the lowest vibrational state of the electronic ground state $^2A_{1u}$ in the predicted $D_{5d}$ symmetry for $C_{60}^+$ and result in two excited states separated by $59.6\,cm^{-1}$. In the given symmetry and spectral region, only two electronic transitions are dipole allowed from the electronic ground state (Figure 5.1). Therefore, $\tilde{\nu}_{a'}$ originates either from a different electronic state or is the result of a different structural isomer.

In a previous study Langford and Williamson proposed that the electronic state $^2E_{1u}$ is thermally accessible even at cryogenic temperatures. The level spacings are predicted to by $\sim 6\,cm^{-1}$ [27]. In Figure 5.11 the spectra in the region of $\tilde{\nu}_a$ and $\tilde{\nu}_{a'}$ of $C_{60}^+$–Ne at $T_{nom} = 4.0, 8.4$ and $11.4\,K$ are shown. The attenuation of the absorption band at $10\,379\,cm^{-1}$ increases with higher temperature. A Boltzmann analysis of the intensity ratios yields a separation of $4.2\,cm^{-1}$ assuming a two level system where the upper level is twofold degenerate. The internal temperature of $C_{60}^+$ has been approximated by the mass weighted collision temperature assuming a translational temperature of 150 K. Below 4.5 K a deviation from the Boltzmann curve is observed, a possible reason could be the phase transition of $^4$He. Similar measurements have been carried out using $C_{60}^+$–Ar in a range of 4-8 K. However, no significant changes in the relative intensities were observed.

Another scheme has been applied by probing the ions with a fluence above the saturation threshold to observe maximum depletion. If all complexes can be depleted on either transition, the ion cloud would only consist of a single ion ensemble with a common ground state. For $C_{60}^+$–Ne this experiment does not work, because the separation of $\tilde{\nu}_a$ and $\tilde{\nu}_{a'}$ is too narrow. The power broadening would superimpose the two bands into a single one. A larger spacing between the two bands is found for $C_{60}^+$–Ar. Power dependent spectra of this complex are shown in Figure 5.12. At higher fluences, the region between $10\,350$ and $10\,400\,cm^{-1}$ is congested by further absorption bands compared to the spectrum in Figure 5.8. The cross-sections of the additional bands are up to two orders of magnitude weaker than for $\tilde{\nu}_a$ and $\tilde{\nu}_{a'}$. However, in the case of $\tilde{\nu}_{a'}$ a maximum attenuation is reached at $\sim 0.8$ in contrast to $\tilde{\nu}_a$ where all complexes can be depleted. The full attenuation of $\tilde{\nu}_a$

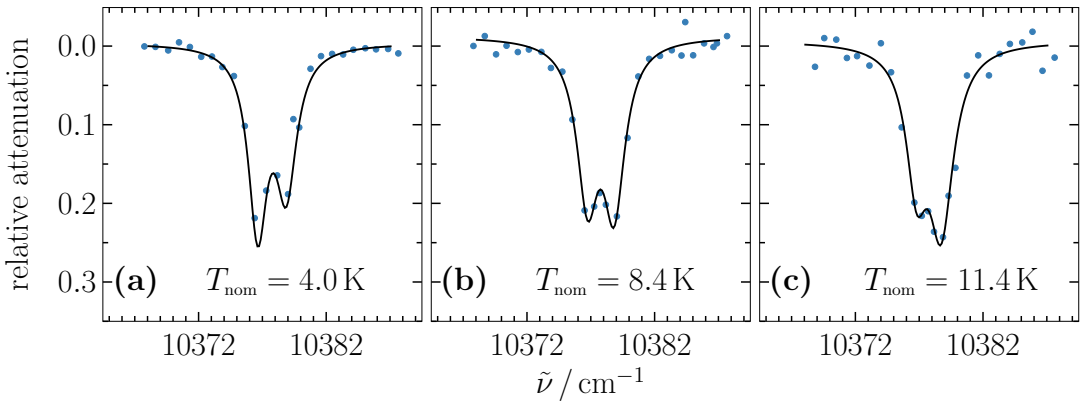


Figure 5.11: Electronic spectra of $C_{60}^{+}$–Ne at nominal temperatures of (a) 4.0 K, (b) 8.4 K and (c) 11.4 K. The laser power was $P = 48\ \mu$W in each. The experimental data (•) have been fit with a Lorentzian profile (**–**).

does not support two different ion ensembles in the trap without an additional mechanism of population exchange. It needs to be emphasized, that the rare gases have been continuously leaked into the trap. Their densities inside the trap are assumed to be $10^{12}$ to $10^{13}\,\mathrm{cm}^{-3}$ at pressures inside the chamber of $\sim 5 \times 10^{-6}$ mbar. Within the irradiation time of 35 ms, Langevin theory predicts 100 to 1000 collisions between the complex and the background gas. Enough to induce excitation and de-excitation processes and a redistribution of the population of multiple ion ensembles.

Further experiments preferably a two-color double resonance excitation could shed insight into this problem. Another possibility would be to modify the experimental setup such that the messenger can be pulsed into the trap and then be evacuated before laser irradiation. In the current setup, condensation effects of the heavier rare gas atoms lead to malfunctions of the piezo valve after a couple of minutes.

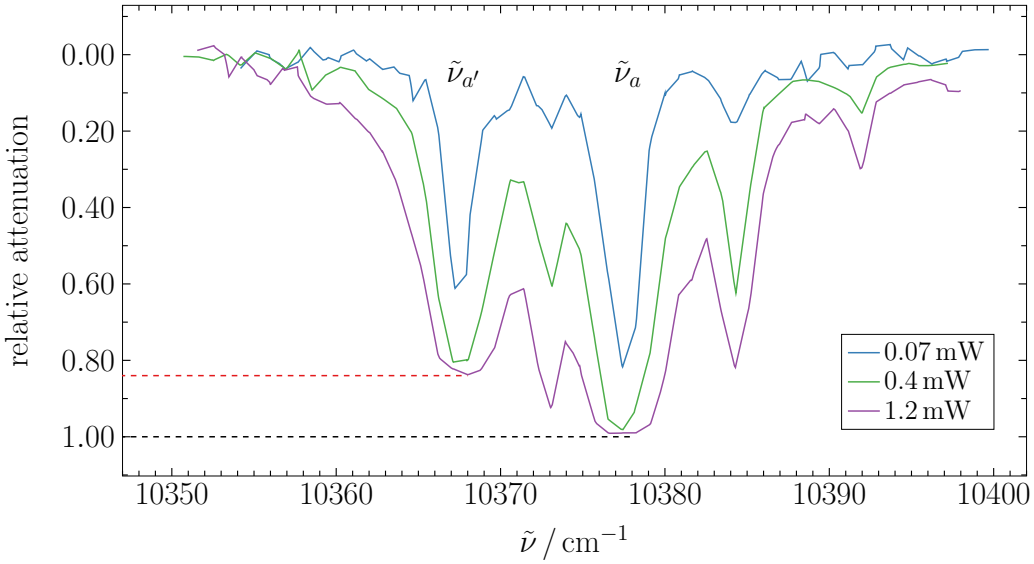


Figure 5.12: $C_{60}^+$–Ar spectra in the region between 10 340 and 10 400 cm$^{-1}$at $P = 1.2, 0.4$, and 0.07 mW. The dashed lines indicate the maximum attenuation for the two absorption bands at 10 368 and 10 379 cm$^{-1}$.

## 5.2 $C_{70}^+$

The identification of $C_{60}^+$ in diffuse interstellar clouds raises the question of the role played by other fullerenes with respect to the DIBs. Not only $C_{60}$ but also $C_{70}$ has been detected in the infrared emission spectrum of a protoplanetary nebula [28] and identified by laser desorption mass spectrometry of samples from the Allende and Murchison meteorites [29]. The ionization potential of $C_{70}$ is with $\sim 8\,\mathrm{eV}$ as low as that of $C_{60}^+$, suggesting that in diffuse clouds it would be in its ionized form [30]. Furthermore, it satisfies the isolated pentagon rule used to explain the high stability of fullerenes suggesting $C_{70}^+$ as a candidate for another carrier of the DIBs.

First spectroscopic measurements of electronic transitions of $C_{70}^+$ have been obtained in a 5 K neon matrix in the region between 12400 and 14000 $\mathrm{cm}^{-1}$ [31]. The spectrum, which has been assigned to the $^2E' \leftarrow {}^2E''$ electronic transition in $D_{5h}$ symmetry, shows several vibronic absorption features with similar absorbance over the covered range. In this region numerous DIBs have been reported [32, 33].

### 5.2.1 $C_{70}^+$–He

The electronic gas-phase spectrum of confined $C_{70}^+$–He in the 4-pole trap, is shown in Figure 5.13. It has been obtained by photofragmentation using the Ti:Sapphire laser with a 3 GHz bandwidth. The individual bands measured in the range between 12500-13500 $\mathrm{cm}^{-1}$have been fit with Gaussian functions giving the wavelengths and FWHMs listed in Table 5.9. The uncertainties are larger than for $C_{60}^+$–He, standard deviations of $\pm 1\,\mathrm{cm}^{-1}$ for the frequencies and 30% for the widths were estimated.

Unlike the absorption spectrum of $C_{60}^+$ , in which the two strong origin bands at 10379 $\mathrm{cm}^{-1}$ and 10438 $\mathrm{cm}^{-1}$ provide a major contribution to the oscillator strength, the system of $C_{70}^+$ consists of many overlapping transitions of roughly equal intensity. The origin band at 12560.6 $\mathrm{cm}^{-1}$ is a factor of 2–3 weaker than the strongest absorption at 13098.1 $\mathrm{cm}^{-1}$. The absorption cross-section at 12560.6 $\mathrm{cm}^{-1}$ is determined to be $(7 \pm 3) \times 10^{-18}\,\mathrm{cm}^2$.

The origin band of $C_{70}^+$–2He was also recorded (Figure 5.14 (a)) to provide information on the perturbation of the electronic transition of $C_{70}^+$ due to the presence of the weakly bound helium atom. A shift of $+0.6\,\mathrm{cm}^{-1}$ from $C_{70}^+$–He to $C_{70}^+$–2He is found at 5 K.

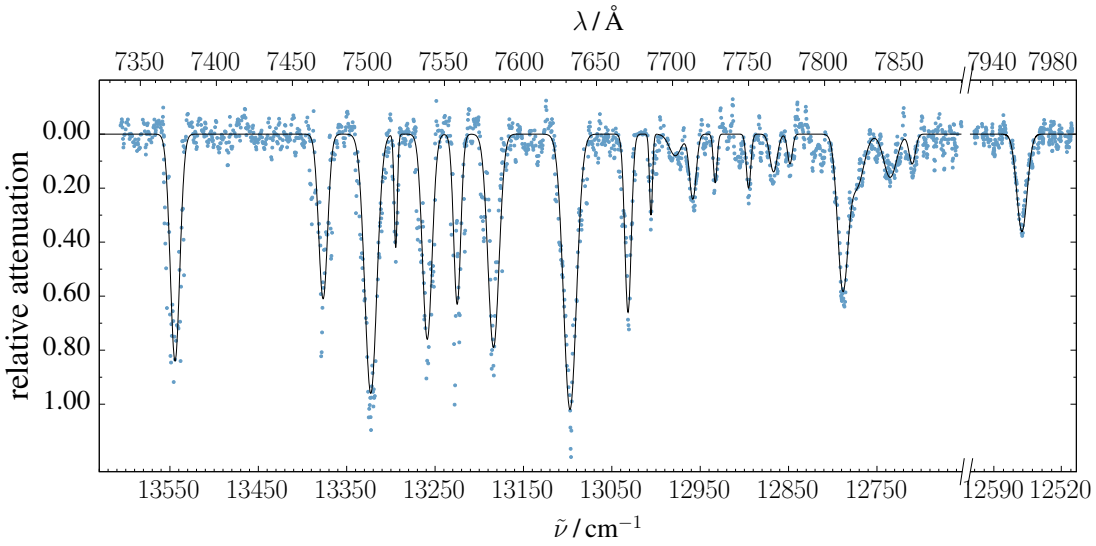


Figure 5.13: Photofragmentation spectrum of $C_{70}^+$–He in the gas phase recorded by monitoring the depletion on the $m/z = 844$ mass channel. Gaussian fits (–) to the experimental data (•) are the solid lines. The intensities of the bands have been scaled by the relative absorption cross-sections.

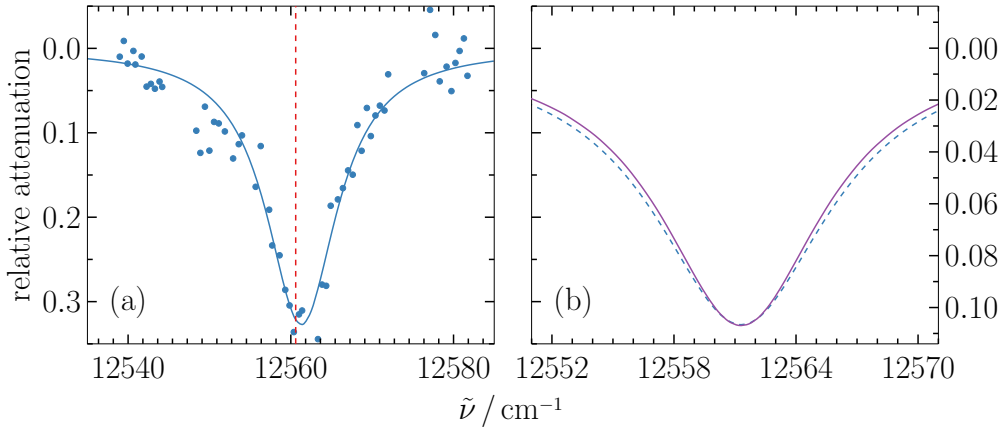


Figure 5.14: (a) Photofragmentation spectrum of the origin band for $C_{70}^+$–2He. Experimental data (•) have been fit using a Lorentzian function (–). The dashed line (--) indicates the band maximum of the corresponding absorption band for $C_{70}^+$–He. (b) Correction (–) of the broadened absorption band in (a).

The FWHMs of $C_{70}^+$–He are significantly broader than for $C_{60}^+$–He and reveal a large spread ranging from $3.7\,cm^{-1}$ to $16.1\,cm^{-1}$. Absorption bands of $C_{70}^+$–He may be partly saturation broadened in addition to their natural width. Only the weaker bands were recorded in the linear regime (attenuation $< 20\%$) A contribution of power broadening can be estimated by using equation (2.60). As shown in Figure 5.14 (b) the FWHM reduces from $10.5\,cm^{-1}$ to $9.5\,cm^{-1}$ indicating a change of $-10\%$. These corrections have been applied to the values listed in Table 5.9. A standard deviation of 30% is estimated as an uncertainty for the FWHMs. The value is obtained from the evaluation of several scans. Assuming that the absorption bands obey a natural linewidth and broadened due to fast internal conversion, the electronic state lifetimes range from 0.5 to 1.4 ps.

### 5.2.2 Comparison to the DIBs

None of the the laboratory bands of $C_{70}^+$ could be matched with the reported bands from astronomical observations, which is not surprising. The neutral fullerene has been identified only in the planetary nebula Tc 1 with an abundance comparable to $C_{60}$ [28]. An estimate for the EW of the strongest transition at $13327\,cm^{-1}$ using equation (5.5) yields $W_{7501} \approx 4\,mÅ$, assuming the same column density derived for $C_{60}^+$. This is close to the reported detection limit at a $3\sigma$ confidence level of 2 mÅ for the spectrograph used with the CFH 3.6 m telescope [14].

| $\tilde{\nu}$ / cm$^{-1}$ | $\Delta\tilde{\nu}$ / cm$^{-1}$ | $\lambda_c$ / Å | $\Delta\lambda$ / Å | $\sigma_{\mathrm{rel}}$ | $f_\nu \times 10^{-3}$ |
|---|---|---|---|---|---|
| 12560.6 | 9.9 | 7959.2 | 6.3 | 0.39 | 0.08 |
| 12723.0 | 7.7 | 7857.6 | 4.8 | 0.12 | 0.02 |
| 12746.6 | 15.4 | 7843.1 | 9.5 | 0.17 | 0.06 |
| 12782.1 | 16.1 | 7821.3 | 9.9 | 0.22 | 0.08 |
| 12797.5 | 12 | 7811.9 | 7.3 | 0.58 | 0.15 |
| 12854.6 | 6.3 | 7777.2 | 3.8 | 0.12 | 0.02 |
| 12872.4 | 9.2 | 7766.4 | 5.6 | 0.15 | 0.03 |
| 12899.7 | 5.7 | 7750.0 | 3.4 | 0.21 | 0.03 |
| 12936.2 | 4.9 | 7728.1 | 2.9 | 0.18 | 0.02 |
| 12961.1 | 8.1 | 7713.3 | 4.8 | 0.24 | 0.04 |
| 12980.2 | 15.7 | 7701.9 | 9.3 | 0.08 | 0.03 |
| 13007.4 | 3.7 | 7685.8 | 2.2 | 0.31 | 0.02 |
| 13033.0 | 7.6 | 7670.7 | 4.5 | 0.68 | 0.11 |
| 13098.1 | 15.4 | 7632.6 | 9.0 | 0.97 | 0.32 |
| 13185.0 | 14 | 7582.3 | 8.1 | 0.80 | 0.24 |
| 13226.7 | 9.1 | 7558.4 | 5.2 | 0.64 | 0.13 |
| 13261.2 | 12.2 | 7538.7 | 6.9 | 0.77 | 0.20 |
| 13297.8 | 4.2 | 7518.0 | 2.4 | 0.42 | 0.04 |
| 13326.8 | 15.3 | 7501.6 | 8.6 | 1.00 | 0.33 |
| 13382.8 | 11.4 | 7470.2 | 6.4 | 0.62 | 0.15 |
| 13559.6 | 12.1 | 7372.8 | 6.6 | 0.84 | 0.22 |

Table 5.9: Wavenumbers and air wavelength of the band maxima and their corresponding FWHM obtained from Gaussian fit of the photofragmentation spectrum of $C_{70}^+$–He. Uncertainties for the frequencies are $\pm 1\,\mathrm{cm}^{-1}$. The widths have been corrected for power broadening and have uncertainties of 30 %. The oscillator strength $f_\nu$ is given for each band maxima based on their individual absorption cross-sections and FWHMs.

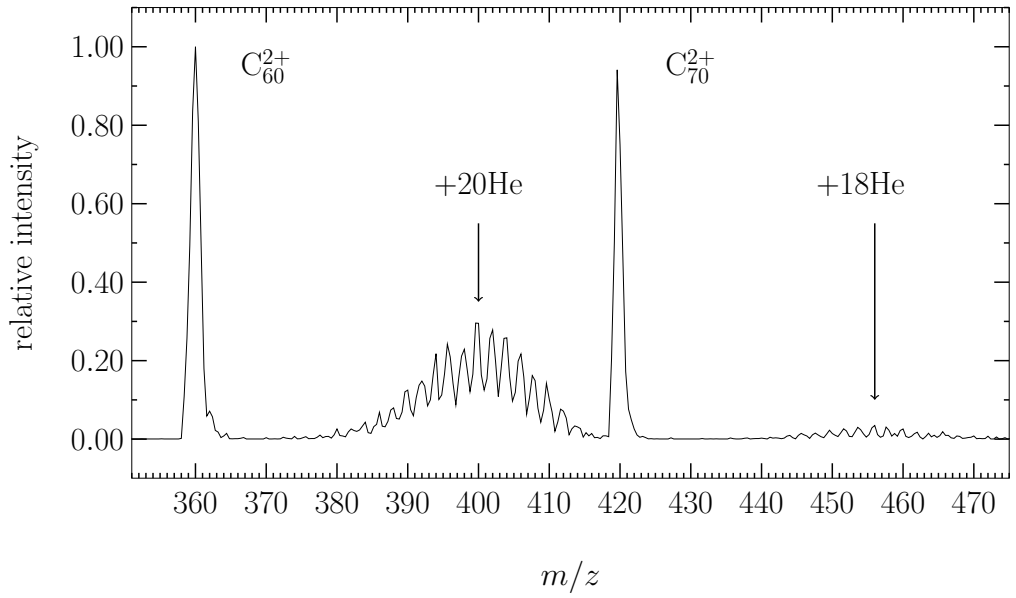


Figure 5.15: Mass spectrum of $C_{60}$ and $C_{70}$ dications with helium attached. The complexes have been formed in a linear quadrupole trap held at $T_{\mathrm{nom}} = 4.5\,\mathrm{K}$ using a helium number density of $1 \times 10^{15}\,\mathrm{cm}^{-3}$.

## 5.3 $C_{60}^{2+}$–He and $C_{70}^{2+}$–He

By increasing the electron impact potential at the source, doubly charged species of $C_{60}$ and $C_{70}$ can be detected in the mass spectrum shown in Figure 5.15. The second ionization potentials are low with $\sim 11.5\,\mathrm{eV}$ and can be easily exceeded with electron bombardment [34]. Attachment of helium is easier due to the additional charge and almost a closed solvation shell around $C_{60}^{2+}$ and $C_{70}^{2+}$ could be formed. For spectroscopic purposes the conditions have been optimized for single helium attachment by increasing the trap temperature.

From matrix results it is expected that $C_{60}^{2+}$–He does not reveal any absorption bands in the NIR and could be confirmed from survey scans using the OPO between the NIR to the UV [35]. This is in agreement with the singlet ground state for which electronic transitions occur typically in the UV region. Fragmentation of the complexes was achieved between 230 and 400 nm; however, no distinct absorption bands were observed.

An absorption band in the 700 nm region has been recently assigned from measurements in neon matrices to $C_{70}^{2+}$ [36]. The transition at $14\,196\,\mathrm{cm}^{-1}$ was attributed to $C_{70}^{+}$ in an earlier study [31]. In the gas-phase this feature was recorded

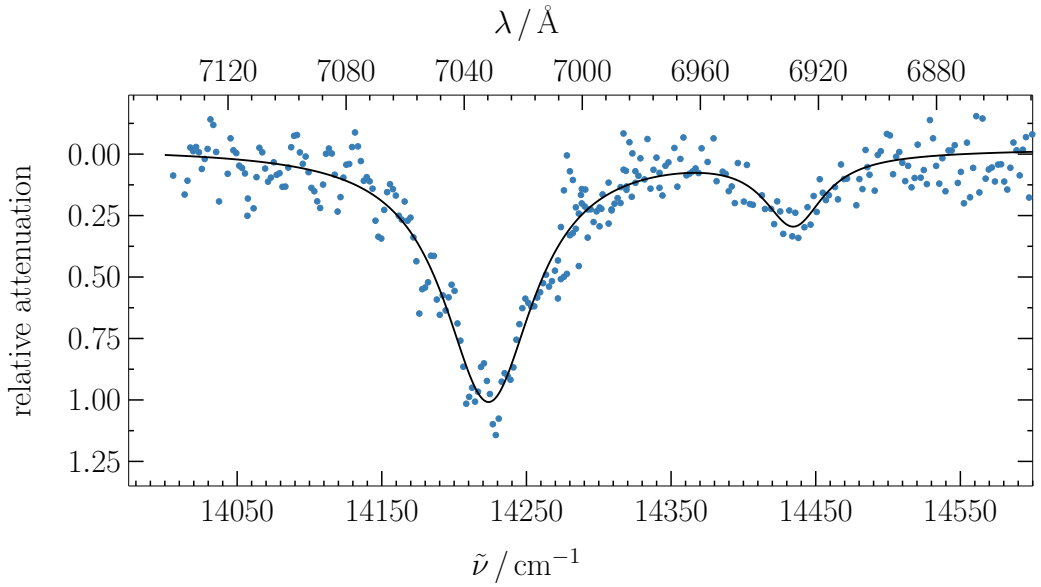


Figure 5.16: Photofragmentation spectrum of $C_{70}^{2+}$–He in the region between 14000-14500 $cm^{-1}$. The normalized experimental data (•) have been fit with Lorentzian functions (–).

with a pulsed-dye laser between 14 000 and 14 650 $cm^{-1}$ at $E_p = 150\,\mu J$. A transition has been observed at $(14\,223 \pm 1)\,cm^{-1}$ followed by a weaker band maximum at $(14\,432 \pm 4)\,cm^{-1}$. Both bands have rather large FWHMs of $(65 \pm 10)$ and $(50 \pm 10)\,cm^{-1}$, respectively. The correlation coefficients for Lorentzian and Gaussian functions are almost equal. For a natural broadening the lifetime is calculated to be $(80 \pm 12)$ fs. An absorption cross-section for the origin band has been estimated as a lower limit to $(8 \pm 5) \times 10^{-16}\,cm^2$, and thus an oscillator strength of $f_{osc} = 0.06$.

The determined value for the absorption cross-section of the origin band is comparable to $C_{60}^{+}$. The dication could be created in interstellar clouds by far-UV photons, although fast internal energy conversion would lead to a small cross-section for photoionization [22]. Therefore, only a small abundance of $C_{70}^{2+}$and possibly $C_{60}^{2+}$in the ISM are expected, even in regions with strong UV flux. Reported DIBs in the range do not match the characteristics of the two observed absorption bands of $C_{70}^{2+}$. In the spectrum of HD 204827 a weak absorption is listed as DIB 345 at $\lambda_c = 7030.29$ Å and has a FWHM of 0.64 Å [37]. An absorption feature assigned as DIB 323 is present in the spectrum of HD 183143 at $\lambda_c = 7030.31$Å but the width of $\Delta\lambda = 0.9$ Å is also much narrower than the ones extracted from the laboratory gas-phase spectrum [33, 38]. Assuming a column density $N(C_{70}^{2+}) = 1 \times 10^{12}\,cm^{-2}$

(equation 5.5), an EW of $W_{7029} = 30\,\text{mÅ}$ can be expected. However, it has been emphasized that the identification of broad DIBs is difficult considering the shallow depth of $\sim 0.1\%$ in the astronomical spectrum at the given column density together with the necessary continuum level subtraction [37, 39, 40].

## 5.4 $C_{84}^+$–He

In 2011 the large fullerene $C_{84}^+$ has been proposed as a possible carrier of a DIB [41]. The assumption was made based on a single absorption band observed at $\lambda = 718,2\,\text{nm}$ with a FWHM of $\Delta\lambda = 3\,\text{nm}$ in a 5 K neon matrix experiment. It was concluded that the two DIBs at $\lambda = 7154\,\text{Å}$ and $\lambda = 7136\,\text{Å}$ (HD 183143) can be reasonable candidates. Furthermore, a transition of $C_{84}^+$ in oleum has been identified at $\lambda = 810\,\text{nm}$ [42].

Gas-phase experiments in the vicinity of these transitions could not confirm the reported absorption band. No fine structure could be resolved between 440 nm and 780 nm using pulse energies of $E_\text{p} \leq 1\,\text{mJ}$, although fragmentation was observed as shown in Figure 5.17. An absorption pattern was also noticed in the UV region between 230 nm and 440 nm, but distinct bands could not be observed.

Unlike $C_{60}$ and $C_{70}$, $C_{84}$ has 24 isomers from which $D_2$ and $D_{2d}$ symmetries are the most energetically favorable [43, 44]. High temperatures in the source ($\sim 550\,°\text{C}$) may initially obtain a larger distribution of isomers, but it can be expected that cooling inside the trap reduces the amount of probed $C_{84}$ isomers.

It is also possible that macroscopic properties obeyed by larger fullerenes have to be considered. Compared to $C_{60}^+$, $C_{84}^+$ has an increased number of valence electrons and exhibits a decreased molecular symmetry. Thus, a high number of energy levels forming band like structures could result in extremely broad absorption bands, in addition to possibly short lifetimes (fs) of the excited electronic states.

## 5.5 Conclusion

Several fullerene-helium complexes have been investigated and discussed by their photofragmentation spectrum with the objective to compare them to astronomical observations. The spectra of $C_{60}^+$–He, $C_{70}^+$–He, and $C_{70}^{2+}$–He revealed several absorption bands in the VIS/NIR. Uncertainties due to induced shifts in the spectrum

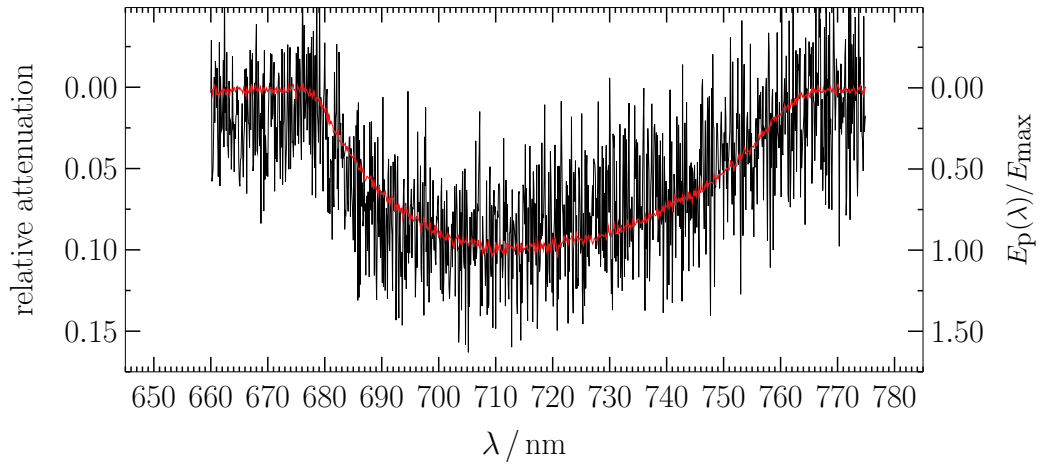


Figure 5.17: Photofragmentation spectrum of $C_{84}^+$–He (–) in the range 670-770 nm at $E_p(\lambda = 720\,\text{nm}) = 1\,\text{mJ}$. The trace (–) on top of experimental data is the power curve of the dye laser.

caused by the helium have been minimized and thus, five absorption bands of $C_{60}^+$ could be assigned to known DIBs. Within the possibilities of the laboratory and astronomical methods all criteria were fulfilled and led to the first identification of a DIB carrier.

The weak estimated oscillator strengths for $C_{70}^+$ and a low expected abundance of $C_{70}^{2+}$ require higher sensitivity of astronomical devices for possible identification in the ISM. In case of $C_{60}^{2+}$–He and $C_{84}^+$–He a loss in complexes due to laser irradiation was noticed, but no distinct absorption bands have been obtained. On the other hand, it is questionable if fullerenes larger than $C_{70}$ should be considered as carriers of DIBs. Their lower symmetry reduces the degeneracies leading to broad absorption bands or congested spectra. Some of them were recently studied in the infrared and there have been no reports of any assignments in $C_{60}$ rich interstellar environments [45].

All fullerenes that were probed in the UV show significant absorptions, but no distinct pattern. Studies of several fullerenes in oleum revealed two peaks in this region with comparable central wavelengths [42]. Also the neon-matrix spectrum of $C_{60}^+$ exhibits a clear pattern with two absorption features between 250 and 350 nm which are supported by TDDFT calculations [35]. This question should be addressed again in future experiments as the UV region is relevant for the so-called UV-bump at 217.5 nm [46].

The absorption cross-section measurements in the 4-pole and 22-pole trap provide also hints for further LIICG experiments. The efficiency should be much higher in a 4-pole trap as apparently only a small fraction of the ions in the 22-pole were excited.

# Bibliography


[1] M. F. Mesleh, J. M. Hunter, A. A. Shvartsburg, G. C. Schatz, and M. F. Jarrold, "Structural information from ion mobility measurements: Effects of the long-range potential", *Journal of Physical Chemistry*, vol. 100, no. 40, pp. 16 082–16 086, 1996. DOI: 10.1021/jp961623v.

[2] B. Follmeg, P. Rosmus, and H. Werner, "Theoretical investigation of collision induced rotational alignment in $N_2^+$–He", *The Journal of Chemical Physics*, vol. 93, no. 7, pp. 4687–4698, 1990. DOI: 10.1063/1.458658.

[3] J. P. Maier, "Interstellar detection of $C_{60}^+$", *Nature*, vol. 370, pp. 423–424, 1994. DOI: 10.1038/370423b0.

[4] B. H. Foing and P. Ehrenfreund, "Detection of two interstellar absorption bands coincident with spectral features of $C_{60}^+$", *Nature*, vol. 369, pp. 296–298, 1994. DOI: 10.1038/369296a0.

[5] J. Fulara, M. Jakobi, and J. P. Maier, "Electronic and infrared spectra of $C_{60}^+$ and $C_{60}^-$ in neon and argon matrices", *Chemical Physics Letters*, vol. 211, no. 2–3, pp. 227–234, 1993. DOI: 10.1016/0009-2614(93)85190-Y.

[6] R. D. Bendale, J. F. Stanton, and M. C. Zerner, "Investigation of the electronic structure and spectroscopy of Jahn–Teller distorted $C_{60}^+$", *Chemical Physics Letters*, vol. 194, no. 4–6, pp. 467–471, 1992. DOI: 10.1016/0009-2614(92)86084-U.

[7] T. Kato, T. Kodama, T. Shida, T. Nakagawa, Y. Matsui, S. Suzuki, H. Shiromaru, K. Yamauchi, and Y. Achiba, "Electronic absorption spectra of the radical anions and cations of fullerenes: $C_{60}$ and $C_{70}$", *Chemical Physics Letters*, vol. 180, no. 5, pp. 446–450, 1991. DOI: 10.1016/0009-2614(91)85147-O.

[8] S. A. Edwards and S. Leach, "Simulated rotational band contours of $C_{60}$ and their comparison with some of the diffuse interstellar bands", *Astronomy and Astrophysics*, vol. 272, p. 533, 1993.

[9] T. Pino, N. Boudin, and P. Bréchignac, "Electronic absorption spectrum of cold naphthalene cation in the gas phase by photodissociation of its van der Waals complexes", *Journal of Chemical Physics*, vol. 111, no. 16, pp. 7337–7347, 1999. DOI: 10.1063/1.480105.

[10] P. Scheier, M. Kuhn, M. Renzler, J. Postler, S. Spieler, M. Simpson, R. Wester, A. Lindinger, J. Cami, A. Tielens, and H. Linnartz, "Solvation of $C_{60}^+$ with He", in, M. Legrand, Ed., ser. Book of Abstracts: Symposium on Size Selected Clusters. 2016, p. 35.

[11] S. Newbury and S. Cohen. (2012). Evaluation of earth's helium supply, [Online]. Available: w3.pppl.gov/ppst/docs/newbury12.pdf (visited on 08/15/2016).

[12] P. Jenniskens, G. Mulas, I. Porceddu, and P. Benvenuti, "Diffuse interstellar bands near 9600Å: Not due to $C_{60}^+$ yet", *Astronomy and Astrophysics*, vol. 327, pp. 337–341, 1997.

[13] G. A. H. Walker, D. A. Bohlender, J. P. Maier, and E. K. Campbell, "Identification of more interstellar $C_{60}^+$ bands", *The Astrophysical Journal Letters*, vol. 812, no. 1, p. L8, 2015. DOI: 10.1088/2041-8205/812/1/L8.

[14] E. K. Campbell, M. Holz, J. P. Maier, D. Gerlich, G. A. H. Walker, and D. Bohlender, "Gas phase absorption spectroscopy of $C_{60}^+$ and $C_{70}^+$ in a cryogenic ion trap: Comparison with astronomical measurements", *The Astrophysical Journal*, vol. 822, no. 1, p. 17, 2016. DOI: 10.3847/0004-637X/822/1/17.

[15] B. H. Foing and P. Ehrenfreund, "New evidences for interstellar $C_{60}^+$", *Astronomy and Astrophysics*, vol. 317, pp. L59–L62, 1997.

[16] T. P. Snow and B. J. McCall, "Diffuse atomic and molecular clouds", *Annual Review of Astronomy and Astrophysics*, vol. 44, pp. 367–414, 2006. DOI: 10.1146/annurev.astro.43.072103.150624.

[17] W. D. Vacca, M. C. Cushing, and J. T. Rayner, "A method of correcting near-infrared spectra for telluric absorption", *The Publications of the Astronomical Society of the Pacific*, vol. 115, no. 805, pp. 389–409, 2003. DOI: 10.1086/346193.

[18] G. H. Herbig, "The search for interstellar $C_{60}$", *The Astrophysical Journal*, vol. 542, pp. 334–343, 2000. DOI: 10.1086/309523.

[19] G. H. Herbig, "The interstellar line spectrum of Zeta Ophiuchi", *Zeitschrift für Astrophysik*, vol. 68, pp. 243–277, 1968.

[20] B. J. McCall, K. H. Hinkle, T. R. Geballe, G. H. Moriarty-Schieven, N. J. E. II, K. Kawaguchi, S. Takano, V. V. Smith, and T. Oka, "Observations of $H_3^+$ in the diffuse interstellar medium", *The Astrophysical Journal*, vol. 567, no. 1, pp. 391–406, 2002. DOI: 10.1086/338380.

[21] J. Cami, "Can fullerene analogues be the carriers of the diffuse interstellar bands?", in *Symposium S297 (The Diffuse Interstellar Bands)*, *Proceedings IAU Symposium*, Z. Knezević and A. Lemaitre, Eds., vol. 9, 2013, pp. 1–5. DOI: 10.1017/S1743921313016141.

[22] A. Omont, "Interstellar fullerene compounds and diffuse interstellar bands", *Astronomy and Astrophysics*, vol. 590, no. A52, pp. 1–27, 2016. DOI: 10.1051/0004-6361/201527685.

[23] A. Kaiser, C. Leidlmair, P. Bartl, S. Zöttl, S. Denifl, A. Mauracher, M. Probst, P. Scheier, and O. Echt, "Adsorption of hydrogen on neutral and charged fullerene: Experiment and theory", *The Journal of Chemical Physics*, vol. 138, no. 074311, pp. 1–14, 2013. DOI: 10.1063/1.4790403.

[24] S. D. Friedman, D. G. York, B. J. McCall, J. Dahlstrom, P. Sonnentrucker, D. E. Welty, M. M. Drosback, L. M. Hobbs, B. L. Rachford, and T. P. Snow, "Studies of diffuse interstellar bands V. Pairwise correlations of eight strong DIBs and neutral hydrogen, molecular hydrogen, and color excess", *The Astrophysical Journal*, vol. 727, no. 1, pp. 1–13, 2011. DOI: 10.1088/0004-637X/727/1/33.

[25] C. Leidlmair, P. Bartl, H. Schöbel, S.Denifl, M. Probst, P. Scheier, and O. Echt, "On the possible presence of weakly bound fullerene–$H_2$ complexes in the interstellar medium", *The Astrophysical Journal Letters*, vol. 738, no. L4, pp. 1–5, 2011. DOI: 10.1088/2041-8205/738/1/L4.

[26] D. Strelnikov, B. Kern, and M. M. Kappes, "On observing $C_{60}^{+}$ and $C_{60}^{2+}$ in laboratory and space", *Astronomy and Astrophysics*, vol. 584, A55, 2015. DOI: 10.1051/0004-6361/201527234.

[27] V. S. Langford and B. E. Williamson, "Magnetic circular dichroism of $C_{60}^{+}$ and $C_{60}^{-}$ radicals in argon matrixes", *The Journal of Physical Chemistry A*, vol. 103, no. 33, pp. 6533–6539, 1999. DOI: 10.1021/jp991393v.

[28] J. Cami, J. Bernard-Salas, E. Peeters, and S. E. Malek, "Detection of $C_{60}$ and $C_{70}$ in a young planetary nebula", *Science*, vol. 329, no. 5996, pp. 1180–1182, 2010. DOI: 10.1126/science.1192035.

[29] L. Becker, R. J. Poreda, and T. E. Bunch, "Fullerenes: An extraterrestrial carbon carrier phase for noble gases", *Proceedings of the National Academy of Sciences*, vol. 97, no. 7, pp. 2979–2983, 2000. DOI: 10.1073/pnas.97.7.2979.

[30] R. Wörgötter, B. Dünser, P. Scheier, and T. D. Märk, "Appearance and ionization energies of $C_{60-2m}^{z+}$ and $C_{70-2m}^{z+}$ ions (with $z$ and $m$ up to 4) produced by electron impact ionization of C60 and C70, respectively", *The Journal of Chemical Physics*, vol. 101, no. 10, pp. 8674–8679, 1994. DOI: 10.1063/1.468062.

[31] J. Fulara, M. Jakobi, and J. P. Maier, "Electronic spectra of the $C_{70}$ molecule and $C_{70}^{+}$, $C_{70}^{-}$ ions in neon matrices", *Chemical Physics Letters*, vol. 206, no. 1–4, pp. 203–209, 1993. DOI: 10.1016/0009-2614(93)85542-V.

[32] G. A. Galazutdinov, F. A. Musaev, J. Krełowski, and G. A. H. Walker, "Narrow diffuse interstellar bands: A survey with precise wavelengths", *Publications of the Astronomical Society of the Pacific*, vol. 112, no. 771, 2000. DOI: 10.1086/316570.

[33] P. Jenniskens and F. Désert, "A survey of diffuse interstellar bands (3800-8680 Å)*", *Astronomy and Astrophysics Supplement Series*, vol. 106, pp. 39–78, 1994.

[34] H. Steger, . de Vries, B. Kamke, and W. Kamke, "Direct double ionization of $C_{60}$ and $C_{70}$ fullerenes using synchrotron radiation", *Chemical Physics Letters*, vol. 194, no. 4–6, pp. 452–456, 1992. DOI: 10.1016/0009-2614(92)86081-R.

[35] B. Kern, D. Strelnikov, P. Weis, A. Böttcher, and M. M. Kappes, "IR, NIR, and UV absorption spectroscopy of $C_{60}^{2+}$ and $C_{60}^{3+}$ in neon matrixes", *The Journal of Physical Chemistry Letters*, vol. 5, no. 3, pp. 457–460, 2014. DOI: 10.1021/jz402630z.

[36] B. Kern, A. Böttcher, and D. Strelnikov, "IR and UV-NIR absorption spectroscopy of matrix-isolated $C_{70}^{+}$ and $C_{70}^{-}$", *The Journal of Physical Chemistry A*, vol. 120, no. 29, pp. 5868–5873, 2016. DOI: 10.1021/acs.jpca.6b06212.

[37] L. M. Hobbs, D. G. York, T. P. Snow, T. Oka, J. A. Thorburn, M. Bishof, S. D. Friedman, B. J. McCall, B. Rachford, P. Sonnentrucker, and D. E. Welty, "A catalog of diffuse interstellar bands in the spectrum of HD 204827", *The Astrophysical Journal*, vol. 680, no. 2, pp. 1256–1270, 2008. DOI: 10.1086/587930.

[38] L. M. Hobbs, D. G. York, J. A. Thorburn, T. P. Snow, M. Bishof, S. D. Friedman, B. J. McCall, T. Oka, and B. Rachford, "Studies of the diffuse interstellar bands. III. HD 183143", *The Astrophysical Journal*, vol. 705, no. 1, pp. 32–45, 2009. DOI: 10.1088/0004-637X/705/1/32.

[39] J. Sollerman, N. Cox, S. Mattila, P. Ehrenfreund, L. Kaper, B. Leibundgut, and P. Lundqvist, "Diffuse interstellar bands in NGC 1448", *Astronomy and Astrophysics*, vol. 429, pp. 559–567, 2005. DOI: 10.1051/0004-6361:20041465.

[40] P. Ehrenfreund, J. Cami, E. Dartois, and B. Foing, "Diffuse interstellar bands towards BD+63° 1964⋆", *Astronomy and Astrophysics*, vol. 317, pp. L28–L31, 1997.

[41] T. M. Halasinski, R. Ruiterkamp, F. Salama, B. H. Foing, and P. Ehrenfreund, "$C_{84}$: A prototype of larger fullerenes. laboratory spectroscopy and astronomical relevance", *Fullerenes, Nanotubes and Carbon Nanostructures*, vol. 19, no. 5, pp. 398–409, 2011. DOI: 10.1080/15363831003721807.

[42] F. Cataldo, S. Iglesias-Groth, and A. Manchado, "On the radical cation spectra of fullerenes and fulleranes. Part 1: $C_{60}$, $C_{70}$, $C_{76}$, $C_{78}$ and $C_{84}$", *Fullerenes, Nanotubes and Carbon Nanostructures*, vol. 20, no. 8, pp. 656–671, 2012. DOI: 10.1080/1536383X.2011.572313.

[43] D. E. Manolopoulos and P. W. Fowler, "Molecular graphs, point groups, and fullerenes", *The Journal of Chemical Physics*, vol. 96, no. 10, pp. 7603–7614, 1992. DOI: 10.1063/1.462413.

[44] X. Wang, C. Z. Wang, B. L. Zhang, and K. M. Ho, "Structural and electronic properties of $C_{84}$: A first-principles study", *Physical Review Letters*, vol. 69, no. 1, pp. 69–73, 1992. DOI: 10.1103/PhysRevLett.69.69.

[45] F. Cataldo, Y. Hafez, and S. Iglesias-Groth, "FT-IR spectra of fullerenes $C_{76}$, $C_{78}$ and $C_{84}$ at temperatures between −180°C and +250°C", *Fullerenes, Nanotubes and Carbon Nanostructures*, vol. 22, 2014. DOI: 10.1080/1536383X.2012.749455.

[46] B. T. Draine, "Interstellar dust grains", *Annual Review of Astronomy and Astrophysics*, vol. 41, pp. 241–289, 2003. DOI: 10.1146/annurev.astro.41.011802.094840.

# 6

*Alles ist in der Natur verbunden: ein Zustand strebt zum andern und bereitet ihn vor.*

■ Johann Gottfried Herder

# Conclusion and Outlook

A combined technique of ion trapping and mass selection enabled the measurement of the electronic spectra of cationic fullerenes at cryogenic temperatures. The recorded spectra allowed the confirmation of $C_{60}^+$ as the carrier of the two DIBs at 9577 Å and 9632 Å, finally after it was proposed more than 20 years ago. In addition, three more of them could be assigned to this molecule leaving almost no doubts. All postulated criteria could be fulfilled and the first five pieces in the puzzle of the diffuse interstellar bands have been put together [1, 2].

A further investigation by applying, e.g., LIICG to fullerenes should be the aim, to elaborate this technique to a standard spectroscopic tool. In that case, laboratory uncertainties could be almost narrowed down to pure statistical errors. But not only the laboratory, also the astronomical sensitivity could be improved. One opportunity may be the James Webb Space Telescope, launch date October 2018. It is optimized for NIR and IR in the range from 0.6 to 2.3 $\mu$m [3]. The telluric correction as they are necessary for ground-based astronomy can than be omitted and may enable lower detection limits. Already in space is the Hubble Space Telescope, which is also equipped with a near infrared camera and multi-object spectrometer, unfortunately this device is currently not operating [4].

The high abundance of $C_{60}^+$ provides a strong stimulus for further optical spectroscopy of fullerene derivatives. Fulleranes, substitution of carbon and embedded atoms or molecules inside the cage as well as endohedral fullerenes lead to enormous amounts of possible carriers [5–7]. The selection of a candidate by pure chemical intuition may not be sufficient and different strategies should be thought of. An interesting approach has been used to find correlations between DIBs with machine learning [8]. Extending this by including experimental and theoretical results of already available data may improve the identification process.

Formation mechanisms of fullerenes have been also extensively discussed. The rich organic inventory of the ISM allows a multitude of chemical processes. A build-up of molecules from small to large has been based on ion-molecule or grain-surface chemistry in hot and dense environments of evolved stars [9, 10]. However, this theory can not explain that $C_{60}$ is formed also in the cold interstellar regions [11]. It has been argued that large PAHs are converted by photochemical evolution into graphene sheets which migrate to fullerenes by spontaneous curling due to carbon loss [12]. This "top-down" route is supported by laboratory experiments creating $C_{60}^+$ and $C_{70}^+$ from photolysis of large PAHs [13]. The detection was based on mass-spectrometry rather than spectroscopy and may still leave some doubts. Therefore, the new developments in spectroscopy of fullerenes could solve this question in future experiments.

# Bibliography


[1] T. P. Snow, "Diffuse interstellar bands: Past and present", in *Symposium S297 (The Diffuse Interstellar Bands)*, Z. Knezević and A. Lemaitre, Eds., vol. 9, 2013, pp. 1–12. DOI: 10.1017/S1743921313015512.

[2] J. P. Maier, "Interstellar detection of $C_{60}^{+}$", *Nature*, vol. 370, pp. 423–424, 1994. DOI: 10.1038/370423b0.

[3] Space Telescope Science Institute. (2013). James Webb Space Telescope: NIRCam Pocket Guide, [Online]. Available: http://www.stsci.edu/jwst/instruments/nircam/docarchive/NIRCam-pocket-guide.pdf (visited on 08/17/2016).

[4] European Space Agency. (2016). Hubble's instruments: NICMOS - near infrared camera and multi-object spectrometer, [Online]. Available: https://www.spacetelescope.org/about/general/instruments/nicmos/.

[5] A. Omont, "Interstellar fullerene compounds and diffuse interstellar bands", *Astronomy and Astrophysics*, vol. 590, no. A52, pp. 1–27, 2016. DOI: 10.1051/0004-6361/201527685.

[6] F. Cataldo, "Fullerane, the hydrogenated $C_{60}$ fullerene: Properties and astrochemical considerations", *Fullerenes, Nanotubes and Carbon Nanostructures*, vol. 11, no. 4, 2003. DOI: 10.1081/FST-120025852.

[7] H. W. Kroto and M. Jura, "Circumstellar and interstellar fullerenes and their analogues", *Astronomy and Astrophysics*, vol. 263, no. 1–2, pp. 275–280, 1992.

[8] D. Barona, D. Poznanski, D. Watson, Y. Yao, N. L. J. Cox, and J. X. Prochaska, "Using machine learning to classify the diffuse interstellar bands", *Monthly Notices of the Royal Astronomical Society*, vol. 451, pp. 332–352, 2015. DOI: 10.1093/mnras/stv977.

[9] A. G. G. Tielens, "The molecular universe", *Reviews of Modern Physics*, vol. 85, no. 3, pp. 1021–1081, 2013. DOI: 10.1103/RevModPhys.85.1021.

[10] S. Irle, G. Zheng, Z. Wang, and K. Morokuma, "The $C_{60}$ formation puzzle "solved": QM/MD simulations reveal the shrinking hot giant road of the dynamic fullerene self-assembly mechanism", *The Journal of Physical Chemistry B*, vol. 110, no. 30, pp. 14 531–14 545, 2006. DOI: 10.1021/jp061173z.

[11] O. Berné and A. G. G. M. Tielens, "Formation of buckminsterfullerene ($C_{60}$) in interstellar space", *Proceedings of the National Academy of Sciences of the United States of America*, vol. 192, no. 2, pp. 401–406, 2011. DOI: 10.1073/pnas.1114207108.

[12] A. Chuvilin, U. Kaiser, E. Bichoutskaia, N. A. Besley, and A. N. Khlobystov, "Direct transformation of graphene to fullerene", *Nature Chemistry*, vol. 2, 2010. DOI: 10.1038/nchem.644.

[13] J. Zhen, P. Castellanos, D. M. Paardekooper, H. Linnartz, and A. G. G. M. Tielens, "Laboratory formation of fullerenes from PAHs: Top-down interstellar chemistry", *The Astrophysical Journal Letters*, vol. 797, no. 2, pp. 1–5, L30 2014. DOI: 10.1088/2041-8205/797/2/L30.

# Appendix

## A Relaxation Kinetics: Microscopic Reversibilty

The angular momentum in terms of an inelastic collision is expressed by

$$\vec{l} = \vec{b} \times \vec{p} = \mu v b, \tag{A.1}$$

with the $\vec{b}$ as the impact parameter and $\mu$ the reduced mass. Quantization of the angular momentum using $\hbar^2(J + 1/2)$ yields a cross-section with transition probability $P^J_{i\to f}(v)$

$$\sigma_{i\to f} = 2\pi \left(\frac{\hbar}{\mu v}\right)^2 \sum_J \left(J + \frac{1}{2}\right) P^J_{i\to f}(v). \tag{A.2}$$

By introducing the wave vector

$$k_i = \sqrt{\frac{2\mu(E - \epsilon_i)}{\hbar^2}}, \tag{A.3}$$

where $E = E_{\text{coll}+\epsilon}$ is the total energy composed of translational and state specific internal energy of the system. Furthermore degeneracy of the initial and final states $(2j_i + 1), (2j_f + 1)$ are added. Now the cross-section has to be summed over the rotational degeneracies of the final and averaged over the rotational degeneracy of the initial state:

$$\sigma_{i\to f} = \frac{\pi}{(2j_i + 1)k_i^2} \sum_J \sum_{m_i, m_f} (2J + 1) P^J_{j_i m_i, j_f m_f}(E), \tag{A.4}$$

where $m_i$ and $m_f$ denote the projection quantum number of the angular momentum. The transition probability is now a matrix depending on a particular value of the angular momentum, and the total energy the independent variable. A property of the matrix $P$ is, that it is symmetric, which means it satisfies:

$$P^J_{j_i m_i, j_f m_f}(E) = P^J_{j_f m_f, i_i m_i}(E) \tag{A.5}$$

This is a consequence of the invariance of the laws of motion under time reversal, called microscopic reversibility [1].

For an ensemble of particles with rate constants $k(v)$ with relative velocities $v$,

the thermal rate constant can be written as an average of these over a Maxwell-Boltzman distribution $f(v)$:

$$k(T) = \int_0^\infty k(v) f(v) dv. \tag{A.6}$$

The rate of collision induced transitions is equal to the cross-section multiplied with the incoming flux. Furthermore, the flux is defined by the relative velocity and the number density. Therefore, one can write for a quantized system:

$$\frac{dn_{i\to f}}{dt} = \rho k_{i\to f}(v) = \rho v \sigma_{i\to f} f(v) \tag{A.7}$$

Substituting the last two equations into each other yields:

$$k_{i\to f}(T) = \sqrt{\frac{8}{\mu\pi k_\mathrm{B} T}} \int_0^\infty \exp\left(E_\mathrm{col}/k_\mathrm{B}T\right) \sigma_{i\to f}(E) E_\mathrm{col} dE_\mathrm{col} \tag{A.8}$$

Next, the integration variable has to be changed to the total energy $E$:

$$k_{i\to f}(T) = \sqrt{\frac{8}{\mu\pi k_\mathrm{B} T}} \int_{\epsilon_i}^\infty \exp\left((E-\epsilon_i)/k_\mathrm{B}T\right) \sigma_{i\to f}(E)(E-\epsilon_i) dE \tag{A.9}$$

The rate coefficient for the reversed process is obtained by swapping the indices $i$ and $f$. Furthermore using eq.$(A.5)$ together with eq.$(A.4)$ yields:

$$\begin{aligned} k_{f\to i}(T) = &\sqrt{\frac{8}{\mu\pi k_\mathrm{B} T}} \frac{(2j_i+1)}{(2j_f+1)} \exp\left(\epsilon_f/k_\mathrm{B}T\right) \\ &\cdot \int_0^\infty \exp\left(-\epsilon_i/k_\mathrm{B}T\right) \sigma_{i\to f}(E)(E-\epsilon_i) dE \end{aligned} \tag{A.10}$$

Comparing the results for $k_{i\to f}(T)$ and $k_{f\to i}(T)$, one can find what is called the detailed balance relation:

$$\frac{k_{f\to i}(T)}{k_{i\to f}(T)} = \frac{(2j_i+1)}{(2j_f+1)} \exp\left((\epsilon_f - \epsilon_i)/k_\mathrm{B}T\right) \tag{A.11}$$

With this equation the reversed rate constants can be calculated. For further reading see e.g. Ref. [2].

# B Table Parameters of 9577/9632 DIBs

| DIB 9577 | | DIB 9632 | | | | | |
|---|---|---|---|---|---|---|---|
| $\lambda_c$ / Å | FWHM / Å | $\lambda_c$ / Å | FWHM / Å | $\frac{W_{9632}}{W_{9577}}$ | $\frac{EW^a_{9632}}{EW_{9577}}$ | Object | Ref. |
| $9577.4 \pm 0.2$ | $3.0 \pm 0.2$ | $9632.6 \pm 0.2$ | $3.0 \pm 0.2$ | 0.98 | - | HD43384 | [3] |
| $9577.4 \pm 0.2$ | $3.0 \pm 0.2$ | $9632.6 \pm 0.2$ | $3.0 \pm 0.2$ | 0.92 | - | HD63804 | [3] |
| $9577.4 \pm 0.2$ | $3.0 \pm 0.2$ | $9632.6 \pm 0.2$ | $3.0 \pm 0.2$ | 0.85 | - | HD80077 | [3] |
| 9577.0 | $2.85 \pm 0.20$ | 9632.0 | $2.9 \pm 0.2$ | 1.17 | - | HD183143 | [4] |
| 9577.0 | $4.0 \pm 0.3$ | 9632.0 | $4.0 \pm 0.3$ | 1.09 | - | HD37022 | [4] |
| 9577.0 | $2.9 \pm 0.4$ | 9632.0 | $2.9 \pm 0.4$ | 0.86 | - | HD80077 | [4] |
| $9577.1 \pm 0.2$ | $3.90 \pm 0.12$ | 9632.0 0.2 | $2.70 \pm 0.05$ | - | 1.08 | HD161061 | [5] |
| $9577.1 \pm 0.2$ | - | 9632.0 0.2 | - | - | 1.33 | HD147889 | [5] |
| $9577.1 \pm 0.2$ | $3.30 \pm 0.07$ | 9632.0 0.2 | $2.50 \pm 0.03$ | - | 1.01 | HD183143 | [5] |
| $9577.1 \pm 0.2$ | $4.80 \pm 0.07$ | 9632.0 0.2 | $3.60 \pm 0.06$ | - | 0.95 | 4U1907 | [5] |
| 9577.0 | 4.4 | 9633.2 | 4.2 | - | 0.92 | HD37022 | [6] |
| 9577.2 | 5.4 | 9633.0 | 4.5 | - | 0.75 | HD37041 | [6] |
| 9577.0 | $2.3 \pm 0.3$ | 9632.0 | $2.0 \pm 0.3$ | 1.23 | - | PPN | [7] |
| - | - | - | - | 1.13 | - | CygOB2/8A | [8] |
| 9577.2 | - | 9632.3 | - | 0.68 | 0.86 | HD167971 | [9] |
| 9576.5 | - | 9632.1 | - | 0.77 | 0.91 | HD168607 | [9] |
| 9576.7 | - | 9632.3 | - | 0.88 | 1.63 | HD186745 | [9] |
| 9577.3 | - | 9632.6 | - | 0.68 | 0.84 | HD183143 | [9] |
| 9577.0 | - | 9632.3 | - | 0.75 | 1.08 | HD190603 | [9] |
| 9576.7 | - | 9631.6 | - | 0.77 | 1.01 | HD194279 | [9] |
| 9577.0 | - | 9631.8 | - | 0.62 | 0.74 | HD195592 | [9] |
| 9576.1 | - | 9631.3 | | 0.63 | 0.82 | HD224055 | [9] |
| 9576.9 | - | 9631.9 | - | 0.68 | 0.79 | BD+404220 | [9] |
| 9577.4 | 3.3 | - | - | - | - | HD183143 | [10] |
| 9577.2 | 3.5 | - | - | - | - | HD169454 | [10] |
| - | - | - | - | 1.00 | 1.32 | HD193237 | [9] |
| - | - | - | - | 0.57 | 0.88 | HD190603 | [9] |
| - | - | - | - | 1.10 | 1.50 | HD198478 | [9] |
| - | - | - | - | 0.98 | 1.17 | HD183143 | [9] |
| - | - | - | - | 0.59 | 1.22 | HD206165 | [9] |
| - | - | - | - | 0.73 | 1.06 | HD169454 | [9] |
| - | - | - | - | 0.50 | 0.86 | HD80077 | [9] |
| - | - | - | - | 0.70 | 1.10 | HD37022 | [9] |
| 9577.0 | 3.5 | 9632.2 | 3.2 | 0.83 | 1.04 | mean | |
| 0.3 | 0.9 | 0.4 | 0.7 | 0.21 | 0.24 | s.d. | |

Table B.1: Reported characteristics for 9577/9632 DIBs toward different lines-of-sight. [a]Equivalent widths are uncorrected for MgII contamination in the spectrum.

# Bibliography


[1] I. W. M. Smith, *Gas kinetics and energy transfer*, P. G. Ashmore and R. J. Donovan, Eds., ser. Specialist Periodical Reports. The Chemical Society, 1977, vol. 2. DOI: 10.1039/9781847556103-00001.

[2] J. C. Polanyi and J. L. Schreiber, *The dynamics of bimolecular reactions*, H. Eyring, D. Henderson, and W. Jost, Eds., ser. Physical Chemistry: An Advanced Treatise. Academic Press, INC., 1974, vol. VIA Kinetics of Gas Reaction.

[3] P. Jenniskens, G. Mulas, I. Porceddu, and P. Benvenuti, "Diffuse interstellar bands near 9600Å: Not due to $C_{60}^+$ yet", *Astronomy and Astrophysics*, vol. 327, pp. 337–341, 1997.

[4] B. H. Foing and P. Ehrenfreund, "New evidences for interstellar $C_{60}^+$", *Astronomy and Astrophysics*, vol. 317, pp. L59–L62, 1997.

[5] N. L. J. Cox, J. Cami, L. Kaper, P. Ehrenfreund, B. H. Foing, B. B. Ochsendorf, S. H. M. van Hooff, and F. Salama, "VLT/X-Shooter survey of near-infrared diffuse interstellar bands", *Astronomy and Astrophysics*, vol. 569, no. A117, pp. 1–13, 2014. DOI: 10.1051/0004-6361/201323061.

[6] T. Misawa, P. Gandhi, A. Hida, T. Tamagawa, and T. Yamaguchi, "Identification of new near-infrared diffuse interstellar bands in the Orion nebula", *The Astrophysical Journal*, vol. 700, no. 2, p. 1988, 2009. DOI: 10.1088/0004-637X/700/2/1988.

[7] S. I. Groth and M. Esposito, "A search for near infrared bands of the fullerene cation $C_{60}^+$ in the protoplanetary nebula IRAS 01005+7910", *The Astrophysical Journal Letters*, vol. 776, no. 1, pp. 1–4, 2013. DOI: 10.1088/2041-8205/776/1/L2.

[8] G. H. Herbig, "The search for interstellar $C_{60}$", *The Astrophysical Journal*, vol. 542, pp. 334–343, 2000. DOI: 10.1086/309523.

[9] G. A. Galazutdinov, J. Krełowski, F. A. Musaev, P. Ehrenfreund, and B. H. Foing, "On the identification of the $C_{60}^+$ interstellar features", *Monthly Notices of the Royal Astronomical Society*, vol. 317, no. 4, pp. 750–758, 2000. DOI: 10.1046/j.1365-8711.2000.03566.x.

[10] G. A. H. Walker, D. A. Bohlender, J. P. Maier, and E. K. Campbell, "Identification of more interstellar $C_{60}^+$ bands", *The Astrophysical Journal Letters*, vol. 812, no. 1, p. L8, 2015. DOI: 10.1088/2041-8205/812/1/L8.